THESIS

DETECTION AND TRANSIT TIME MEASUREMENTS OF INDIVIDUAL SODIUM ATOMS DIFFUSING IN A HELIUM FLOW BY THE LASER RESONANCE FLUORESCENCE CORRELATION TECHNIQUE

Submitted by

Ci-Ling Pan

Physics

In partial fulfillment of the requirements

for the Degree of Doctor of Philosophy

Colorado State University

Fort Collins, Colorado

Fall, 1979

COLORADO STATE UNIVERSITY

Fall, 1979

WE HEREBY RECOMMEND THAT THE THESIS PREPARED UNDER OUR SUPERVISION ENTITLED DETECTION AND TRANSIT TIME MEASUREMENTS OF INDIVIDUAL SODIUM ATOMS DIFFUSING IN A HELIUM FLOW BY THE LASER RESONANCE FLUORESCENCE CORRELATION TECHNIQUE BE ACCEPTED AS FULFILLING IN PART REQUIREMENTS FOR THE DEGREE OF DOCTOR OF PHILOSOPHY.

Committee on Graduate Work

William M. Fairbank Jr.

E. Everett Bergmann

Lawrence N. Hadley

David A. Krueger

Gi-an-yuu Yee

Adviser

ABSTRACT OF THESIS

DETECTION AND TRANSIT TIME MEASUREMENTS OF INDIVIDUAL SODIUM ATOMS DIFFUSING IN A HELIUM FLOW BY THE LASER RESONANCE FLUORESCENCE CORRELATION TECHNIQUE

This thesis describes the laser resonance fluorescence correlation technique for single-atom velocity measurement. Using this technique, we have detected individual sodium atoms diffusing through a laser beam in a slow helium flow. From the width of the fluorescence bursts detected, the transit time for the diffusing atom is determined. This is the first measurement of the motion of a single atom in a buffer gas. A probability analysis was developed which allowed us to estimate the average burst size of emitted fluorescence photons by an atom traversing the laser beam. All these results were in general agreement with the theoretical predictions. With improvements, we will be able to measure the velocity of a single-atom either in a flow or in a vacuum.

By averaging over many sodium atoms, the diffusion coefficients of sodium atoms in helium and argon buffer gases were investigated using this technique. The measured diffusion coefficients were found to be in reasonable agreement with theoretical predictions and previous experimental results. To our knowledge, this is the

first application of resonance fluorescence correlation technique to the measurement of diffusion coefficient of fast moving atoms in gases.

Ci-Ling Pan
Physics Department
Colorado State University
Fort Collins, Colorado 80523
Fall, 1979

ACKNOWLEDGMENTS

I am indebted to Dr. C. Y. She, my advisor, for his guidance, encouragement and support throughout my graduate education. I would like to thank my committee members for their help and interests in my work. In particular, I would like to thank Dr. W. M. Fairbank, Jr. for many helpful discussions and suggestions during the course of this research and for his critical reading and comments on the manuscripts of this thesis. I wish to express my appreciation for the help and contributions of Mr. John Prodan who worked closely with me since the summer of 1978. I have also had many helpful discussions with Mr. Al Tveton. I would like to thank Mr. Jim Buckley for helping me build the apparatus used in this experiment. The loving patience and encouragement of my wife, Ru-Pin, kept me going throughout this research. As a physicist, she has also provided insights in many of our discussions concerning my experiment. Our son, Yu-Chin, has also been an inspiration to me. I am grateful to my parents, Mr. and Mrs. An-Sheng Pan, whose enthusiasm and support made my graduate study abroad possible in the first place.

TABLE OF CONTENTS

Chapter		Page
I.	INTRODUCTION	1
II.	THEORY	6
	2.1 Resonance Fluorescence of Sodium Atoms in a Helium Flow	6
	2.2 Single-Atom Burst Correlation Technique	17
	2.3 Ensemble-Averaged Correlation Function	32
III.	EXPERIMENTAL METHODS	38
	3.1 General Description	38
	3.2 Flow Cell Design	40
	3.3 The Total Detection Efficiency	45
	3.4 The Iodine Vapor Cell as an Optical Filter	57
	3.5 Signal Processing	63
	3.6 Experimental Procedures	67
IV.	SINGLE-ATOM DETECTION AND TRANSIT-TIME MEASUREMENTS: PROGRESS TO DATE	74
	4.1 Estimate of Flow Velocity	76
	4.2 Single-Atom Burst Correlation Functions	80
	4.3 Probability Analysis	94
V.	DIFFUSION COEFFICIENTS MEASUREMENTS	105
	5.1 Theoretical Predictions	106
	5.2 Experimental Results	115
VI.	CONCLUSIONS AND SUGGESTIONS FOR FUTURE WORK	134
REFERENCES		139

LIST OF FIGURES

Figure		Page
I-1	Different schemes for detecting a single atom with lasers. It may be detected by observing the emitted fluorescence photons as in (a) and (b), or by photoionization or field ionization as in (c) and (d)	2
II-1	The function $f(x) = \sqrt{x} \int_{-\infty}^{\infty} \frac{du}{e^{u^2} + x}$ vs x, $0.01 \leq x \leq 1,000$	10
II-2	The function $f_2(b/w) = F_b/F$ vs b/w, $0 \leq b/w \leq 2$	12
II-3	F_b/F as a function of the percentage of emitted fluorescence photons with bursts larger than or equal to F_b	13
II-4	Pressure-broadened sodium D_2 line at 200 Torr of helium	16
II-5(a)	A typical single-beam correlation function due to a dust particle. The beam width is w = 144 μm. Flow velocity determined from $1/e^2$ point of the correlation function is 12 cm/sec	25
(b)	A correlation function obtained with two laser beams due to a dust particle. The two beams of radii w = 125 μm are separated by 500 μm. The velocity as determined from the separation of the two humps and the $1/e^2$ points of each hump are 18 cm/sec and 12 cm/sec, respectively	25

LIST OF FIGURES (CONTINUED)

Figure		Page
II-6(a)	The detected pulse train C ($q\Delta T$) showing a burst of 31 counts above clipping level k = 1 with initial and final samples q_i and q_f	27
(b)	The single-clipped correlation function R_k ($m\Delta T$) obtained with the pulse train C_k ($q\Delta T$). The average background level is indicated by the line marked BKG	27
III-1	A block diagram of the experimental apparatus	39
III-2	Layout of the flow cell with glass central sections no. 1 and no. 2	42
III-3	Set up for measurement of the transmission of the lens system. F's indicate focuses of the two lenses	46
III-4	Count rate detected is plotted as a function of high voltages applied to the photocathode of our RCA 31034A photomultiplier	50
III-5	Differential pulse height spectrum of our RCA 31034A photomultiplier taken at 1500 V	51
III-6	Differential pulse height spectrum of our RCA 31034A photomultiplier taken at 1800 V	52
III-7	The detector aperture function f_1 (z/L_p) as a function of the distance of the pin-hole from the center of the observation region, z	55
III-8	The iodine absorption line in the vicinity of sodium D_2 line	58

LIST OF FIGURES (CONTINUED)

Figure		Page
III-9	The attenuation factor for stray light, for stray plus Rayleigh scattering due to 200 Torr of helium buffer gas, and for sodium resonance fluorescence by our iodine filter are plotted as a function of $p/T^{3/2}$	62
III-10	The operation of the Malvern single-clipped digital correlator, illustrating the manner in which a two-humped correlation function is obtained for a two beam time-of-flight velocity measurement	65
IV-1	τ_D at 200 Torr of helium and 40°C, and τ_f for flow velocities v = 100 cm/sec, 500 cm/sec and 1000 cm/sec as a function of beam radius w	75
IV-2	Single-particle correlation functions obtained with one laser beam of radius w = 144 μm for (a) Δp = 1 Torr, (b) Δp = 4 Torr, and (c) Δp = 8 Torr, respectively	79
IV-3	Three consecutive single-particle correlation functions obtained with two laser beams of radii w = 210 μm and w = 165 μm and separated by 670 μm, Δp = 20 Torr	81
IV-4(a)	Single-atom correlation function obtained with two 75 μm radii laser beams separated by 500 μm, with 2 mw per beam	84
(b)	Correlation function due to noise counts obtained when no sodium atom was present	84
IV-5	Single-atom correlation functions obtained with (a) one laser beam of radius w = 350 μm and (b) two laser beams of radii w = 625 μm and separated by 725 μm. The iodine filter was used in these experiments	86

LIST OF FIGURES (CONTINUED)

Figure		Page
IV-6	Two multi-humped correlation functions obtained at higher sodium level with (a) one laser beam of radius w = 350 μm and (b) two laser beams of radii w = 625 μm and separation ℓ = 725 μm. The iodine filter was used in these experiments	89
IV-7	Two single-atom correlation functions obtained with two laser beams with w = 65 μm and separation ℓ = 875 μm	92
IV-8	The function $f_3(p', x) = \int_{-\infty}^{p'} \frac{du}{e^{u^2}+x} \Big/ \int_{-\infty}^{\infty} \frac{du}{e^{u^2}+x}$ versus p', where $p' = \frac{\sqrt{2}\,vt}{w}$ and x = 1.91	100
IV-9	Probability distribution of detected counts both on and off-resonance. A single laser beam of radius w = 65 μm at laser power p = 1.4 mw was used. The sample time is ΔT = 250 μs	102
IV-10	The probability distribution of detected counts on resonance as shown in Fig. IV-8 is now shown with the theoretically predicted distribution with $\epsilon\eta F$ = 15 counts	104
V-1	Reduced collision integral for diffusion Ω_D^* as a function of reduced temperature $T^* = kT/\epsilon_{12}$	114
V-2	Typical time-averaged correlation function for diffusing sodium atoms in 200 Torr of helium with Δp = 1 Torr. The radii of the laser beams used were w_x = 109 μm and w_y = 91 μm	116

LIST OF FIGURES (CONTINUED)

Figure		Page
V-3	The diffusion time $\tau_{Dx} = w_x^2/4D$, $w_x = 109$ μm versus the pressure of helium buffer gas	118
V-4	The data shown in Fig. V-3 have now been normalized using the $T^{3/2}$ dependence to 273 K and plotted as a function of the pressure of helium buffer gas	120
V-5	The diffusion time $\tau_{Dy} = w_y^2/4D$, $w_y = 59$ μm versus pressure of the helium buffer gas. The data have been normalized to 273 K	121
V-6	The diffusion time $\tau_{Dy} = w_y^2/4D$, $w_y = 144$ μm versus pressure of the helium buffer gas. The data have been normalized to 273 K	122
V-7	$D_{Na\text{-}He}p$ (in Torr-cm^2/sec) at 273 K is plotted as a function of helium buffer gas. The error bars indicate estimate of possible systematic error	123
V-8	The diffusion time $\tau_{Dy} = w_y^2/4D$, $w_y = 56$ μm, at 273 K versus the pressure of the argon buffer gas from 10 Torr to 50 Torr	125
V-9	The diffusion time $\tau_{Dy} = w_y^2/4D$, $w_y = 56$ μm at 273 K versus the pressure of the argon buffer gas from 25 Torr to 300 Torr	126
V-10	The diffusion time $\tau_{Dy} = w_y^2/4D$, $w_y = 100$ μm at 273 K versus the pressure of the helium buffer gas. The runs with good and bad signal-to-noise are as indicated in the figure	133

I. INTRODUCTION

The realization of single-atom detection[1-4] is perhaps one of the more important and fascinating applications of laser spectroscopy in recent years. Either the method of laser resonance fluorescence[5] or resonance ionization[6] has been used in these experiments. In both methods, the atom is first excited from ground state 1 to a low lying excited state 2 by tuning the frequency of a laser to the resonant transition of the atom. This is indicated by the broad arrows in Fig. I-1. First, consider a simple two-level atom as shown in Fig. I-1(a). After absorption of a laser photon, the excited atom would decay to the ground state 1 after a delay of 10^{-7} to 10^{-8} sec, the lifetime of the excited state 2. During this decay it emits a fluorescence photon of approximately the same frequency, as shown by the wavy arrow. During the passage through the laser beam, the atom would continue to absorb and re-emit photons many times, resulting in 10^{7} to 10^{8} spontaneously emitted photons/sec. With a detection efficiency of 1%, of the order of 10^{5} counts/sec are measurable due to the presence of a single fluorescent atom. Provided background stray light, which in this case occurs at the same frequency as fluorescence signal, is kept to a minimum, individual atoms can be detected, in the resonance fluorescence scheme, by

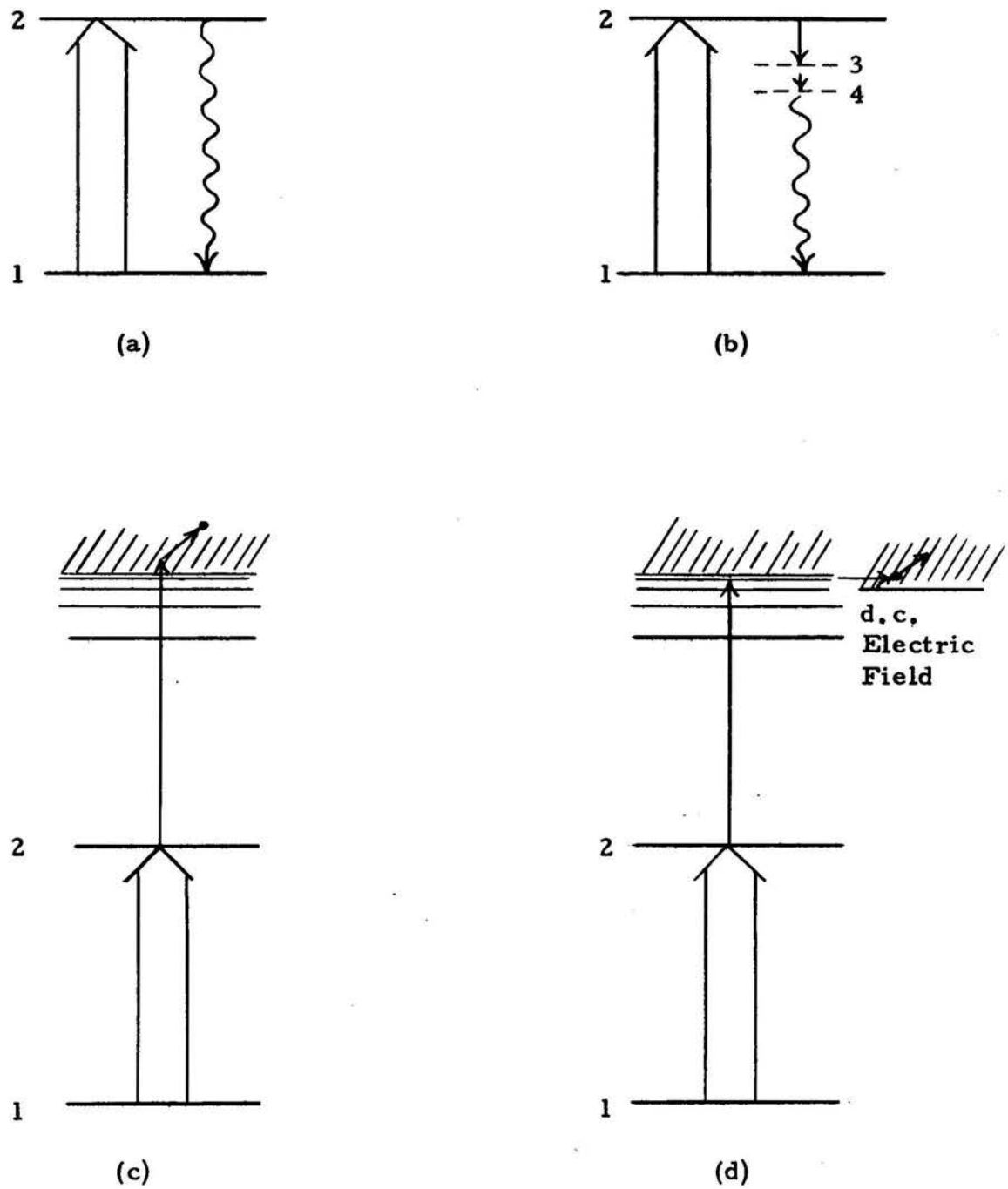

Fig. I-1. Different schemes for detecting a single atom with lasers. It may be detected by observing the emitted fluorescence photons as in (a) and (b), or by photoionization or field ionization as in (c) and (d).

registering these counts. It is possible to circumvent the stray light problem with level schemes shown in Fig. I-1(b), for atoms such as cesium. In these cases, the fluorescence frequency, represented by the wavy arrow, is different from the laser frequency. Hence, one can eliminate background stray light at the laser frequency by optical filtering when detection only at the fluorescence frequency is made. Unfortunately, the oscillator strengths of the resonant transitions of these multilevel atoms are typically 10^{-1} to 10^{-2} as compared to the order of unity for a two-level atom such as sodium. Hence, fewer fluorescence photons are available for detection.

In the resonance ionization scheme, the atom is further excited from the low lying excited state 2 into the ionization continuum either directly by another laser as shown in Fig. I-1(c), or first excited to a high-lying excited state near the ionization limit and subsequently ionized by a d.c. electric field as shown in Fig. I-1(d). Upon ionization, an electron and an ion are thus created, and the presence of a single neutral atom can then be inferred by detecting these changes using devices such as a gas proportional counter or an electron multiplier operated in vacuum.

Given the capability of single-atom detection, it is of interest to measure the velocity of a single atom in real-time. The resonance ionization scheme would not be suitable for this application, because

the atom is destroyed by ionization during the detection process. She et al.[7] first proposed the laser resonance fluorescence time-of-flight correlation technique for this type of measurement. Briefly, a dye laser which is tuned to the atomic transition is split to form two parallel beams in the region of interest. As an atom moves across the two beams, the fluorescence photons emitted by the atom would come in two sequential bursts. The digital autocorrelation function of the two detected bursts of photoelectron counts should exhibit a two-humped structure with the second hump lagging the first one by the time-of-flight of the atom from one beam to the other. If the beam separation is known, the transverse velocity of the atom can be determined. Of course, it is also possible to use just one beam for the measurement of atom's motion, in which case the width of the autocorrelation function would yield information on the transit-time of the atom across the single beam.

In this thesis, we shall present experimental evidence that, for the first time, individual sodium atoms in a helium buffer gas have been detected and their motions measured in real-time by the resonance fluorescence correlation technique. We have not yet been able to measure the flow velocity of such a sodium atom because diffusion is faster than the mean flow in our present experimental set-up. As a result, instead of measuring single-atom flow velocities, we actually measured the transit-time of a sodium atom

diffusing across the laser beam. By averaging over the fluorescence emission of many sodium atoms, we were able to measure the binary diffusion coefficients of Na in He and Na in Ar. The pressure dependence of these coefficients was also investigated. To our knowledge, this is the first time that diffusion coefficients of gaseous systems have been measured in this manner.

The organization of this thesis is as follows: The basic theory behind laser resonance fluorescence and digital correlation techniques is described in Chapter II. In Chapter III, the experimental aspects are discussed in detail. Results and analysis of our single-atom detection with transit-time measurements and diffusion coefficient measurements are presented in Chapter IV and Chapter V, respectively. Finally, conclusions and suggestions for future work are presented in Chapter VI.

II. THEORY

In this chapter, the theory of the laser resonance fluorescence correlation technique employed in this study is presented. The first section describes the general principles of laser resonance fluorescence for a two-level system; these principles are applied to sodium atoms in a helium flow. In the second section, the principles of single- and double-burst correlation techniques for velocity and transit-time measurements are reviewed. Finally, the ensemble-averaged autocorrelation function for diffusing sodium atoms in a helium buffer gas is derived in section 3; it is shown to be a means for measuring the diffusion coefficient of sodium atoms in helium.

2.1 Resonance Fluorescence of Sodium Atoms in a Helium Flow

Consider the interaction of monochromatic radiation of intensity I and frequency ν with a two-level atom as shown in Fig. I-1(a). The population and degeneracies of the two levels are N_1, g_1 and N_2, g_2 respectively. If we assume the total population of the two levels, i.e., $N = N_1 + N_2$, remains constant in time, the rate of change of N_2 is equal to the difference between the rate of absorption upwards to level 2, $N_1 B_{12} I$, and the rate of downward transition to level 1 (both spontaneous, $N_2 A_{21}$, and stimulated, $N_2 B_{21} I$), i.e.

$$\frac{dN_2}{dt} = N_1 B_{12} I - (A_{21}+B_{21} I) N_2 \ , \qquad (2.1)$$

where B_{12} and B_{21} are Einstein coefficients for absorption and stimulated emission respectively, and A_{21} is the Einstein coefficient for spontaneous emission. Under steady state conditions, $\frac{dN_2}{dt} = 0$. We find from Eq. (2.1),

$$\frac{N_2}{N} = \frac{B_{12} I}{A_{21} + (B_{12}+B_{21})\ I} \ . \qquad (2.2)$$

Noting that $g_1 B_{12} = g_2 B_{21}$, and defining the saturation intensity I_s as the intensity required to make N_2/N equal to $1/2$ of its maximum value, i.e.,

$$I_s = \frac{A_{21}}{B_{12}\,(1+g_1/g_2)} \ , \qquad (2.3)$$

then Eq. (2.2) becomes,

$$\frac{N_2}{N} = \frac{1}{(1+g_1/g_2)} \left(\frac{I/I_s}{1+I/I_s} \right) \ . \qquad (2.4)$$

The rate at which spontaneously emitted fluorescence photons per atom is given by

$$R = \left(\frac{N_2}{N} \right) A_{21} = R_s \ \frac{I/I_s}{1 + I/I_s} \ . \qquad (2.5)$$

The quantity

$$R_s = A_{21}\left(\frac{g_2}{g_1+g_2}\right) \tag{2.6}$$

is the saturated fluorescence rate. This is the maximum rate possible and occurs when $I >> I_s$. The saturation intensity, I_s, can be written as,

$$I_s = \frac{8\pi hc}{(1+g_2/g_1)\,\lambda^3\, g(\nu)}\ , \tag{2.7}$$

where the relation $B_{21} = \frac{c^2 g(\nu)}{8\pi h\nu^3} A_{21}$ [7] has been used. $g(\nu)$ is the normalized line shape function for the transition.

For a TEM_{oo} laser beam, the laser intensity has a Gaussian spatial profile, $I = I_o \exp(-2r^2/w^2)$. The beam radius, w, is the radius where the intensity falls to $1/e^2$ of its maximum value I_o; $P_o = \frac{1}{2}\pi w^2 I_o$ is the laser power. An atom with a velocity component v normal to the beam, making a transit through the center of the beam, i.e., $r = v\,t$, will emit a total number of photons,

$$F = \int_{-\infty}^{\infty} R\, dt\ .$$

Using Eq. (2.5), this becomes

$$F = R_s \int_{-\infty}^{\infty} \frac{(I_o/I_s)\, dt}{e^{2r^2/w^2} + I_o/I_s} \,. \tag{2.8}$$

If we let $I_o/I_s = x$, and $u^2 = 2r^2/w^2$, Eq. (2.8) becomes,

$$F = \frac{R_s w_s}{\sqrt{2}\, v} f(I_o/I_s) \,, \tag{2.9}$$

where $w_s = w (I_o/I_s)^{\frac{1}{2}} = (2P_o/\pi I_s)^{\frac{1}{2}}$, is the beam spot size which, for a given power, P_o, produces I_s at the beam center. The dimensionless function, f, is defined by

$$f(x) = \sqrt{x} \int_{-\infty}^{\infty} \frac{du}{e^{u^2} + x} \,. \tag{2.10}$$

A plot of this function is shown in Fig. II-1. It ranges from .16 to 1.12 for a wide range of experimental conditions (I_o/I_s = 0.01 to 1000) and assumes a maximum value of 1.12 at $I_o/I_s = 1.91$.

Typical atoms cross the laser beam at some impact parameter b from the beam center. This means $r^2 = b^2 + v^2 t^2$ instead of $r^2 = v^2 t^2$ as was assumed above. The total number of fluorescence photons emitted then becomes

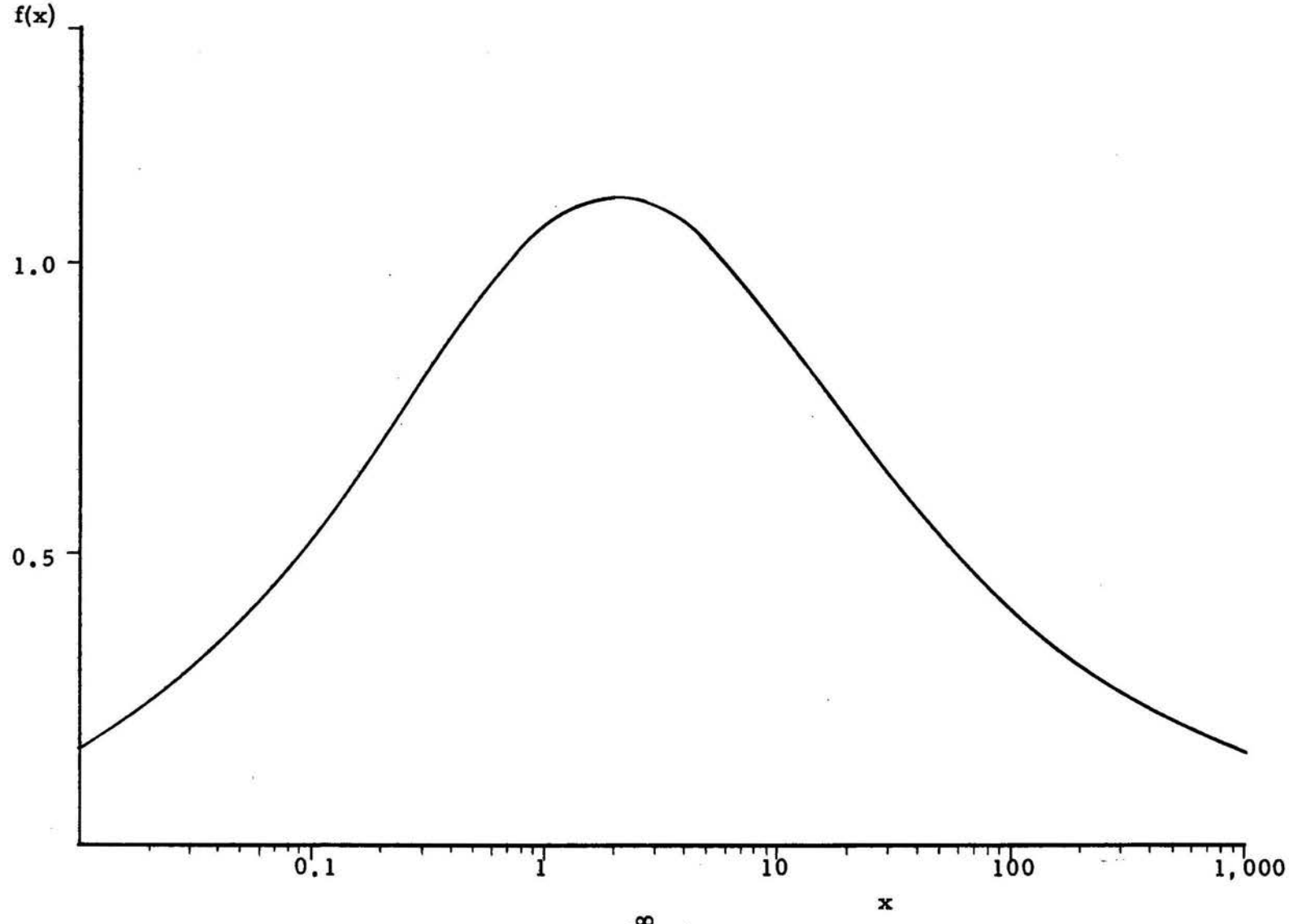

Fig. II-1. The function $f(x) = \sqrt{x} \int_{-\infty}^{\infty} \frac{du}{e^{u^2} + x}$ vs x, $0.01 \leq x \leq 1,000$.

$$F_b = R_s \int_{-\infty}^{\infty} dt \frac{e^{-2v^2t^2/w^2}}{1+\left(\frac{I_o}{I_s} e^{-2b^2/w^2}\right)\left(e^{-2v^2t^2/w^2}\right)} \cdot \left(\frac{I_o}{I_s} e^{-2b^2/w^2}\right) . \qquad (2.11)$$

If we let $y = (I_o/I_s)\, e^{-2b^2/w^2}$ and $u^2 = 2v^2t^2/w^2$, Eq. (2.12) becomes,

$$F_b = \frac{R_s w_s}{\sqrt{2}\, v} e^{-b^2/w^2} f(y) \qquad (2.12)$$

where $f(y)$ is the same function as given in Eq. (2.10).

In Fig. II-2, the normalized function F_b/F versus b/w for $I_o/I_s = 1.91$ is shown. F_b/F, hereafter referred to as $f_2(b/w)$, will be used later in Chapter III for the determination of the sodium level and for probability analysis of the detected fluorescence counts in Chapter IV. For trace atoms seeded in a carrier gas with mean flow velocity v, normal to the laser beam, all values of impact parameters are possible when enough atoms are considered. Fig. II-3 plots F_b/F as a function of the percentage of the emitted fluorescence photons with bursts larger than or equal to F_b under the optimum condition, $I_o/I_s = 1.91$. From Fig. II-3, we conclude

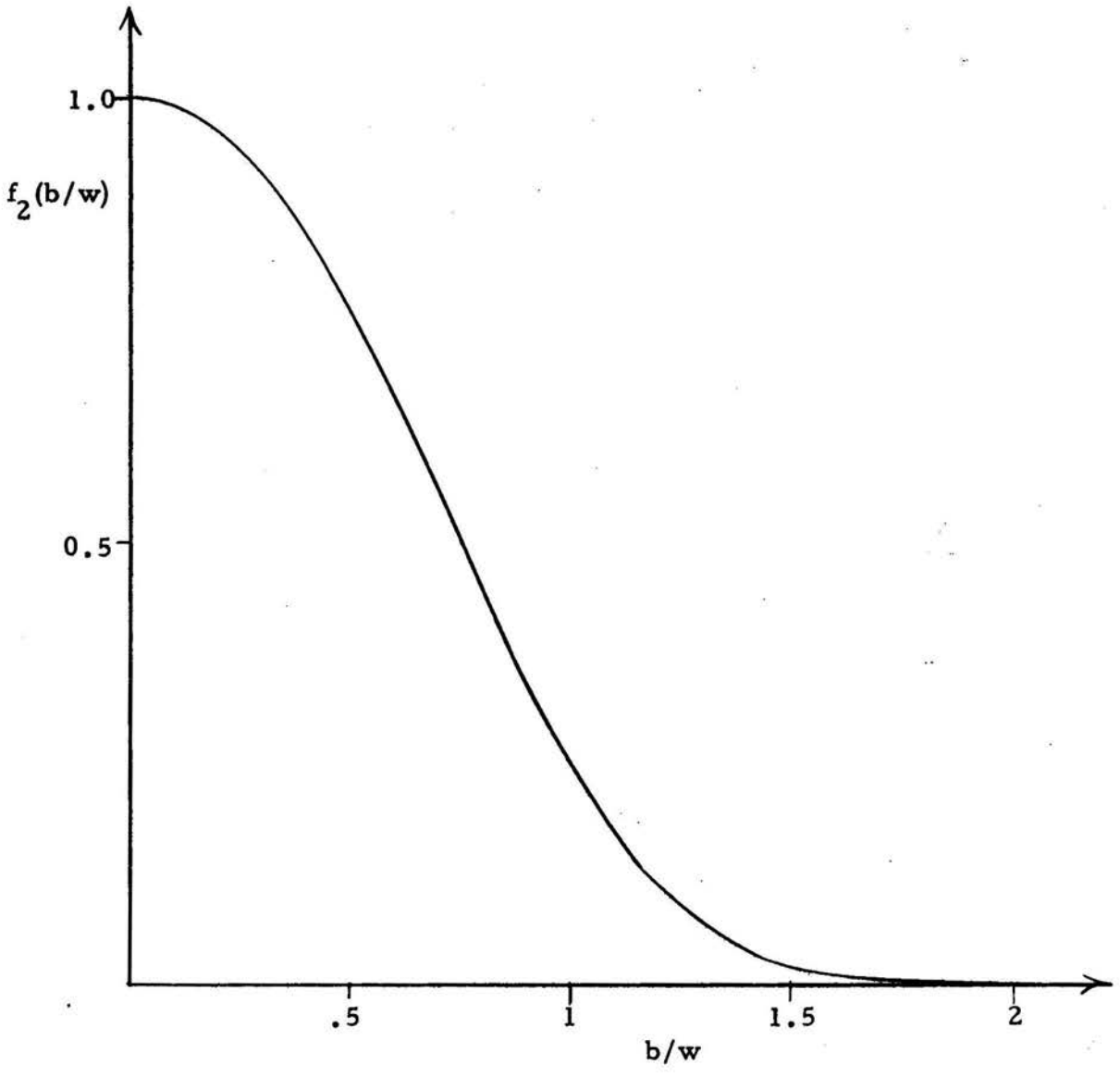

Fig. II-2. The function $f_2(b/w) = F_b/F$ vs b/w, $0 \leq b/w \leq 2$.

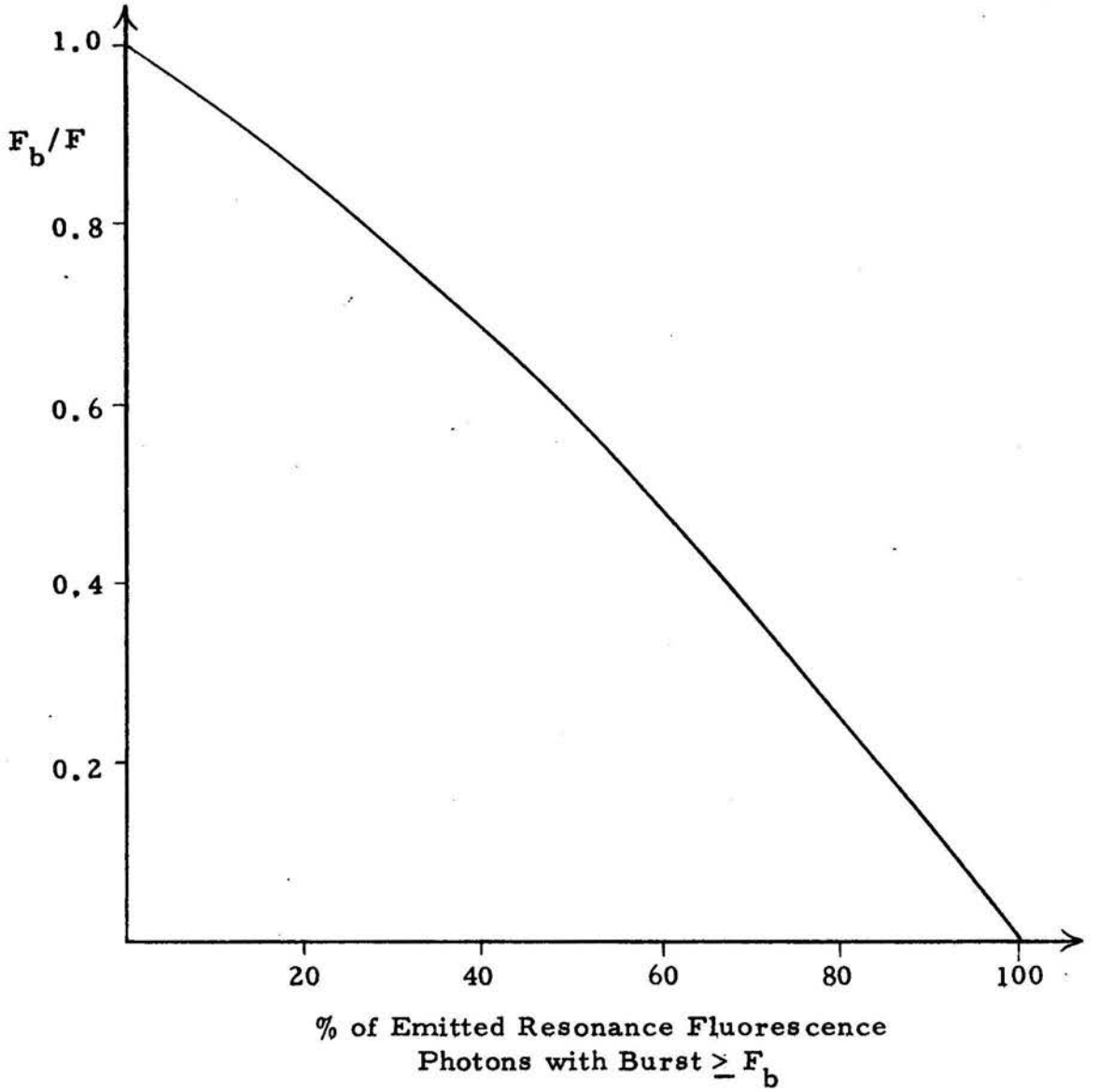

Fig. II-3. F_b/F as a function of the percentage of emitted fluorescence photons with bursts larger than or equal to F_b.

that 50% of the emitted fluorescence photons would occur in bursts with $F_b \geq 0.6\,F$ when they cross the beam.

So far, we have only considered the case for which the flow velocity is sufficiently high so that the transit-time for an atom with $b = 0$ due to the mean flow, $\tau_f = 2w/v$, is much shorter than the diffusion time, $\tau_D = w^2/4D$, the time a diffusing atom stays in the beam, where D is the diffusion coefficient. The trajectory of the atom in this case is approximately linear. In the other limit, i.e., for $\tau_D \ll \tau_f$, the motion of the atom across the beam takes a random zigzag path dominated by atomic collisions. In that case, there is no well-defined velocity for use in Eq. (2.9).

As a rough approximation, we can use an effective velocity v_{eff}, $v_{eff} \cong w/\tau_D$, with which Eq. (2.9) becomes

$$F \approx \frac{R_s}{\sqrt{2}}\,\tau_D\left(\frac{I_o}{I_s}\right)^{\frac{1}{2}}\,f\left(\frac{I_o}{I_s}\right). \tag{2.13}$$

It should be pointed out that because of the haphazard motion of diffusion, the emitted fluorescence rate as the atom diffuses in and out of the beam is not necessarily a Gaussian function in time as has been assumed in deriving Eqs. (2.9) and (2.11). Furthermore, the concept of an impact parameter, b, is meaningless in this case. Nevertheless, Eq. (2.13) is useful in providing a rough estimate for fluorescence photons emitted during a transit.

In our experiments, we typically study the motion of sodium atoms in 200 Torr of helium. At this pressure, the sodium D_2 line at 5890Å is much broader than its hyperfine structure and can be considered as a two-level atom. In this case, $g_2/g_1 = 2$, $\tau = 1/A_{21} = 16.035 \pm .2$ n sec,[8] and $R_s = 4.16 \times 10^7$ sec^{-1} from Eq. (2.6). When the laser is tuned to the peak of the absorption line, $\nu = \nu_o$, the normalized line-shape function in Eq. (2.7) becomes[9]

$$g(\nu=\nu_o) = \left(\frac{2}{\Delta\nu_D}\right)\left(\frac{\ell n 2}{\pi}\right)^{\frac{1}{2}} \exp\left[\ell n 2 \left(\frac{\Delta\nu_L}{\Delta\nu_D}\right)^2\right]\left[1 - \text{erf}\sqrt{\ell n 2}\left(\frac{\Delta\nu_L}{\Delta\nu_D}\right)\right], \tag{2.14}$$

where $\Delta\nu_D$ and $\Delta\nu_L$ are Doppler- and pressure-broadened linewidth respectively.

Fig. II-4 shows an experimental pressure-broadened profile of the sodium D_2 line at 200 Torr of He. Normalizing by integrating the area under the curve, we find $g(\nu=\nu_o) = 1.51 \times 10^{-10}$ sec. At 300 K, the Doppler linewidth of sodium D_2 line is $\Delta\nu_D = 1.31$ GHz. Using Eq. (2.14), $\Delta\nu_L = 3.93$ GHz. Substituting into Eq. (2.7, we find $I_s = 5.4$ W/cm^2. Actually, both $\Delta\nu_D$ and $\Delta\nu_L$ are temperature dependent. In our experiments, it was necessary to heat up the sodium side pocket on the flow cell to a different extent in different runs in order to drive sodium atoms into the helium flow. As a

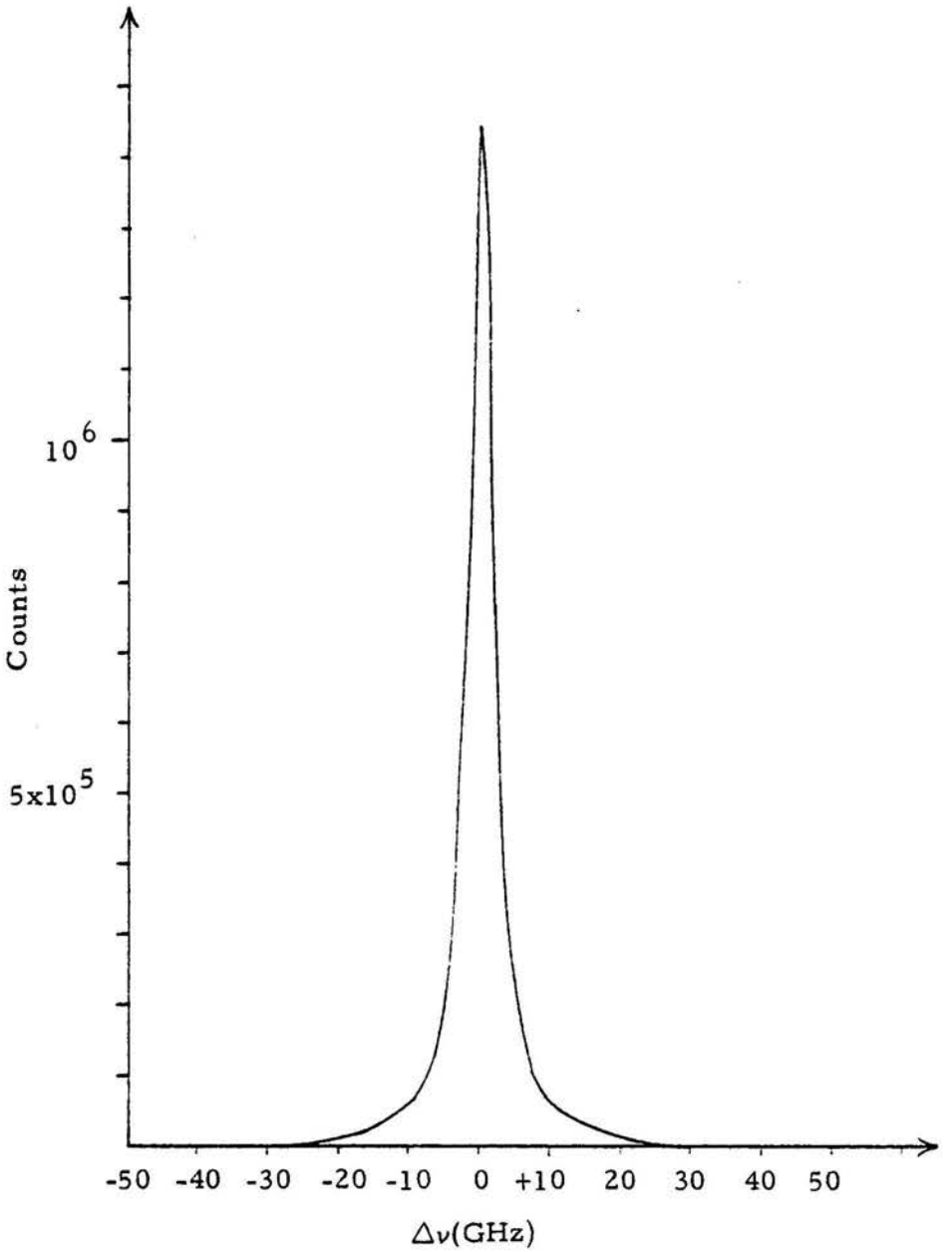

Fig. II-4. Pressure-broadened sodium D_2 line at 200 Torr of helium.

result, the temperature in our flow cell varied slightly in different experimental runs. Nevertheless, the number given above for I_s can be used as a reasonable estimate in calculating the optimum beam radius, laser power, and the expected number of fluorescence photons per transit.

As a numerical example, let us consider a hypothetical case with experimental parameters similar to our measurements to be described in Chapter IV. A sodium atom with normal velocity $v = 100$ cm/sec in 200 Torr of helium pass through two laser beams separated by 800 μm with beam radius $w = 50$ μm. Since the function $f(I_o/I_s)$ assumes a maximum value of 1.12 for $I_o/I_s = 1.91$), naturally one should try to make $I_o = 1.91\ I_s$, or 10.3 w/cm^2. This corresponds to using 0.4 mW of laser power per beam. Eq. (2.9) then predicts 2275 photons would be emitted by the sodium atom traversing the center of one laser beam or 4550 photons if it passes through the centers of both beams. At a detection efficiency of 1%, we should then obtain 46 signal counts above background due to the presence of the sodium atom. As a comparison, typically we observed 20-50 signal counts in the recorded correlation functions. These are discussed in Chapter IV.

2.2 Single-Atom Burst Correlation Technique

In any type of optical spectroscopy in which quantum photodetectors are employed, signal processing involves extracting

information contained in a train of pulses in time, each pulse representing one photo-detection event. For a constant light level, the number of these pulses in a fixed time interval will assume a Poisson distribution due to the random nature of the photo-electric effect. An atom crossing the laser beam tuned to the atomic transition, however, would produce a burst of fluorescence photons. The corresponding photoelectron pulses or counts would be "bunched together" and correlated in time. Hence, a computation of the autocorrelation function of the digital pulse train would extract information about the bunched fluorescence photons, from which the motion of the atom could be deduced.

The autocorrelation function of the detected photocount rate, $i(t)$, is defined as

$$R(\tau) = \lim_{T \to \infty} \frac{I}{T} \int_{-T/2}^{T/2} i(t)\ i(t-\tau)\, dt$$

$$= \langle i(t)\ i(t-\tau) \rangle , \qquad (2.15)$$

that is, $i(t)$ is multiplied by a delayed version of itself $i(t-\tau)$, and the product is averaged over T seconds. The parameter τ is the delay time. The brackets indicate a time-average. In a digital correlator, the time-axis is divided into uniform sampling intervals of duration ΔT, the sample time. The time-average in Eq. (2.15)

is then approximated by summing a finite number, N_T, of sampled products of the number of detected photocounts, $C(t)$, in time ΔT, where

$$C(t) \cong \Delta T\,[i(t)] \quad . \tag{2.16}$$

A digital representation of the correlation function for delay time $\tau = m\Delta T$, m being an integer, can then be obtained. In terms of $C(t)$, the autocorrelation function Eq. (2.15) is now approximated as,

$$R(m\Delta T) = \frac{1}{N_T \Delta T} \sum_{q=1}^{N_T} \frac{C(q\Delta T)}{\Delta T} \frac{C((q-m)\Delta T)}{\Delta T} \Delta T$$

$$= \frac{1}{N_T (\Delta T)2} \sum_{q=1}^{N_T} C(q\Delta T)\, C((q-m)\Delta T) \quad . \tag{2.17}$$

For sufficiently small ΔT and sufficiently large N_T, $R(m\Delta T)$ approaches the integral form given in Eq. (2.15).

In order to speed up the digital multiplication and calculate correlation in real-time, $R(m\Delta T)$ is usually evaluated by using a one-bit quantization scheme called single-clipping. We employed such a single-clipped digital correlator in our experiments. Its operating principles will be described in Sec. III-5. In this

instrument, $C(q\,T - m\Delta T)$ is replaced by the clipped version, $C_k(q\Delta T - m\Delta T)$ which is defined by,

$$C_k(q\Delta T - m\Delta T) = \begin{cases} 1 & \text{if } C(q\Delta T - m\Delta T) > k \\ 0 & \text{if } C(q\Delta T - m\Delta T) \leq k \end{cases}, \qquad (2.18)$$

where k is a preset integer called the clipping level. In an actual experiment, the mth store channel of the single-clipped digital correlator displays the clipped correlation function,[10]

$$R_k(m\Delta T) = \sum_{q=1}^{N_T} C(q\Delta T)\, C_k(q\Delta T - m\Delta T) . \qquad (2.19)$$

This is, besides a multiplicative constant, often a reasonably good approximation to Eqs. (2.15) and (2.17).

Previous workers,[10, 11] by comparing actual measurements with computer simulation of an ideal digital correlator, found that the error in determining characteristic relaxation time (e.g., diffusion time), τ_r, of the system under study using single-clipping is typically less than 1% if the clipping level k is set less than or equal to $\overline{C}$, the average photocounts per sample. They treated the case of Gaussian statistics and deals with long-time averaged correlation functions. In general, it was found to be good practice to make $\Delta T/\tau_D \leq 0.1$ and the number of photocounts per relaxation time ≥ 10. In our diffusion coefficient measurements, which deals

with long-time averaged correlation functions, we generally have $\Delta T/\tau_D \leq 0.2$ and the number of photocounts per diffusion time $\simeq 1$. No detailed experimental study concerning the effect of clipping on velocity measurements has appeared to our knowledge. Remote wind speed measurements with large dust particles using single-particle correlation technique[12, 13] with two laser beams yielded velocities in excellent agreement with the average wind speed measured with a conventional anemometer. In these cases, burst correlation due to dust particles were measured and the clipping level was set below signal counts but above the average noise counts.

Now let us consider the case in which an atom with mean flow velocity v in the x-direction, $x(t) = vt$, is making a transit across a single laser beam with Gaussian profile, i.e.,

$$I = I_o e^{-2(x^2(t)+b^2)/w^2} = I_o e^{-2(v^2t^2+b^2)/w^2} , \qquad (2.20)$$

where b is the impact parameter. Substituting Eq. (2.20) into Eq. (2.5), we find that for the unsaturated case, $I_o << I_s$, the temporal evolution of the rate of fluorescence photocounts by the atom along its path would also have a Gaussian profile,

$$i(t) \simeq i_o e^{-2v^2t^2/w^2} , \qquad (2.21)$$

where $i_o = R_s \left(\frac{I_o}{I_s} \right) e^{-2b^2/w^2} \epsilon \eta$. ϵ and η are optical collection and photon counting efficiencies, respectively. The count rate i (t) has the interesting property that its halfwidth in time is independent of the path the atom took, as long as it is a linear trajectory. Using Eq. (2.21) in Eq. (2.15), the photocount autocorrelation function can be evaluated,

$$R(\tau) = \frac{i_o^2}{T} \int_{-T/2}^{T/2} e^{-2v^2 t^2/w^2} e^{-2v^2 (t-\tau)^2/w^2} dt$$

$$= i_o^2 e^{-v^2 \tau^2/w^2} \left[\frac{1}{T} \int_{-T/2}^{T/2} e^{-v^2 (2t-\tau)^2/w^2} dt \right]$$

$$= i_o^2 e^{-v^2 \tau^2/w^2} \left[\frac{\sqrt{\pi}}{2} \frac{1}{T} (w/v) \operatorname{erf} (v/w (T-\tau)) \right]$$

$$= \text{constant} \cdot e^{-v^2 \tau^2/w^2} . \qquad (2.22)$$

Thus R (τ) has a Gaussian profile that peaks at $\tau = 0$ and with a width in time $\sqrt{2}$ times larger than the width of the corresponding fluorescence burst. If the signal is treated digitally, for small ΔT we have,

$$C(t) \simeq C_o e^{-2v^2 t^2/w^2} , \qquad (2.23)$$

where $C_o = (R_s \Delta T) \frac{I_o}{I_s} e^{-2b^2/w^2} \epsilon \eta$. Substituting in Eq. (2.17),

$$R(m\Delta T) = i_o^2 \sum_{q=1}^{N_T} \frac{1}{N_T} e^{-2v^2(q\Delta T)^2/w^2} e^{-2v^2(q-m)^2\Delta T^2/w^2}$$

$$= \frac{i_o^2}{N_T} e^{-v^2(m\Delta T)^2/w^2} \sum_{q=1}^{N_T} e^{-v^2(2q-m)^2\Delta T^2/w^2} . \quad (2.24)$$

For sufficiently large N_T, the sum in Eq. (2.24) is essentially a constant. Hence, $R(m\Delta T)$ is also a Gaussian function with the same width in time as $R(\tau)$. The transit time of the atom across the beam, $\tau_f = 2w/v$, and its velocity v can thus be determined simply by measuring the width of $R(\tau)$ or $R(m\Delta T)$.

A typical single-beam correlation function we measured due to a dust particle is shown in Fig. II-5(a). For dust particles, the diffusion time is much longer than a typical transit time because the particles are so large. Also, no saturation phenomenon is involved in dust particle scattering. Thus, the above equations are valid with the constants i_o^2 now proportional to the square of the scattering cross-section of the particle. In Fig. II-5(a), the time when the correlation function drops to $1/e^2$ is 1.7 msec. The beam radius w is equal to 144 μm. Hence, its velocity is 12 cm/sec. Comparing

Fig. II-5(a). A typical single-beam correlation function due to a dust particle. The beam width is w = 144 μm. Flow velocity determined from $1/e^2$ point of the correlation function is 12 cm/sec.

(b). A correlation function obtained with two laser beams due to a dust particle. The two beams of radii w = 125 μm are separated by 500 μm. The velocity as determined from the separation of the two humps and the $1/e^2$ points of each hump are 18 cm/sec and 12 cm/sec, respectively.

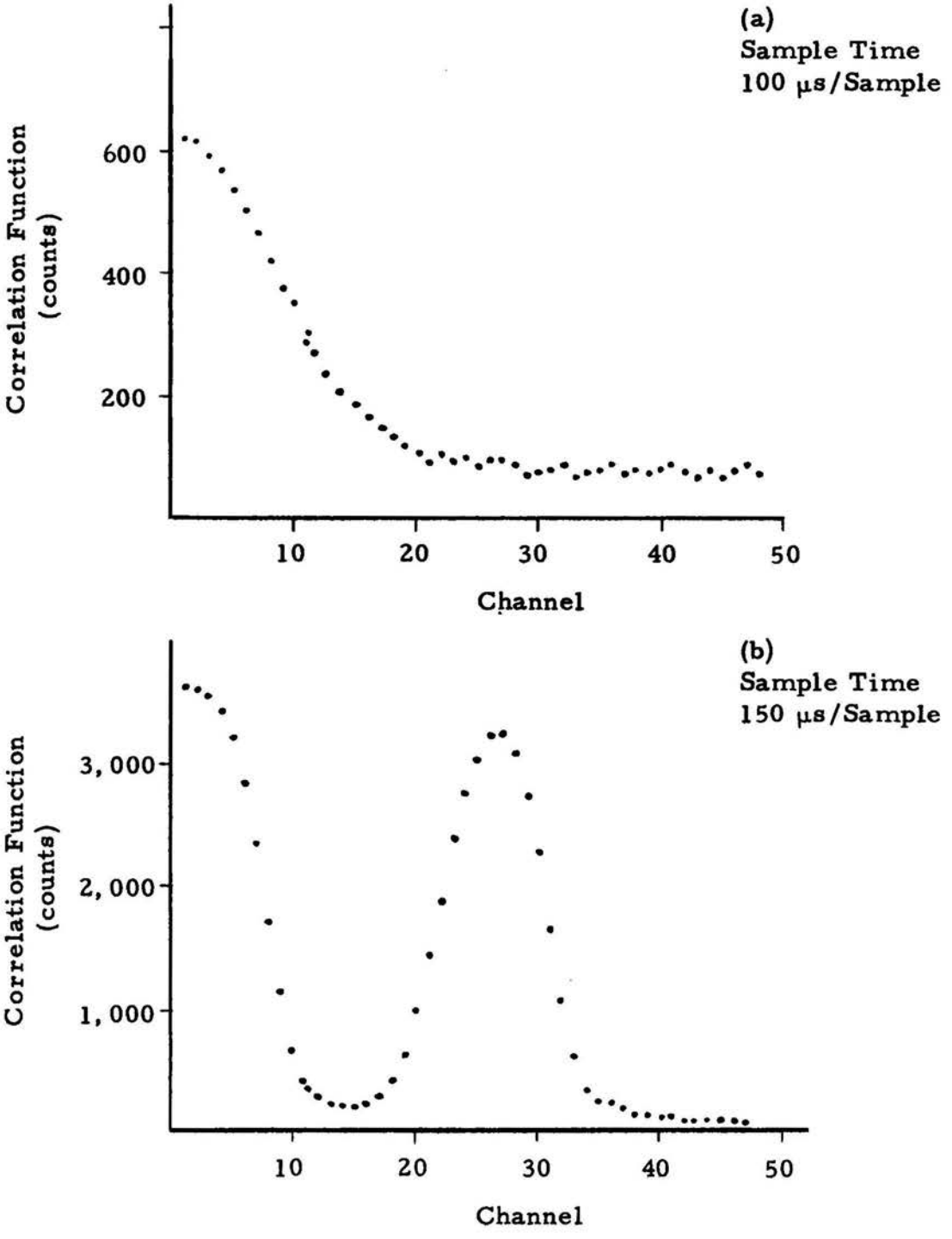
(a)
Sample Time
100 μs/Sample
Correlation Function
(counts)
600
400
200
10
20
30
40
50
Channel
(b)
Sample Time
150 μs/Sample
Correlation Function
(counts)
3,000
2,000
1,000
10
20
30
40
50
Channel

the counts in channel 0 to the background, one can see that the total signal of the burst is about 550 counts.

The reasoning behind the above estimate of signal counts due to a particle from an experimentally observed single-clipped correlation function is as follows. Let us consider the case in which the clipping level k is set such that $C_k(q\Delta T) = 1$ during the transit of the particle across the laser beam and $C_k(q\Delta T) = 0$ in most of the other samples during the measurement time, $N_T\Delta T$. In Fig. II-6 we show the $C(q\Delta T)$ pulse train with clipping level k and the corresponding single-clipped correlation function $R_k(m\Delta T)$. From Eq. (2.19), we find that the content of the zeroth channel, $R_k(0)$ is

$$R_k(0) = \sum_{q=q_i}^{q_f} C^{burst}(q\Delta T)\,(1) + \sum_{q=1}^{N_T} C^{bkg}(q\Delta T)\,(1)$$

$$= \begin{array}{l}\text{total signal counts}\\ \text{in the burst due to the}\\ \text{transit of the atom}\end{array} + \begin{array}{l}\text{total background}\\ \text{counts exceeding}\\ \text{clipping,}\end{array} \qquad (2.25)$$

where q_i and q_f are initial and final samples for the burst. The quantity $C^{burst}(q\Delta T)$ is the number of signal counts in the qth sample of the burst, whereas $C^{bkg}(q\Delta T)$ is the background count in the qth sample above clipping. Since background counts are uncorrelated, they appear in all the channels. Hence, a comparison

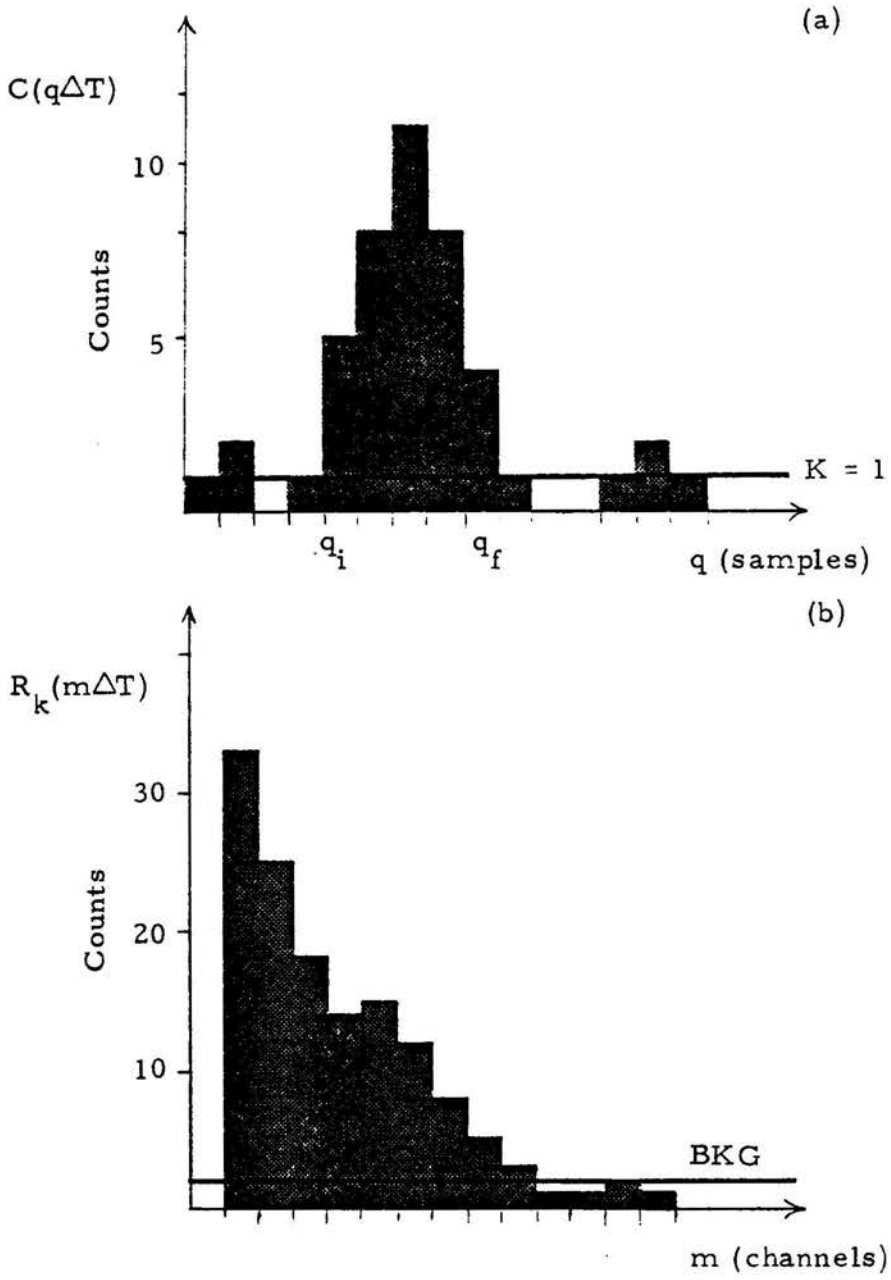

Fig. II-6(a). The detected pulse train C(qΔT) showing a burst of 31 counts above clipping level k = 1 with initial and final samples q_i and q_f.

(b). The single-clipped correlation function R_k(mΔT) obtained with the pulse train C_k(qΔT). The average background level is indicated by the line marked BKG.

of $R_k(0)$ with the latter channels gives the total signal counts due to the burst. $R_k(0)$ is not displayed in our correlator. A reasonable estimate of $R_k(0)$ can be obtained, however, by examining the first few channels of the correlator and knowledge about the shape of the correlation functions, e.g., Gaussian, bell-shaped, etc.

If two Gaussian laser beams with separation ℓ are used, the laser intensity distribution experienced by an atom crossing both beams at impact parameter b and with transverse velocity v would be,

$$I(t) = I_o \left\{ \exp\left[-2\left(\frac{x^2(t)+b^2}{w^2}\right)\right] + \exp\left[-2\left(\frac{(x(t)-\ell)^2+b^2}{w^2}\right)\right]\right\} . \tag{2.26}$$

Following Eq. (2.23), the total fluorescence photocount rate is written as,

$$i(t) = i_1(t) + i_2(t) , \tag{2.27}$$

with $$i_1(t) = i_o e^{-2v^2t^2/w^2} \tag{2.28}$$

and $$i_2(t) = i_1(t-\tau_f) \tag{2.29}$$

where $\tau_f = \ell/v$ is the time-of-flight of the atom between the two beams. The correlation function $R(\tau)$ becomes

$$R(\tau) = \langle i(t)\, i(t-\tau) \rangle$$

$$= \langle (i_1(t) + i_2(t))\, (i_1(t-\tau) + i_2(t-\tau)) \rangle$$

$$= \langle i_1(t)\, i_1(t-\tau) \rangle + \langle i_2(t)\, i_2(t-\tau) \rangle + \langle i_1(t)\, i_2(t-\tau) \rangle$$

$$+ \langle i_2(t)\, i_1(t-\tau) \rangle \ . \qquad (2.30)$$

The first two terms are just autocorrelation signals arising from the atom traversing each beam, i.e., $R_{11}(\tau)$ and $R_{22}(\tau)$. The last two terms are cross-correlation between signals from both beams, i.e. $R_{12}(\tau)$ and $R_{21}(\tau)$ respectively. Eq. (2.30) can now be rewritten as,

$$R(\tau) = R_{11}(\tau) + R_{22}(\tau) + R_{12}(\tau) + R_{21}(\tau) \ . \qquad (2.31)$$

Using Eq. (2.30),

$$R_{22}(\tau) = \langle i_1(t-\tau_f)\, i_1(t-\tau_f-\tau) \rangle$$

$$= \langle i_1(t')\, i_1(t'-\tau) \rangle$$

$$= R_{11}(\tau) \ , \qquad (2.32)$$

where $t' = t-\tau_f$. Similarly,

$$R_{12}(\tau) = \langle i_1(t)\, i_1(t-\tau_f-\tau)\rangle$$

$$= R_{11}(\tau+\tau_f) \qquad (2.33)$$

and

$$R_{21}(\tau) = \langle i_2(t)\, i_2(t-\tau+\tau_f)\rangle$$

$$= R_{22}(\tau-\tau_f)$$

$$= R_{11}(\tau-\tau_f)\ . \qquad (2.34)$$

Substituting into Eq. (2.31), we have

$$R(\tau) = 2R_{11}(\tau) + R_{11}(\tau+\tau_f) + R_{11}(\tau-\tau_f)\ . \qquad (2.35)$$

Our earlier discussion on single-beam correlation functions indicates $R_{11}(\tau)$ peaks at $t = 0$. In the two-beam case, then, Eq. (2.35) tells us that we would have one central peak at $t = 0$ and two symmetrically displaced peaks at $t = \pm\tau_f$ respectively. All digital correlators we know of display only the portion of the correlation function with $t > 0$. Hence, the correlation function due to an atom traversing both laser beams should exhibit a two-hump structure. If the two bursts of fluorescence photons are of equal magnitude, the peak centered at $t = 0$ should be twice as high as the one at $t = \tau_f$, as indicated in Eq. (2.35).

We have also recorded correlation functions for which the first peak is only slightly higher than the second peak. This corresponds to the case in which the first burst of photons is much smaller than the second burst, while both bursts exceed the clipping level. The particular way with which the single-clipped correlator computes the correlation function is primarily responsible for this artifact. An example of this type of correlation functions due to a dust particle is shown in Fig. II-5(b). The two beams of radius $w = 125\ \mu m$ are separated by $700\ \mu m$. From the position of the second peak, we can see that $\tau_f \simeq 4$ ms. Hence, $v = \ell/\tau_f = 18$ cm/sec. The total signal counts are about 3500. From the width of each peak, we find $v = 12$ cm/sec. This was one of the earliest correlation functions we obtained. The agreement with theory was much better for the two-beam type correlation functions for dust particles we obtained later on. Several examples are shown in Fig. IV-3.

When we are looking for single atoms, we usually set the incident laser power P_o such that $I_o/I_s \simeq 1.91$, in order to obtain the maximum signal. At this saturation level, the profile of the resonantly scattered fluorescence photons would not be exactly Gaussian. It would be flattened on the top due to saturation. If, in addition, there are only a few counts per burst above noise, additional errors would arise in a velocity determination using the widths of the humps due to the uncertainty in determining the width of the

correlation function. On the other hand, the separation of the two humps in two-beam type correlation functions can be determined with higher accuracy. It is not dependent on the shape of the humps. Therefore, the two-beam configuration is generally favored for velocity measurement.

When diffusion is dominant, the expressions for correlation functions derived above are no longer valid. Still, a burst of photons is detected when a sodium atom diffuses in and out of a laser beam. The corresponding correlation function should have a one-hump structure. In general, it is not a Gaussian function. As a rough estimate, though, the transit time can still be defined to be the time when the peak of the correlation function drops to $1/e^2$ of its value. We shall see below that by averaging diffusion transit times, we can measure the diffusion coefficient for the atom-gas system.

2.3 Ensemble-Averaged Correlation Function

The ensemble-averaged or long-time averaged correlation functions can be used to investigate the statistics of the dynamical properties of the system under study, such as diffusion or the turbulence level in a flow. Our interest arises from the need to determine whether diffusion or flow is dominant in our apparatus. When flow is dominant, information on the mean flow velocity is obtained from the averaged correlation function which is of the same form as those described in Sec. 2.2. When diffusion is dominant, an average time

for the atom diffusing in and out of the laser beam is obtained, from which the diffusion coefficient of the system can be deduced. The theoretical expression of the averaged correlation function for diffusion is derived in this section.

To obtain time-averaged correlation functions, it is not necessary to keep the sodium concentration at single-atom level. The correlation in the fluctuation of the number of sodium atoms in the observation volume gives the same average correlation function as an average over individual sodium atoms for a long period of time. A similar technique was used by D. Madge et al.[14, 15] to study the diffusion rate of Rhodamin 6G molecules in water solution and the chemical reaction rate for forming EtBr-DNA complex. A general review on the statistical properties of scattered light can be found in ref. 16.

We will consider the case in which diffusion is dominant and flow is negligible. Experimentally, the correlation function is averaged for a time much longer than the average diffusion time for an atom, τ_D. Theoretically, this is obtained by taking the ensemble average over all possible motions of the atoms. Using a modified version of Eq. (2.21) in Eq. (2.15), the correlation function for diffusing atoms can be written as

$$R(\tau) = i_o'^2 \left\langle e^{-2r^2(t)/w^2} \, e^{-2r^2(t-\tau)/w^2} \right\rangle . \qquad (2.36)$$

where $i_o' = R_s\left(\frac{I_o}{I_s}\right)\epsilon\,\eta$ and the brackets indicate ensemble average. Let us consider an atom at position $\underset{\sim}{r}_1(t)$ at time t. At time $t-\tau$ it was at position $\underset{\sim}{r}_2(t-\tau)$, i.e.

$$\underset{\sim}{r}_2(t-\tau) = \underset{\sim}{r}_1(t) - \Delta\underset{\sim}{r}(\tau) \quad . \tag{2.37}$$

Taking the ensemble average over all possible $r_1(t)$ and $r_2(t-\tau)$'s of the diffusing atoms, Eq. (2.37) becomes[16]

$$R(\tau) = i_o'^2 \int d\underset{\sim}{r}_1(t) \int d\Delta\underset{\sim}{r}(\tau)\, P(\Delta\underset{\sim}{r}, \tau \,|\, \underset{\sim}{r}_1, t)\, P(\underset{\sim}{r}_1, t)\, e^{-2r_1^2(t)/w^2}$$

$$\cdot\, e^{-2(\underset{\sim}{r}_1(t) - \Delta\underset{\sim}{r}(\tau))^2/w^2} \quad , \tag{2.38}$$

where $P(\underset{\sim}{r}_1, t)$ is the probability density that an atom is at $(\underset{\sim}{r}_1, t)$ and $P(\Delta\underset{\sim}{r}, \tau \,|\, \underset{\sim}{r}_1, t)$ is the probability density that an atom at $(\underset{\sim}{r}_1, t)$ in unit volume $d(\Delta\underset{\sim}{r}(\tau))$ was at $(\underset{\sim}{r}_1 - \Delta\underset{\sim}{r}(\tau))$ at time $t-\tau$. Assuming uniform flux density for sodium atoms, we may write $P(\underset{\sim}{r}_1, t) = N$, N is the number density of sodium atoms. For isotropic diffusion, $P(\Delta\underset{\sim}{r}, \tau \,|\, \underset{\sim}{r}_1, t)$ is just the random walk probability density,[16]

$$P(\Delta\underset{\sim}{r}, \tau \,|\, \underset{\sim}{r}_1, t) = \frac{1}{4\pi D\tau}\, e^{-(\Delta x^2 + \Delta^2 y)/4D\tau} \quad . \tag{2.39}$$

Here we have restricted ourselves to two-dimensional motion. This is because the length of the photocathode is much longer than the

laser beam radius in our experimental set up. The characteristic time for diffusion, τ_D, in the z-direction is much longer than that in the x-y plane. When proper sample times are chosen, the z-dimension is effectively infinite and the motion of the atoms in the z-direction can be ignored.

To evaluate Eq. (2.38), we note that the integration over $\Delta z(\tau)$ gives a normalized value of 1; the integration over $z_1(t)$ gives the length L' of the detection region due to the detector aperture function $f_1(z/l)$ to be defined in Sec. 3.3. We can now separate $R(\tau)$ into two independent averages over x- and y-motion, because these do not correlate for random motion, i.e.,

$$R(\tau) = i_o'^2 R_x(\tau) R_y(\tau) L' , \tag{2.40}$$

where

$$R_x(\tau) = \frac{1}{\sqrt{4\pi D\tau}} \int_{-\infty}^{\infty} e^{-\Delta x_1^2(\tau)\left[\frac{1}{w^2}+\frac{1}{4D\tau}\right]} \int_{-\infty}^{\infty} e^{-\frac{4}{w^2}\left[x_1(t)-\frac{1}{2}x(\tau)\right]^2} dx_1(t) d\Delta x(\tau) . \tag{2.41}$$

The integration limits in $R_x(\tau)$ and $R_y(\tau)$ have been set to infinity because the dimension of the cell is much longer than the

Gaussian beam radius which defines the observation volume. In the time domain, this is equivalent to saying that the duration of the burst is much shorter than the total measurement time. Integrating Eq. (2.41) we get

$$R_x(\tau) = \frac{\sqrt{\pi}}{2} w \frac{1}{\left(1+\frac{4D\tau}{w^2}\right)^{\frac{1}{2}}} \tag{2.42}$$

and

$$R(\tau) = (i_o'^2/4)\, N(\pi w^2 L') \frac{1}{1+\frac{4D\tau}{w^2}}$$

$$= (i_o'^2/4)\,(NV)\frac{1}{1+\tau/\tau_D}\,, \tag{2.43}$$

where $V = \pi w^2 L'$ is the observation volume, and $\tau_D = w^2/4D$. τ_D is just the average time for an atom to diffuse a distance w in two-dimensions. NV is the total number of sodium atoms in the observation volume. In general, there is also stray light background present. Thus, the observed correlation function is fitted to

$$R(\tau) = A + B/(1+\tau/\tau_D)\,, \tag{2.44}$$

where A is a constant resulting from stray light contribution and

$$B = \frac{i_o'^2}{4}(NV)\,.$$

The profile of the focussed dye laser beam we used was usually not exactly Gaussian. It was actually elliptically shaped. For an elliptical Gaussian beam, the intensity profile is given by

$$I = I_o \exp\left(-\frac{2x^2}{w_x^2} - \frac{2y^2}{w_y^2}\right).$$

The two beam radii are not equal. The observed correlation function is then of the form,

$$R(\tau) = A + B/(1+\tau/\tau_{Dx})^{\frac{1}{2}}(1+\tau/\tau_{Dy})^{\frac{1}{2}}, \qquad (2.45)$$

instead of Eq. (2.44), where $\tau_{Dx} = w_x^2/4D$, $\tau_{Dy} = w_y^2/4D$, $B = \left(\frac{i_o'^2}{4}\right) N\pi w_x w_y L'$, and A is again a constant due to stray light. If w_x and w_y are known, a simple three-parameter fit (to A, B, D) allows us to determine the diffusion coefficient, D. We believe this is perhaps the most convenient and potentially most accurate technique for the evaluation of gaseous diffusion coefficients to date.

III. EXPERIMENTAL METHODS

3.1 General Description

A block diagram of the experimental set-up is shown in Fig. III-1. The light source was a Coherent Radiation CR 599 frequency-stabilized, single-mode dye laser, pumped by a CR-12 Argon ion laser. Typically, up to 40 mW of usable single-mode dye laser power were generated. Part of the dye laser beam was fed to a spectrum analyzer for monitoring the laser mode and frequency stability. For wavelength calibration a Kowalski type digital wave meter[17] was used which gives wavelength readings accurate to $\pm$ 0.01Å. Typically, we first tuned the dye laser to within 0.3Å of the sodium D_2 line using the wavemeter. Then we scanned the laser to the peak of the resonance by observing the visible fluorescence from a heated sodium reference cell.

With the help of two alignment mirrors, the dye laser beam was sent through the center of the flow cell located inside a blackened box. Various lens combinations were used to achieve the desirable beam diameters, ranging from 100 μm to 600 μm in the observation volume. These diameters were measured by recording the transmitted radiation through a 30 μm pinhole mounted on a micrometer-controlled x-y-z translation stage. In this manner, the beam

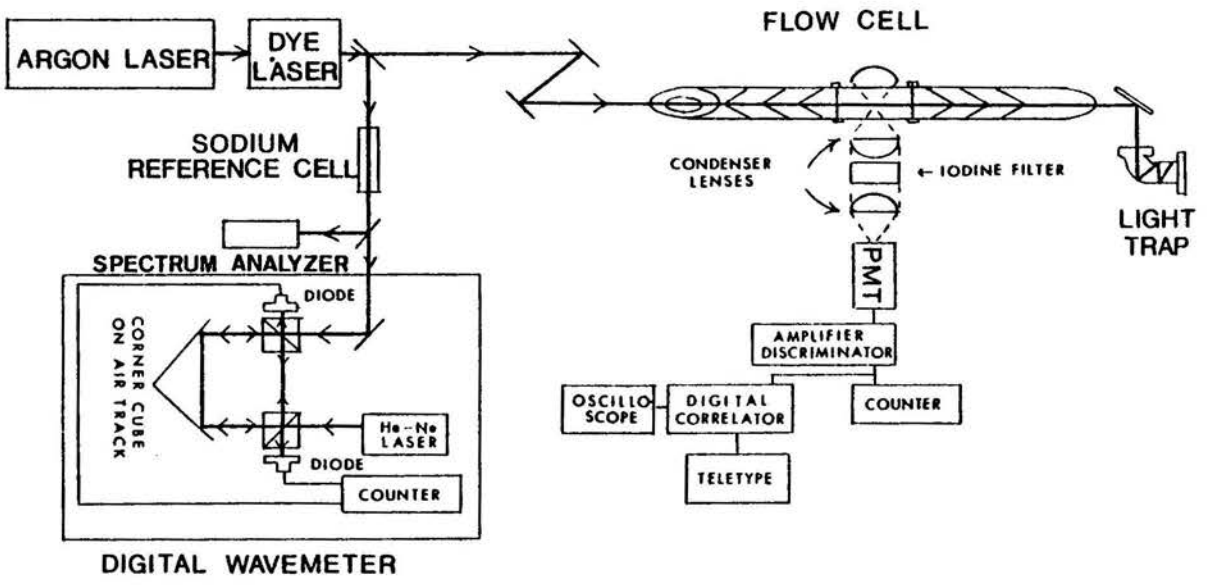

Fig. III-1 A block diagram of the experimental apparatus.

intensity profile in the x-y plane was traced out for several positions along the z-axis for each geometry used.

The fluorescence photons were collected at right angles to the beam by a pair of Klinger f/0.8 crown glass aspheric condenser lenses and a matching spherical mirror. The collected photons were then detected by a thermoelectrically cooled RCA 31034A photomultiplier. The output of the photomultiplier was amplified, discriminated, pulse shaped and then fed into a Malvern single-clipped digital correlator. A frequency counter was used for monitoring the average count rate going into the correlator. Experimentally obtained correlation functions were displayed on the oscilloscope screen and printed out when a permanent record was desired.

3.2 Flow Cell Design

At 5890Å, the resonant wavelength for sodium, one milliwatt of laser power contains 3×10^{15} photons/sec. When saturated, a sodium atom would emit $\sim 10^{7}$ photons/sec. It is necessary to suppress the stray light photons to less than 10^{-9} of the incident photons in order that the fluorescence signal will be larger than the stray light level. This is generally done by observation at right angles to the beam and by the use of a well designed scattering cell. In our experiments, two types of background scattering were present: (1) the "usual" stray light contribution due primarily to reflections

of the divergent part of the laser beam from cell walls and scattering from entrance and exit windows of the cell, and (2) Rayleigh scattering by the carrier gas atoms or molecules after the cell was filled with the flowing gas.

The first kind of background scattering can be overcome by proper design of the scattering cell. Several cells have been constructed and tested during the course of this research. With our first flow cell we found sodium oxide deposits on the cell wall and windows after some usage. As a result, stray light increased considerably. In order to be able to clean the cell wall, our final design was a detachable cell with three sections and removable windows. The general layout of this cell is shown in Fig. III-2. The two end sections, made of copper, were mounted with good quality quartz windows at Brewster's angle. A light trap was used to absorb the reflected laser light. There were three baffles in each end section made of brass. These baffles had sharp edges and were set at an angle of 30° with respect to the laser beam so that the spurious light scattered from the windows and any divergent light from the laser beam was prevented from reaching the observation region. The interiors of the end sections were first blackened with a coat of carbon film by using an acetylene torch. The two end windows were then epoxied on. We note here that ordinary flat black paint does not work for the interior of the cell, because sodium atoms would

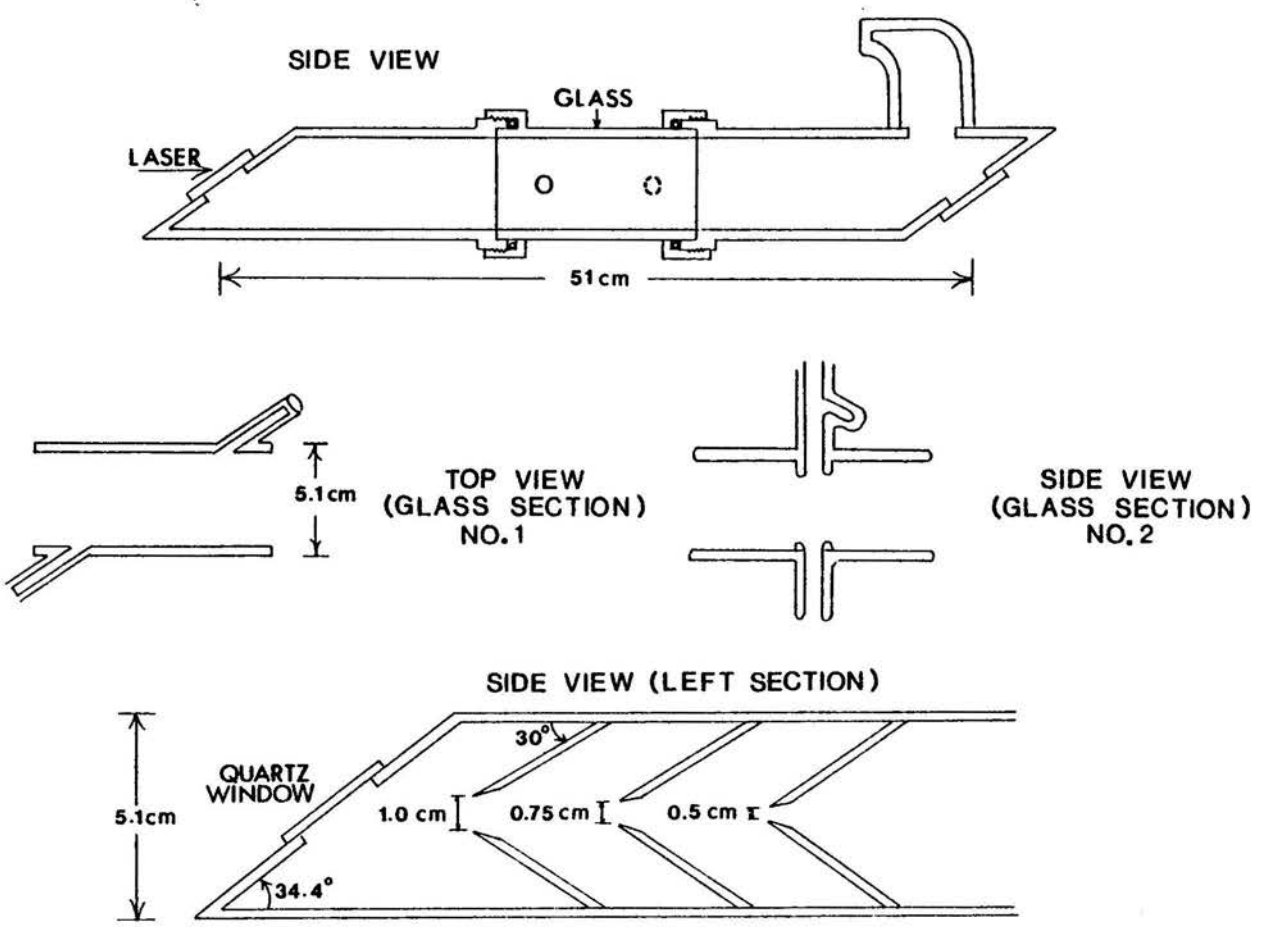

Fig. III-2. Layout of the flow cell with glass central sections no. 1 and no. 2.

chemically react with most oxides. The central section was made of a pyrex glass tube section with ports connected to the flowing gas tank and vacuum system. Our initial experiments were performed with tube section no. 1 as shown in Fig. III-2. Its inlet and exit tubes were at an angle of 37° with the tube section. Later on we used tube section no. 2, in which the inlet and exit tubes were perpendicular to the main tube section. The interior of the glass sections except for the observation windows were also blackened as described above. The observation windows were then cleaned carefully. The three sections were joined together by ultra-torr type fittings so that the whole cell was vacuum tight. The exterior of the entire cell except for the windows was also blackened by using ordinary flat black paint. With this cell, the stray light of this type was reduced so that only about 2×10^{-11} per steradian of the incident photons reached the photocathode.

By heating up a side pocket containing metallic sodium on the inlet tube of the central section, sodium atoms were seeded into the flowing gas. The pressure of the gas maintained in the cell and the pressure drop across the observation region were monitored by a mercury manometer incorporated in the gas handling system with measurement stations located near both the inlet and exit tubes of the glass section.

We have chosen helium as the buffer gas because helium atoms have the smallest Rayleigh scattering cross-section in the visible region of all atoms and molecules.[18] Rayleigh scattering by helium atoms at 200 Torr of pressure, yields 3×10^{-11} scattered photon per steradian per incident photon. In principle, to reduce Rayleigh scattering, one only need rotate the polarization of the laser parallel to the direction of observation. Electromagnetic theory then predicts that no Rayleigh scattering would be observed because electromagnetic radiation must have a transverse component to the direction of propagation. However, since we are collecting light over a cone of angles, some Rayleigh scattering will be detected. We found that Rayleigh scattering decreased by a factor of two only as we changed the laser polarization from perpendicular to parallel to the observation direction. We also found that the sodium fluorescence intensity dropped by a factor of two when the incident laser was polarized parallel instead of perpendicular to the direction of observation. As a result, there is a net loss in signal to noise when parallel polarization is used. Another approach we tried involves inserting a polarizer with polarization perpendicular to that of the laser between the cell and the collecting lenses. Again, there is no net gain in signal to noise.

3.3 Total Detection Efficiency

The total detection efficiency is defined as the product of the optical collection efficiency, ϵ, and the photon counting efficiency η. The meaning of these efficiencies and our experimental measurements of these quantities are discussed in this section.

The optical collection efficiency is the fraction of light emitted from the focal volume that is collected by the optical system used. It is determined as follows. From solid angle calculations, a lens with a focal length of $f = 4$ cm, and clear aperture diameter of $\phi = 4.7$ cm, should collect 6.4% of the light. The matching spherical mirror should collect an equal amount of light emitted in the opposite direction. Unfortunately, some of the light is lost due to lens aberrations and reflection losses. These factors are difficult to calculate reliably, so we measured them directly. A schematic of the experimental set up for this measurement is shown in Fig. III-3. The two lenses were set up in their position for single atom experiments. A helium discharge of diameter 0.2 cm covered with black tape except for a volume 0.5 cm in length was used to simulate a line source. The discharge was placed at the focus of the first lens. The second lens then focussed the light on the rectangular shaped photocathode. The transmitted power was first measured at the center of the front face of the first lens through a 4 mm diameter aperture. This allows us to determine the intensity I_L^o at that joint. The

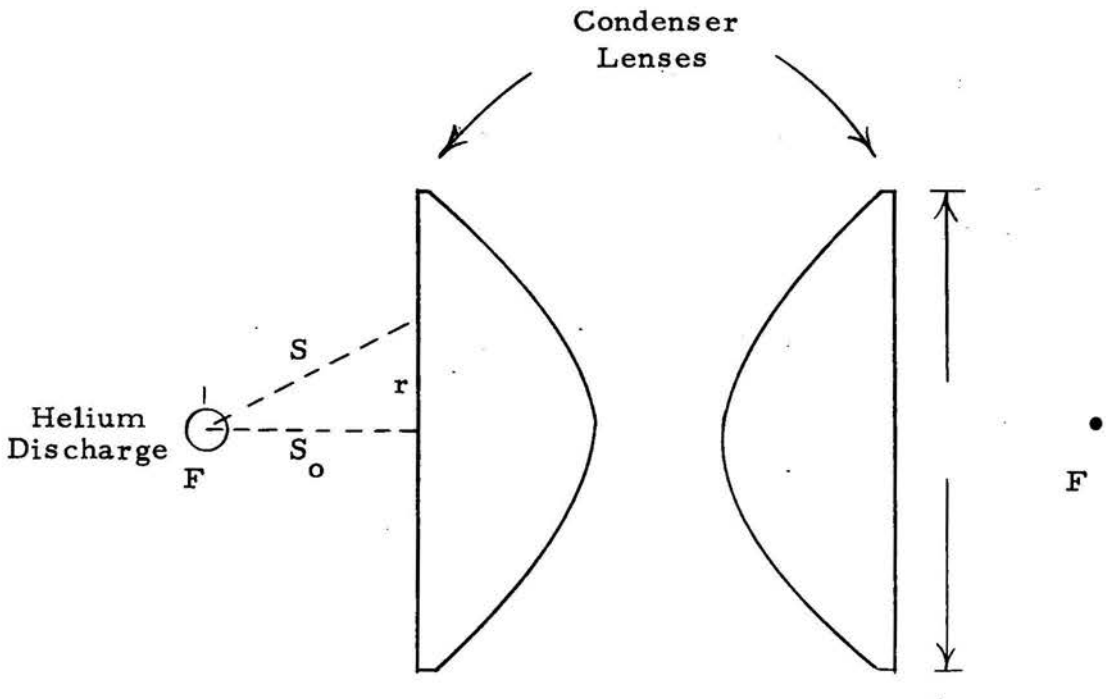

Fig. III-3. Set up for measurement of the transmission of the lens system. F's indicate foci of the two lenses.

intensity, $I_L(r)$, at a point r from the center of front face of the first lens is

$$I_L(r) = I_L^o \cdot \left(\frac{S_o}{\sqrt{S_o^2 + r^2}} \right)^2 \tag{3.1}$$

where S_o is the distance from the line source to the flat face of the lens. Note that for aspheric lenses, S_o is not equal to the focal length f. Integrating (3.1) over the lens surface, we find that the power incident on the first lens is

$$P_i = \pi S_o^2 I_L^o \ln \left(\frac{\phi^2}{4S_o^2} + 1 \right) \tag{3.2}$$

Next, the transmitted power at the focus of the second lens, P_f, was measured. The transmission of the lens system is just P_f/P_i. Using this technique, we found that the transmission of the lens pair is $35 \pm 2\%$. When half of a pyrex glass tube section identical to the glass section used in the cell was inserted between the aperture and the first lens, the transmission was reduced to $30 \pm 2\%$. Because the light collected by the mirror needs to go through both sides of the glass tube, the transmission of light collected by the mirror was estimated to be $22 \pm 2\%$. The optical collection efficiency of the lens-mirror system, ϵ, is then $(0.3 + 0.22) \times 6.4\%$, or 3.3%. This number represents a reasonable estimate for use in the calculation

of total detection efficiency. In retrospect, however, we should have simulated a point light source instead of the line source used here. Later in the measurement of the effective length of the photocathode, a simulated point light source was indeed used to eliminate possible errors due to less than perfect focussing along the length of the observation region.

The photon counting efficiency of the detector is defined as the ratio of detected photoelectron count rate to the rate of incident photons, i.e.

$$\eta \text{ (photon counting efficiency)} = \frac{\text{(count rate detected)}}{\text{(\# of incident photons/sec)}} = \frac{R}{(P/h\nu_o)} \qquad (3.3)$$

where P is the light power or incident on the photomultiplier and ν_o its frequency.

The photon counting technique has been widely used. In some applications, it is desirable to maximize the ratio of signal counts to dark counts. For single-atom velocity measurements, however, it is desirable to have the highest possible photon counting efficiency, i.e. signal level. Dark counts are insignificant with the background level we have. In the following, the procedure used to set up photon counting electronics is described. For more details on the theory

and practice of photon counting, the work of Poultney[19] and references therein should be consulted.

First, the proper voltage applied to the photocathode and discriminator level was set. The dye laser was tuned to 5890Å and sent directly onto the photocathode. The laser power was attenuated by a stack of calibrated N.D. filters to about 10^{-13} w. This was done to avoid saturating the photocathode. With the discriminator set at a fixed level, the detected count rate was measured for various high voltages applied to the photocathode. This is shown in Fig. III-4 for discriminator set at 90 mv. The optimum voltage should be set on the so-called photon counting plateau, where changes in high voltage produce little or no changes in the detected count rate. In the single-atom experiments, we set high voltages at either 1500 volts or 1800 volts. Next, the photomultiplier was set at the appropriate voltage (either 1500 v or 1800 v) and the count rate was measured as a function of discriminator level or pulse height. This produced the so-called integral pulse height spectrum. Calculating the number of pulses within a certain pulse height band by subtracting, we then obtained the differential pulse height spectrum.

Figs. III-5 and III-6 show the integral and differential pulse height spectrum of our RCA 31034A photomultiplier tube operating at 1500 and 1800 volts respectively. They both exhibit single-photoelectron peaks. The optimum discriminator level should be

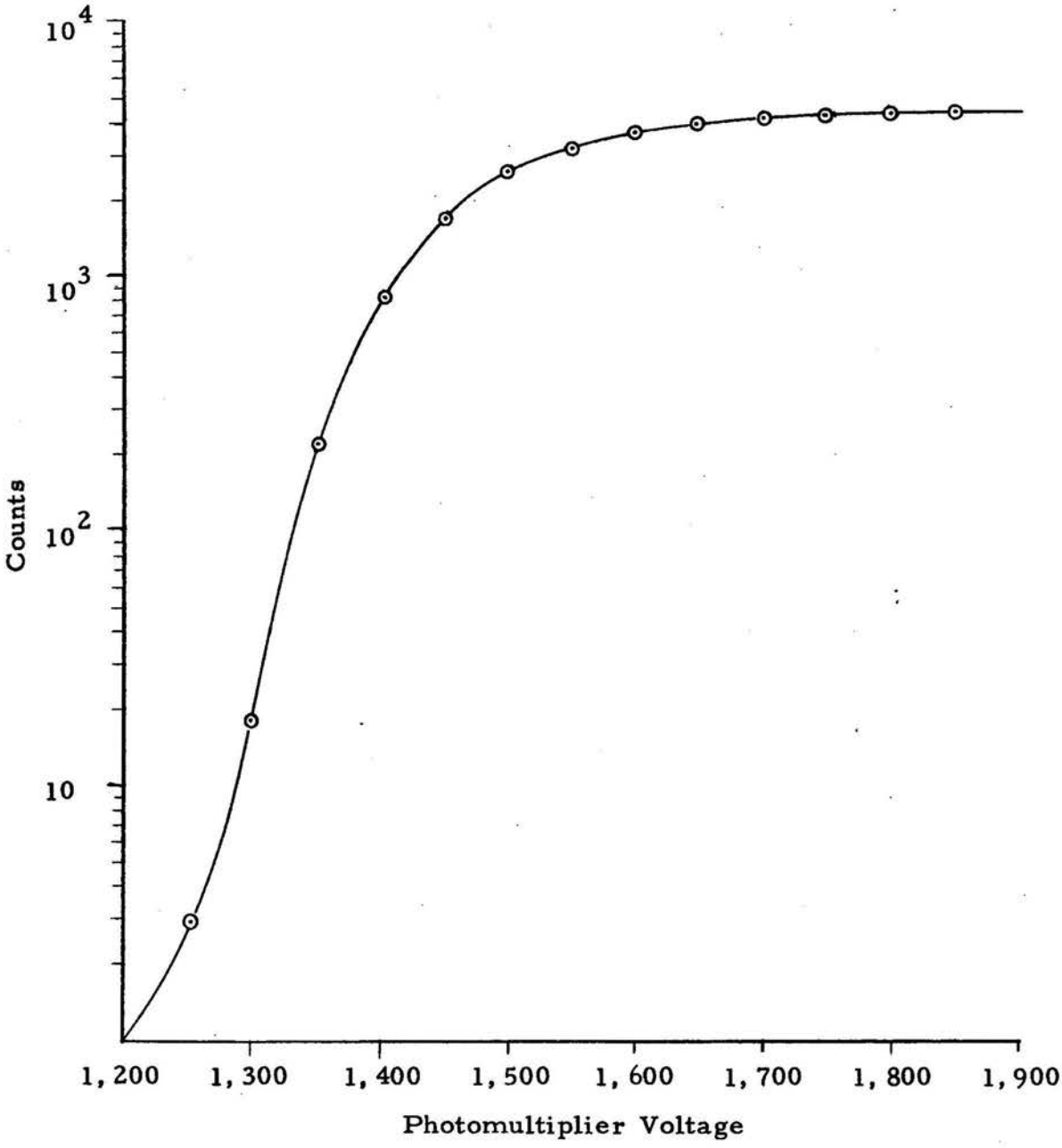

Fig. III-4. Count rate detected is plotted as a function of high voltages applied to the photocathode of our RCA 31034A photomultiplier.

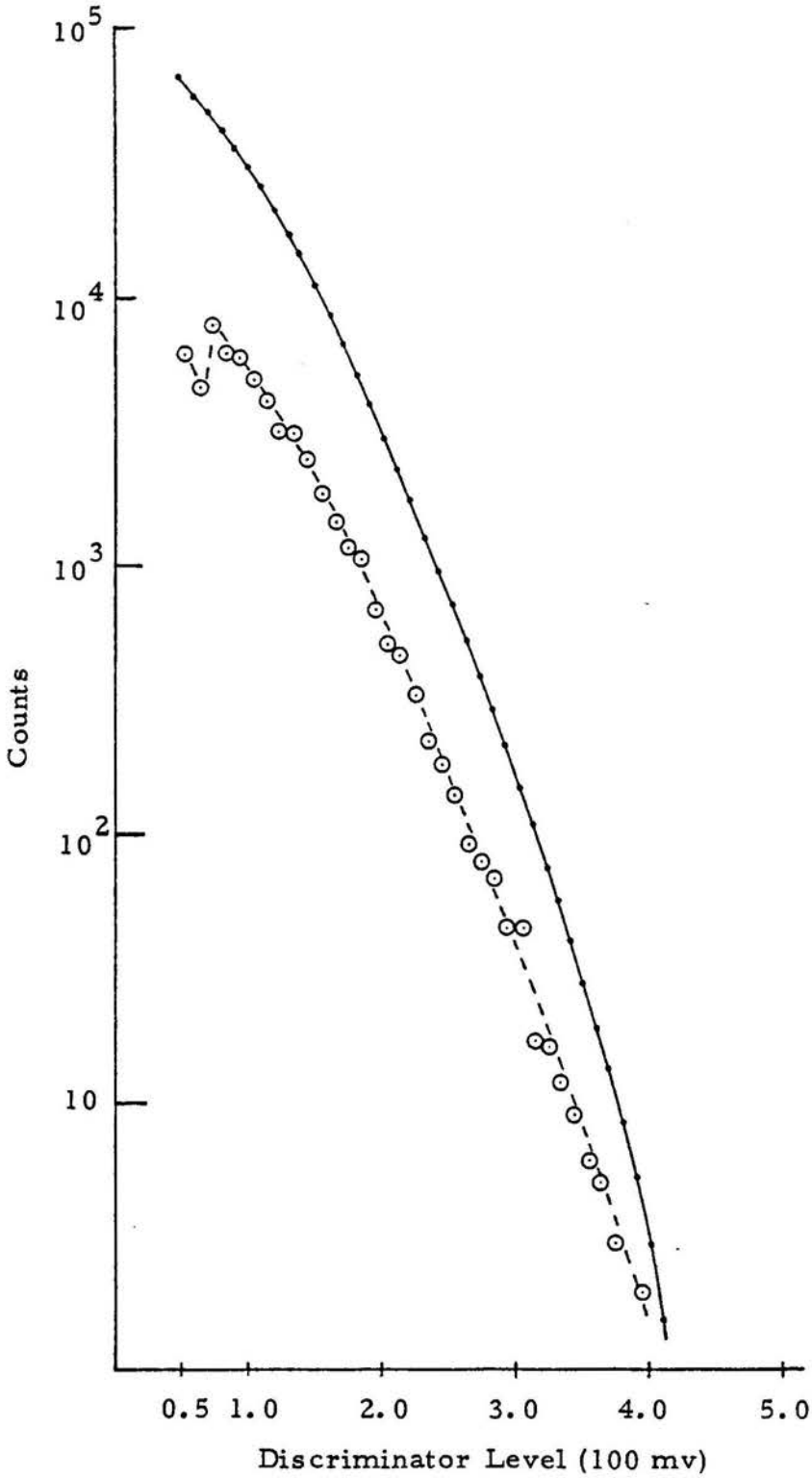

Fig. III-5. Integral and differential pulse height spectrum of our RCA 31034A photomultiplier taken at 1500 V.

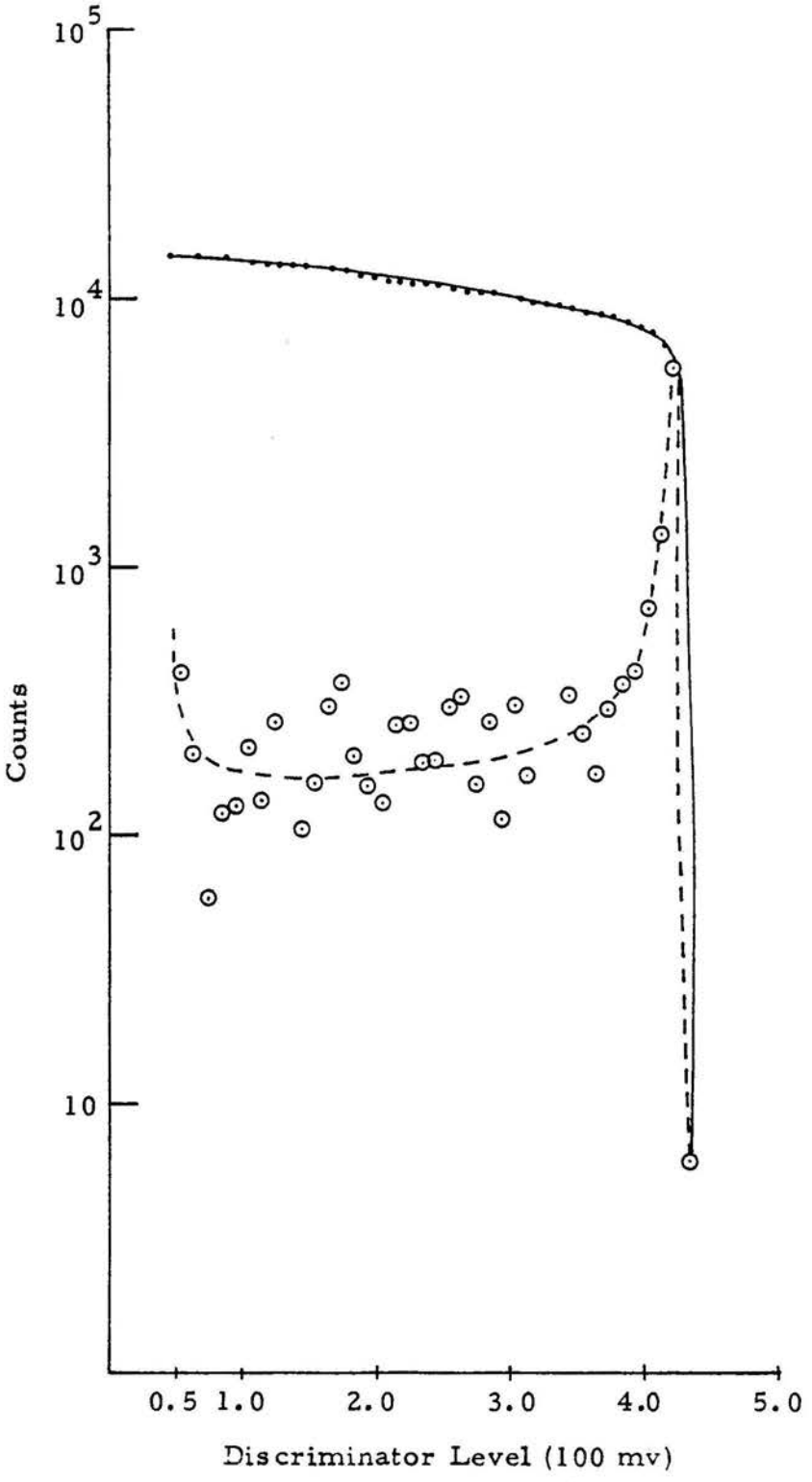

Fig. III-6. Integral and differential pulse height spectrum of our RCA 31034A photomultiplier taken at 1800 V.

set at a pulse height on the ascending edge of the peak to admit the single photoelectrons while rejecting the small pulses that consist of most of the dark counts of the photomultiplier and amplifier noise. This level was set at 90 mV for both voltages used. Examining Fig. III-6, however, one finds that the single-photoelectron peak is very narrow. In retrospect, we should have set the discriminator level much higher, around 350 mV. Still, all the single-photoelectrons are counted with the lower discriminator level we used.

To obtain the photon counting efficiency at a given voltage and discriminator level, we first measured the laser power, P_o, before attenuation by a power meter. The incident laser power at the photocathode, P, is just this number multiplied by the attenuation factors of the calibrated neutral density filters. Substituting this number and the observed count rate, R, into Eq. (3.3), η can now be evaluated. For our RCA 31034A photomultiplier, these measurements yielded the photon counting efficiency, η, equal to 15% at an applied voltage of 1500 volts, and 29% at 1800 volts. For both applied voltages, the discriminator level was set at 90 mv.

Combining the results of optical collection efficiency and photon counting efficiency measurements, we found the total detection efficiency, $\epsilon\eta$, of our system to be 0.5% at an applied voltage of 1500 volts and 0.96% at 1800 volts. Two other methods can be

used to check the total detection efficiency independently; they are the measurements of fluorescence in an evacuated sodium cell and Rayleigh scattering from the flow cell.

In the fluorescence method, the power absorbed by the fluorescent atoms, P_A, is related to the incident power, P_o, and transmitted power, P_T, as:

$$P_A/P_o = 1 - P_T/P_o = 1 - \exp(-\sigma NL)$$

$$\cong \sigma NL \qquad (3.4)$$

where $\sigma = 8 \times 10^{-12}$ cm^2 [5] is the absorption cross-section for the sodium D_2 line, and N is the number density of sodium. At room temperature $N = 9 \times 10^5/\text{cm}^3$. [5] L is the effective length of the focal volume as seen by the photomultiplier. It was determined by a method similar to that described earlier for lens transmission measurement. The light source was a pinhole placed before the He discharge with a ground glass plate in between to ensure light coming out of the pinhole in all directions. This assembly was translated horizontally by a distance z with respect to the lens axis, and the output current was recorded as a function of the position of z, the effective point source. In this manner, we obtained the detector aperture function $f_1\left(\frac{z}{L_p}\right)$, as shown in Fig. III-7. The variable z is the distance of the pinhole from the center of the observation

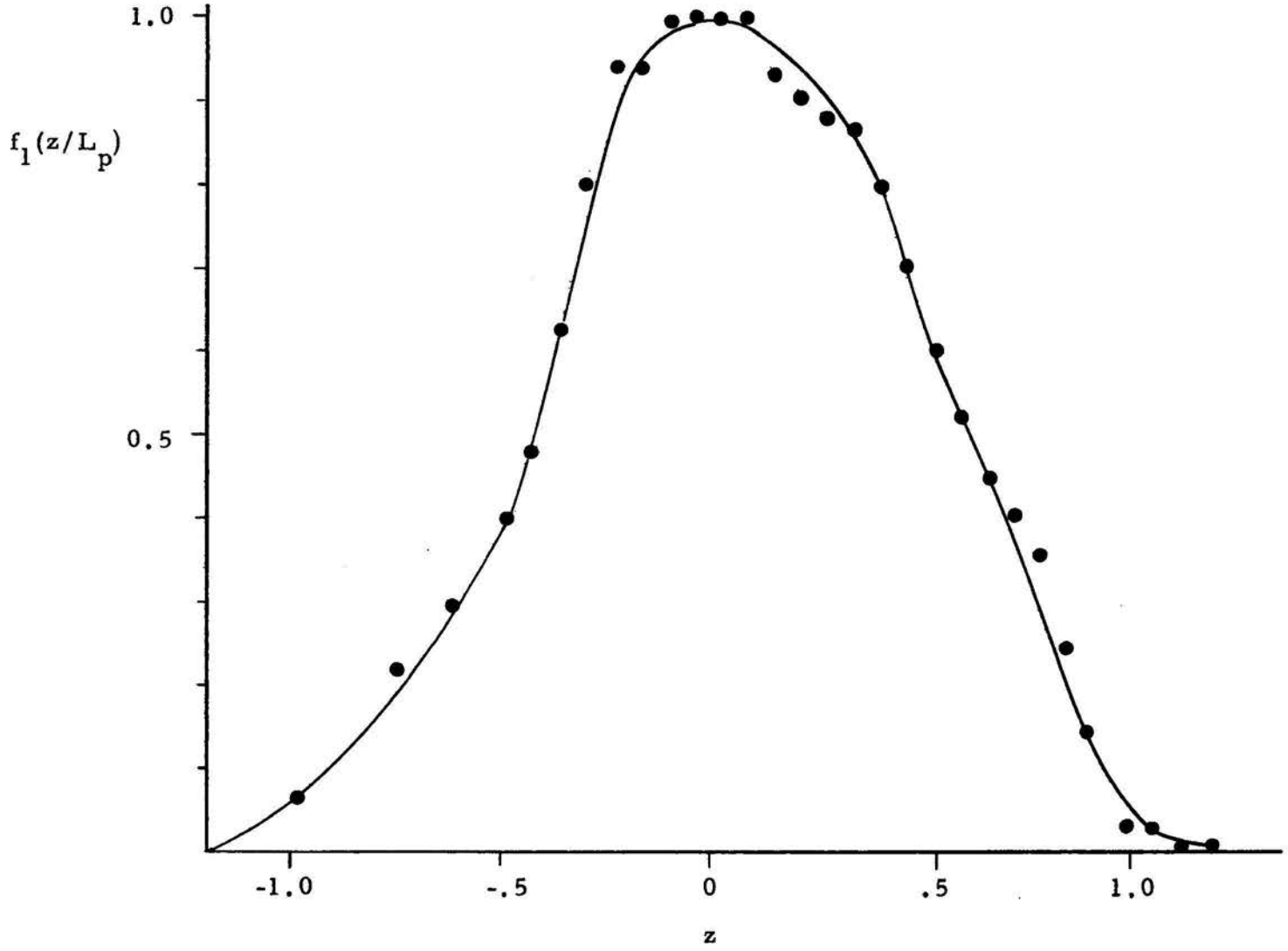

Fig. III-7. The detector aperture function $f_1(z/L_p)$ as a function of the distance of the pinhole from the center of the observation region, z.

region, and L_p is the photocathode length. Integrating the area of the curve and dividing by the peak current, we found that the effective length of the observation region was $L = 1.12$ cm, as compared to the length of the photocathode, $L_p = 1$ cm.

Since resonance fluorescence is isotropic, the fluorescence count rate, R_F, should just be the scattered power (equal to the absorbed power, P_A) multiplied by the detection efficiency, $\epsilon\eta$, and divided by the photon energy $h\nu_o$:

$$R_F = (P_o \sigma NL)(\epsilon\eta)/h\nu_o \tag{3.5}$$

R_F was obtained by taking the difference in the total count rate for laser wavelength on and off-resonance with corrections for power variations. Because stray light is roughly independent of the wavelength, its contribution cancels when the subtraction was done. Since $I_s = 16$ mw/cm^2 for sodium atoms in vacuum, care must be taken to prevent saturating the transition. Typically, a couple of μw was used for mm size laser beam.

This can be written as,

$$\epsilon\eta = \frac{R_F h\nu_o}{\sigma NL\, P_o} \tag{3.6}$$

This expression also holds for Rayleigh scattering if R_F in Eq. (3.6) is replaced by R_R, the count rate due to Rayleigh scattering,

which is just the difference in count rates with and without helium gas in the cell with correction for power variations. $\sigma = 3.72 \times 10^{-29}$ cm^2, the total Rayleigh scattering cross-section for He,[19] and N, the number density of He at a given pressure and temperature, are used. At 200 Torr and 300 K, $N = 6.44 \times 10^{18}$ atoms/cm^3.

Measurements by both techniques yield total detection efficiencies ranging from .4% to .6% when the photomultiplier was at 1500 V, in good agreement with our previous estimation. There seemed to be some variation from day to day in the numbers we obtained. Presumably, this was due to minor misalignment of the collection optics with respect to the laser beam.

3.4 The Iodine Vapor Cell as an Optical Filter

In an effort to further reduce stray light, an iodine vapor cell was inserted between the two condensor lenses in some of the single-atom detection and velocity measurements to be discussed in Chapter IV. A similar technique was used by previous workers to suppress background scattering at the laser frequency while passing the frequency shifted Raman and Brillouin scattered light.[20] This was done for the 5145Å line of an Argon ion laser. The iodine vapor cell may be used as an optical filter for our experiment because I_2 also has an absorption line which nearly coincides with the sodium D_2 line, as shown in Fig. III-8. If the dye laser is tuned to this line, the stray light at laser frequency should be strongly absorbed

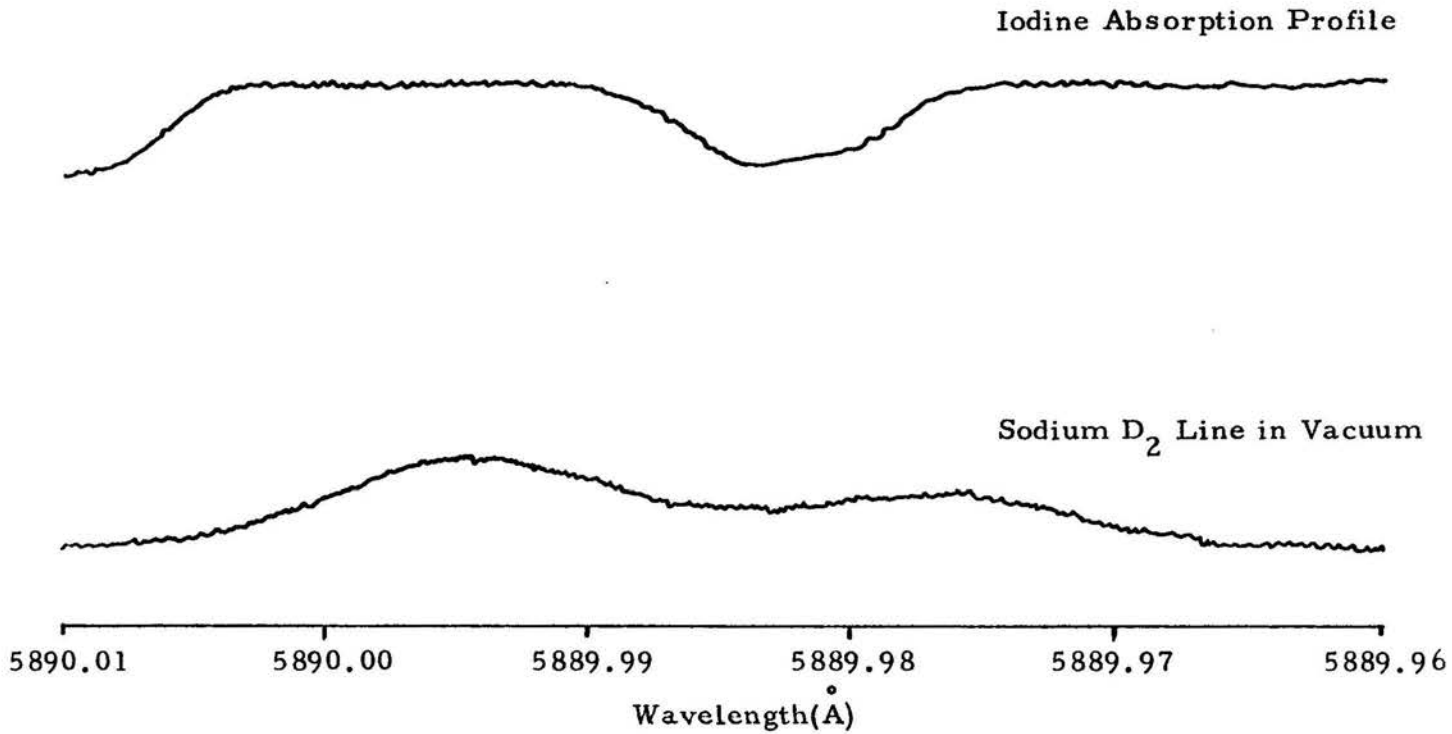

Fig. III-8. The iodine absorption lines in the vicinity of sodium D_2 line.

by iodine molecules; the pressure-broadened Na resonance line which is broader than the I_2 absorption line, is attenuated to a much lesser extent. Unfortunately, the spectrum of Rayleigh scattering (by helium atoms) which is Doppler broadened is also quite broad. At 200 Torr of helium and 300°K, the Doppler width of Rayleigh scattered light and the pressure broadened width of sodium emission are respectively, 2.22 and 4.2 GHz. As a result, background light due to Rayleigh scattering cannot be blocked effectively. Only the stray light scattered off cell walk and windows can be effectively attenuated by the iodine cell.

The iodine cell we used was made of a 1-inch long pyrex tubing of 3-inch diameter. The ends of the section were sealed off with pyrex windows. Several hundred milligrams of solid iodine were placed in the cell. The cell was evacuated for about 10 minutes through a nitrogen cold trap by using a roughing pump and then sealed off. .A layer of blackened aluminum sheet about $1\frac{1}{2}$-inches wide was wrapped around the cell side wall. The edges of the cell face were also blacked with flat black paint to prevent leakage of light around and through the glass sidewalls. Heater tape was wrapped around the sides of the cell to heat it. The cell temperature was measured with a thermocouple installed at the tip of the cell where the remaining solid I_2 is concentrated.

The attenuation factor for stray light at the laser frequency was measured by recording the transmitted stray light power with and without the iodine filter. From Eq. (3.4), which applies to this case also, we can see that the ratio of transmitted to incident power should be equal to $\exp(-\sigma_o NL_c)$, where σ_o is the peak absorption cross-section of I_2, N is number density of I_2, and L_c the length of the iodine cell. Since $N = p/kT$, and σ_o is proportional to $T^{-\frac{1}{2}}$ to the first order, due to its dependence on the Doppler linewidth, one expects that the natural logarithm of the attenuation factor would be proportional to $p/T^{3/2}$. The above arguments are valid for background scattering due to stray light alone. Because Rayleigh scattering due to 200 Torr of helium and sodium D_2 line fluorescence are Doppler-broadened and pressure-broadened respectively, the attenuation of scattered light of these two types should be the convolution of the scattered light with $\exp(-\sigma(\nu)NL_c)$. Thus, we do not necessarily expect a $p/T^{3/2}$ dependence. The attenuation for stray light alone, for stray light plus Rayleigh scattering due to 200 Torr of helium buffer gas, and for sodium resonance signal are all plotted versus $p/T^{3/2}$ for comparison in Fig. III-9. The vapor pressure of I_2 was calculated from the empirical formula given in ref. 21,

$$\log p_{mm} = 10.167 - 3178.0/T \qquad (3.7)$$

Fig. III-9. The attenuation factor for stray light, for stray plus Rayleigh scattering due to 200 Torr of helium buffer gas, and for sodium resonance fluorescence by the iodine filter are plotted as a function of $p/T^{3/2}$.

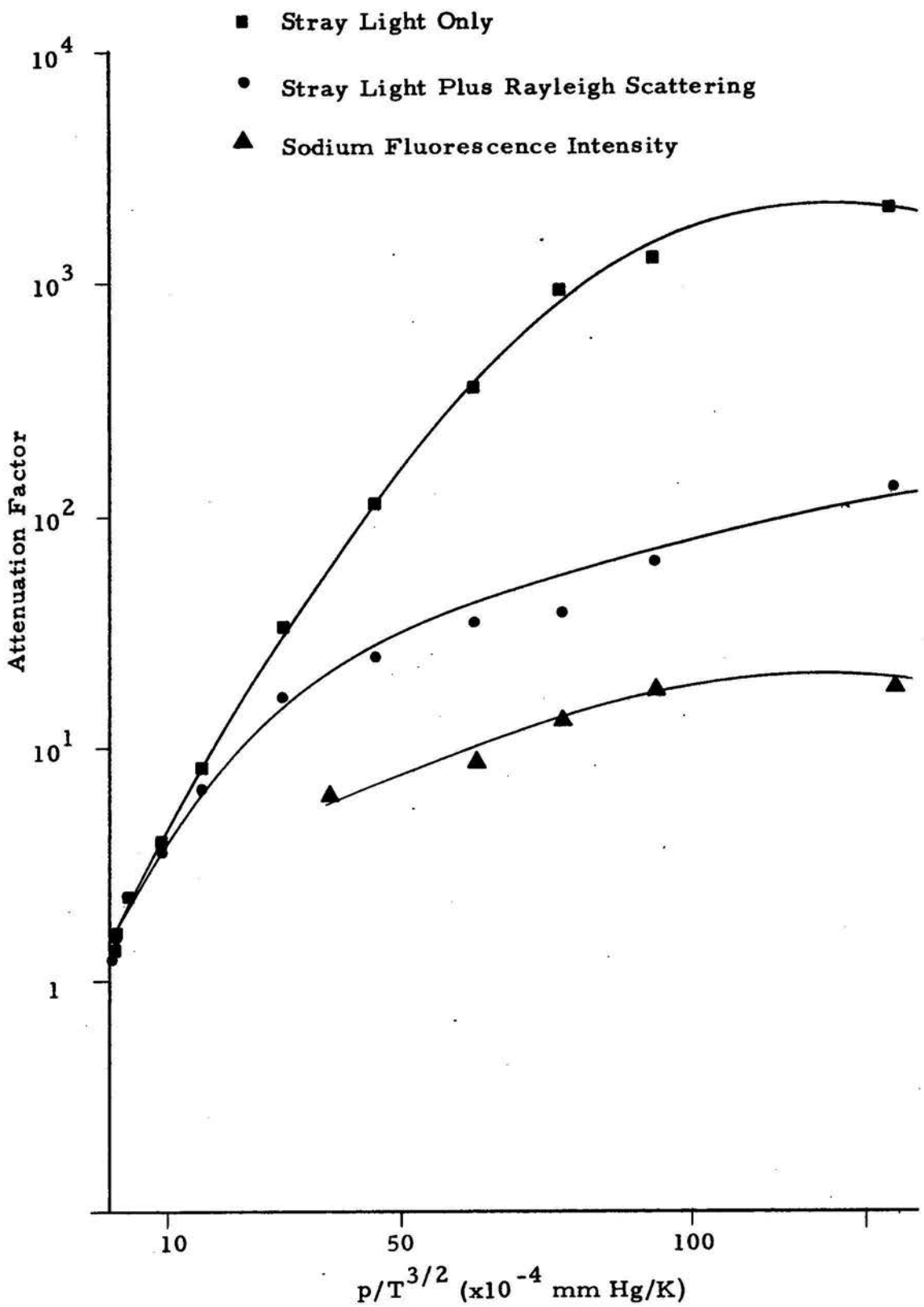
Stray Light Only
Stray Light Plus Rayleigh Scattering
Sodium Fluorescence Intensity
Attenuation Factor
10^4
10^3
10^2
10^1
1
10
50
100
$p/T^{3/2}$ (x10^{-4} mm Hg/K)

where p_{mm} is the vapor pressure of I_2 in mm Hg, and T is the temperature in K. Eq. (3.7) was obtained for temperatures ranging from 39-166°C. It was assumed to be valid for data taken between room temperature and 39°C. The curve for stray light attenuation obtained deviates from the straight line expected. Similar behavior was found by Devlin et al.[20] in their studies. They surmised that this could be due to collisional broadening of I_2. For the results we presented in Fig. III-8, the use of Eq. (3.7) for the vapor pressure of I_2 at temperature below 37°C could contribute significantly to the error.

In our single-atom velocity and transit time measurements, the iodine cell was operated at a temperature such that the total background attenuation factor (stray light plus Rayleigh scattering) was about 100. The corresponding signal attenuation as read from Fig. III-9 was about 18. Although the iodine cell permits the use of higher laser power, the gain in signal-to-noise is not enough to offset the loss in signal counts from a single atom, which was already marginal. Hence, this technique did not help very much for the single-shot type experiments we performed. For experiments in which a time-average is done, this could still be a useful technique.

3.5 Signal Processing

When taking correlation functions, we used the Malvern single-clipped digital correlator. Its principles, applications, and

limitations have been given in Refs. 10 and 11. One of the major merits of this instrument is that it processes the detected photo-pulses digitally and directly in real time. Fig. III-10 illustrates how a two-humped correlation function is obtained for a two-beam time-of-flight velocity measurement on this instrument. The input pulse train is first fed into a shift register through a set-reset flip-flop, which places a "1" in the shift register only when more than k counts arrive in a sample time ΔT. The clipping level, k, may be set at will. This clipped signal is moved sequentially down the shift register by the sample time clock. Thus, at time $q\Delta T$, q being an integer, the contents of the mth shift register contains $C_k(q\Delta T - m\Delta T)$, the clipped delayed version of the unclipped input counts per sample, $C(q\Delta T)$. Both $C(q\Delta T)$ and $C_k(q\Delta T - m\Delta T)$ are defined in Sec. 2.2. The quantity $m\Delta T$ is the delay time. The input $C(q\Delta T)$ is applied to each "and" gate, and the resulting product $C(q\Delta T)\, C_k(q\Delta T - m\Delta T)$ is added to the mth memory channels. Repeating this process for N_T samples, we obtain the single-clipped correlation coefficient $R_k(m\Delta T)$ for delays from ΔT to $M\Delta T$, M being the total number of channels available. Mathematically, this can be written as:

$$R_k(m\Delta T) = \sum_{q=1}^{N_T} C(q\Delta T)\, C_k(q\Delta T - m\Delta T), \quad 1 \leq m < M \ , \qquad (3.8)$$

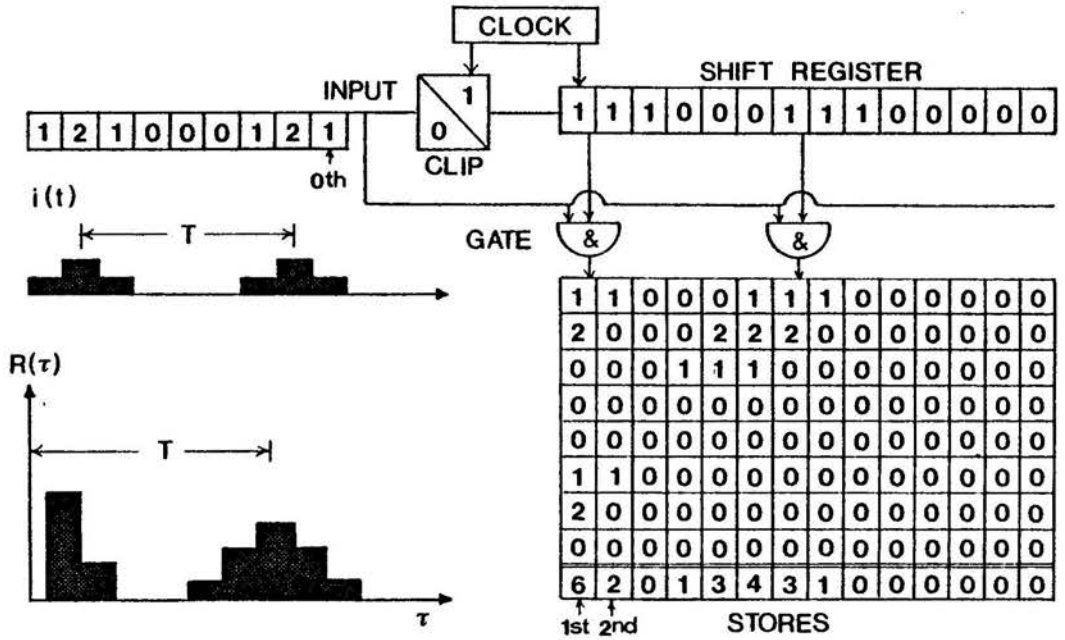

Fig. III-10. The operation of the Malvern single-clipped digital correlator, illustrating the manner in which a two-humped correlation function is obtained for a two beam time-of-flight velocity measurement.

where N_T is the total number of samples. This is the same function as was discussed in section 2.2. Fig. III-10 clearly shows that the time-of-flight between the two input pulses is retrieved from the corresponding correlation function, even though the shapes of the pulses are somewhat distorted primarily because there are only four counts per burst to start with.

Utilizing the clipping feature, one can in principle clip out most of the background noise if the signal level is high enough. This was done in remote wind speed measurements performed at Colorado State University.[12, 13] The clipping level was set as high as six times the noise level. Very little or no noise counts were registered under those conditions. Whenever a large enough dust particle with signal counts per sample higher than the clipping level passed through the laser beams, a good quality correlation function was obtained. It was found that as few as 10 signal counts above clipping was sufficient for detecting a reasonable correlation function. In the present experiment, however, the maximum number of signal counts per atom per transit is fixed, i.e. there are no "larger" atoms. Our signal level, limited by the detection efficiency, only allows us to clip at most 1.5 to 2 times above the average background counts per sample level. Because of the statistical nature of the detection process, the background counts will fairly often exceed clipping level and deteriorate the quality of the observed correlation function. Thus,

the clipping feature may provide some signal-to-noise improvement if properly set, but it cannot eliminate the background noise completely.

Another feature of the Malvern correlator worth noting is the probability density mode of operation. In this mode, the number of samples containing C counts is stored in the (C + 1)th memory channel. If N_T samples have been taken, the (C + 1)th channel in the probability density mode will display

$$G(C, \Delta T) = N_T P(C, \Delta T) \tag{3.9}$$

where $P(C, \Delta T)$ is the probability density of detecting C counts in a sample time, ΔT. This feature allowed previous workers to successfully determine the dust particle size distribution in the atmosphere and to evaluate the performance of the laser velocimeter for wind speed measurements.[22] We used this technique to estimate the average number of counts in a fluorescence burst emitted by a single atom. Measurements of this type are discussed in Chapter IV.

3.6 Experimental Procedures

The first step is alignment of the optical system. With the flow cell removed from the box, the laser beam was sent through the focus of the first condenser lens. The flow cell was then put back in place and adjusted vertically and horizontally until the transmitted

laser power at the exit window of the cell was at its maximum. This usually assured that the laser beam went through the center of the cell. Sometimes additional minor adjustments of the position of the cell were necessary to minimize stray light. Next, the Rayleigh scattering level was measured, and the detection efficiency was determined from Eq. (3.6). If this turned out to be lower than expected, the evacuated sodium cell was used to recheck and optimize the position of the condenser lens and mirror. Finally, we started heating the sodium side pocket on the flow cell until the proper sodium level was reached as determined by monitoring the fluorescence count rate, R_F .

We measured the fluorescence count rate, R_F, by taking the difference in count rate on and off resonance with corrections for power variations. Theoretically, R_F is calculated by integrating the contributions due to the atoms from each element of the area $\Delta b \Delta z$ in the plane defined by the laser beam and axis of the collection optics. If the average velocity of the atoms is v, there would be $Nv\,(\Delta b)(\Delta z)$ atoms crossing the area element $\Delta b \Delta z$ per second, each emitting $\epsilon\,\eta\,F_b\,(b/w)\;f_1\,(z/L_p)$ or $\epsilon\,\eta\;F\;f_2\,(b/w)\;f_1\,(z/L_p)$ counts. That is,

$$R_F = \sum_{b/w=0}^{\infty} \sum_{z=-\infty}^{\infty} \epsilon\eta F\; f_2\,(b/w)\; f_1\,(z/L_p)\; Nv\Delta b\Delta z \;, \qquad (3.10)$$

where N is the number density of sodium atoms, f_2 (b/w) and f_1 (z/L_p) are dimensionless functions plotted in Fig. II-2 and Fig. III-7 respectively. If the limits of b/w are taken from 0 to 2, and z/L_p from -1.2 to 1.2, then essentially all the contributions of f_1 (z/L_p) and f_2 (b/w) are included. Eq. (3.10) can now be re-written as,

$$R_F = (wL_p)(Nv)(\epsilon\eta F) \sum_{b/w=0}^{2} \sum_{z/L_p=-1.2}^{1.2} f_2(b/w)\, f_1(z/L_p)\, (\Delta z/L_p)\, (\Delta b/w) \qquad (3.11)$$

With L_p = 1 cm, numerical integration yielded,

$$\sum_{b/w=0}^{2} f_2 (b/w)\, (\Delta b/w) = 0.77$$

and

$$\sum_{z/L_p=-1.2}^{1.2} f_1 (z/1)\, (\Delta z/1) = 1.12 \ .$$

Hence, the incident flux of sodium atoms, Nv, in atoms per cm^2 per sec, is equal to,

$$Nv = \frac{R_F}{(1.12)\,(0.77)\,(\epsilon\eta F)\,w\,(1\text{ cm})} \quad . \tag{3.12}$$

The number of sodium atoms per sec entering the rectangular observation area defined by the Full-Width-at-Half-Maximum of the detector aperture function $f_1(z/L_p)$, $L' = 1.2$ cm, and the laser beam diameter, $2w$, is

$$Nv\,(2w)\,(L') = 2.78\,\frac{R_F}{\epsilon\eta F} \quad . \tag{3.13}$$

Two other quantities are of interest: the sodium atom concentration, N, and the number of sodium atoms in the focal volume defined by $\pi w^2 L'$, N'. They are

$$N = \frac{R_F}{0.86\,\epsilon\eta F}\left(\frac{1}{wv}\right) \tag{3.14}$$

and

$$N' = N\,(\pi w^2 L')$$

$$= (4.37)\,(w/v)\,\frac{R_F}{\epsilon\eta F} \quad . \tag{3.15}$$

To ensure that we indeed detected individual sodium atoms, the following procedure was adopted. The correlator was activated for a measurement period of length, $N_T \Delta T$, where ΔT is the sample time, and N_T is the number of samples taken in an

experiment. Typically, $N_T = 100$ samples were taken. The sodium density was set so that on the average, only a fraction of a sodium atom enters the laser beam during the measurement time, $N_T \Delta T$. This sodium level for the experiment was obtained by multiplying Eq. (3.13) by $N_T \Delta T$, the measurement time, i.e.

$$\left(\begin{array}{l}\text{\# of sodium atoms} \\ \text{entering the laser} \\ \text{beam during the} \\ \text{measurement time}\end{array}\right) = 2.78 \left(\frac{R_F}{\epsilon \eta F}\right) N_T (\Delta T) \qquad (3.16)$$

Once the proper level of sodium atoms was reached, we repeated starting and resetting the correlator while monitoring the oscilloscope screen for correlation functions. For many tries, no correlation functions were observed. This is because either no sodium atoms were present or perhaps because the diffusing atoms did not stay long enough in the beam to give a burst visibly above the noise or else they went through the side of the beam. Whenever a sodium atom produced a burst of fluorescence photons sufficiently above the background during its transit, a visible correlation function was obtained. Typically, sample times ranging from 10 to 40 μs were used. For $N_T = 100$ samples, the total measurement time was from 1 to 4 ms. For this few samples taken, care had to be taken to reset the contents in the shift register to zero before each run. Otherwise, the digits left over from the preceeding run would significantly affect the results of the new run. This was achieved

by doing several runs while blocking the laser. This clears out the shift register. For experiments in which a time-average is involved, such as the diffusion coefficient measurements, a large N_T (e.g. 10^6) is used, and this is not a problem.

The procedure for diffusion coefficient measurements is as follows. A constant sodium level was maintained, usually of the order of a few sodium atoms in the observation volume. The sample time ΔT was chosen such that the ratio of ΔT to the diffusion time τ_D was equal or less than 0.2. This assures that τ_D can be deduced with accuracy from the shape of the measured correlation function. Since only a rough estimate of τ_D was known before hand, several runs with different ΔT's were performed. While the laser was tuned to sodium resonance, the correlator was left on for 10^6 to 10^7 samples until a correlation function with high signal-to-noise was obtained. This corresponded to a measurement time on the order of minutes. To check the self-consistency of our measurements, the above procedure was repeated for different gas pressures and laser beam radii. Since the diffusion coefficient is temperature dependent, the temperature in the cell during the run needs to be measured. This was done later on by inserting a thermocouple in the observation volume. Calibration curves were made for the cell temperature for a given pressure and flow versus the temperature of the sodium pocket, which was recorded for each run. For the last

diffusion measurement run, the thermocouple was in place in the cell during the runs. The gas temperature was measured just after the correlation functions were taken, and the sodium atoms were heated directly by using the resistance wire wrapped on the chunk of sodium metal.

IV. SINGLE-ATOM DETECTION AND TRANSIT TIME MEASUREMENTS: PROGRESS TO DATE

Using the apparatus described in Chapter III. we have obtained single-atom correlation functions with regularity since fall of 1978. These correlation functions yielded apparent velocities on the order of 80 cm/sec. At that point, we thought that we had measured the velocities of individual sodium atoms in the helium flow. The frequency of occurrence of two-hump correlation functions when two laser beams were used, however, was lower than we estimated for the sodium level maintained during the experiments. This made us suspicious. Later on, when we calculated the effects of diffusion, we found that it played a much larger role than we had previously anticipated in the flow cell employed. In fact, for the typical experiments we performed, i.e., laser beams with $w = 65\ \mu m$ separated by about 800 μm and sodium atoms in 200 Torr of helium, the diffusion time calculated from our measurements in Chapter V was $\tau_D = w^2/4D \cong 6.6\ \mu sec$, while the apparent transit-time of the atom across a laser beam, $\tau_f = 2w/v$, was about 160 μs. In Fig. IV-1 we plotted τ_D at 200 Torr of helium and 40°C, a typical experimental condition, and τ_f for flow velocities $v = 100$ cm/sec, 500 cm/sec, and 1000 cm/sec as a function of beam radius, w.

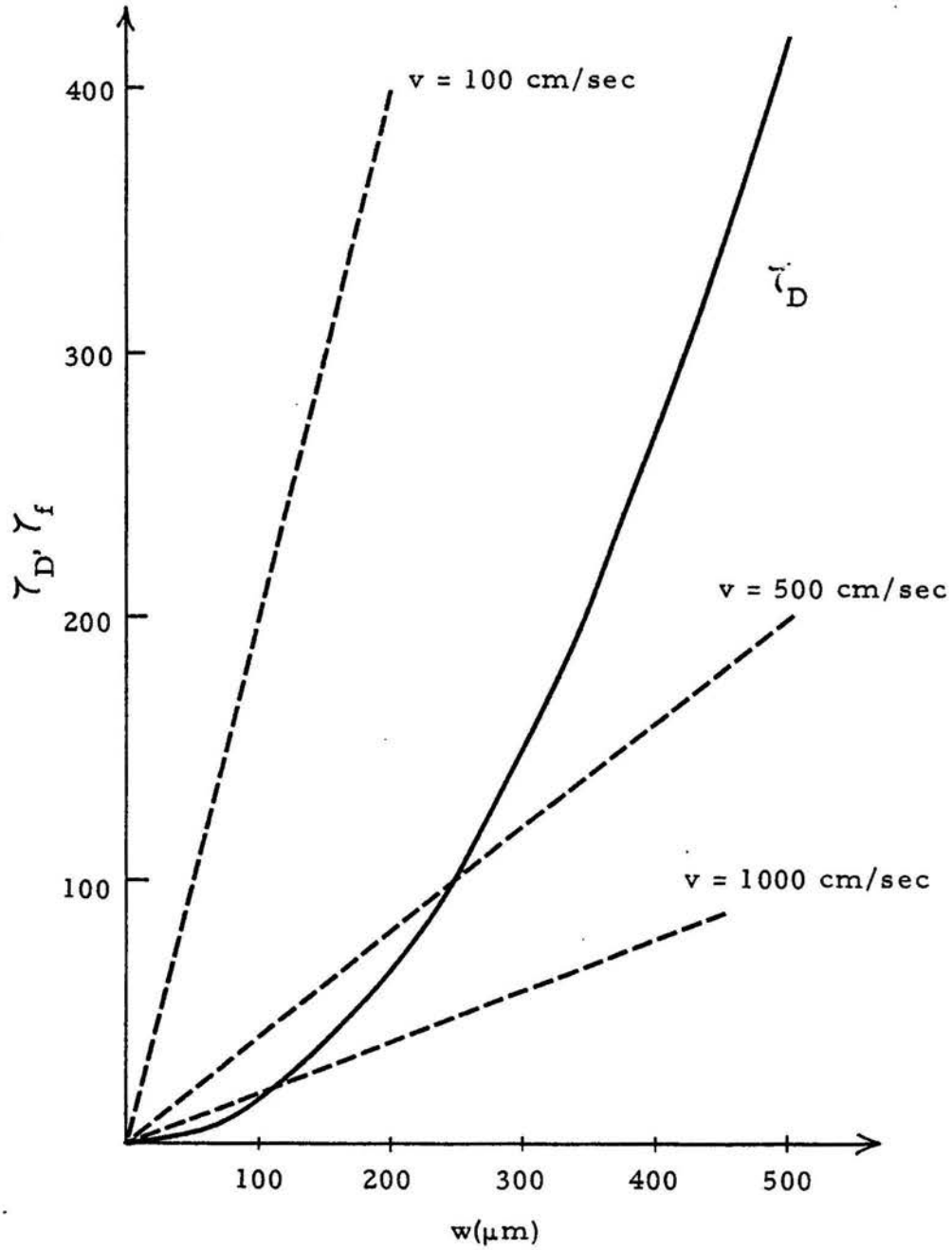

Fig. IV-1. γ_D at 200 Torr of helium and 40°C, and γ_f for flow velocities v = 100 cm/sec, 500 cm/sec and 1,000 cm/sec as a function of beam radius.

This figure helps to illustrate the beam radius and flow velocity necessary for the flow to overcome diffusion. Flow velocity measurements with large particles to be described in Sec. 4.1 indicated that the average flow velocity in these experiments was actually of the order of 1 cm/sec. Clearly, the correlation functions we observed did not represent flow velocity measurements due to the dominance of diffusion. Nevertheless, these were single-atom events registered in real-time. Furthermore, a rough estimate of an atom's transit time across a single laser beam could be extracted from the width of the single bursts. In Sec. 4.3, we present a probability analysis for the estimation of the burst size of the fluorescence counts due to a single sodium atom traversing one laser beam. This turned out to be in excellent agreement with our experimental results.

4.1 Estimate of Flow Velocity

In 200 Torr of helium buffer gas, the mean free path between collisions of sodium atoms and helium atoms is approximately 0.07 μm. This is at least a thousand times smaller than the characteristic dimension for diffusion in our experiments, i.e., the laser beam radius. As a result, the flow condition in our experimental set-up should be viscous as opposed to the free molecular flow or Kundsen flow. If, in addition, the flow is also laminar, the Poiseuille flow formula should apply. The velocity profile would then be parabolic,[23] i.e.,

$$v = v_o \frac{(R^2 - r^2)}{R^2}$$

$$= \frac{\Delta p}{4\eta_o \ell} (R^2 - r^2) \qquad (4.1a)$$

with the Reynolds number of the flow R_e defined by

$$R_e = \frac{\rho(2R)v_o}{\eta_o} , \qquad (4.1b)$$

where Δp and ℓ are the pressure drop and total length of the tube between pressure measurement stations respectively. These stations are located on both the inlet and pumping side of the central glass section. η_o is the viscosity of the flowing gas and ρ its mass density. R is the radius of the tube, and r is the distance of a point in the flow from the center of the tube. v_o is then the velocity at the center of the tube. In our apparatus, polyflow tubes with R = .2 cm were used to join the flow cell to the flowing gas tank and the vacuum system. The length ℓ, assuming only polyflow tube connect the two measurement stations, is equal to 275 cm. For helium, $\eta_o = 1.82 \times 10^{-4}$ poise and $\rho = 4.28 \times 10^{-5}$ gm/cm^3 at 200 Torr and 300 K. With $\Delta p \simeq 1$ Torr, typical for our single-atom correlation measurements, Eq. (4.1) predicts $v_o = 260$ cm/sec and $R_e = 24$ in the polyflow tube. Since the onset of turbulent flow occurs for $R_e > 2300$, this flow is obviously not turbulent before

entering the flow cell. For cell center section no. 2, the flow was first expanded into .4 cm radius glass tubing before entering the observation region. The flow velocity, according to Eq. (4.1) should reduce by a factor of 4, or $v_o = 65$ cm/sec. When the effect of the observation chamber is ignored, this is in reasonable agreement with the measured apparent velocity. Measurements of single-atom correlation functions yielded apparent velocities from 40 to 130 cm/sec. The big spread in velocities was then thought to be the result of turbulence in the flow inside the cell. It turned out that the actual flow velocity slowed down considerably in the big observation chamber.

The flow velocity in our apparatus for various pressure drops, Δp's, can be determined accurately by recording the single-particle correlation functions due to large particles in the flow using the very same methods as for single atoms. These particles were probably bits of sodium oxide inevitably formed each time fresh sodium metal was put in the cell, which broke off when the sodium pocket was heated up for the first time. Fortunately, they disappeared after the sodium pocket had been heated for several hours and did not interfere with single-atom measurements. In Fig. IV-2(a), (b) and (c) three single-particle correlation functions obtained for $\Delta p \simeq 1$ Torr, 4 Torr and 8 Torr, using one laser beam of diameter 288 μm, are shown. The velocities determined from the width of these

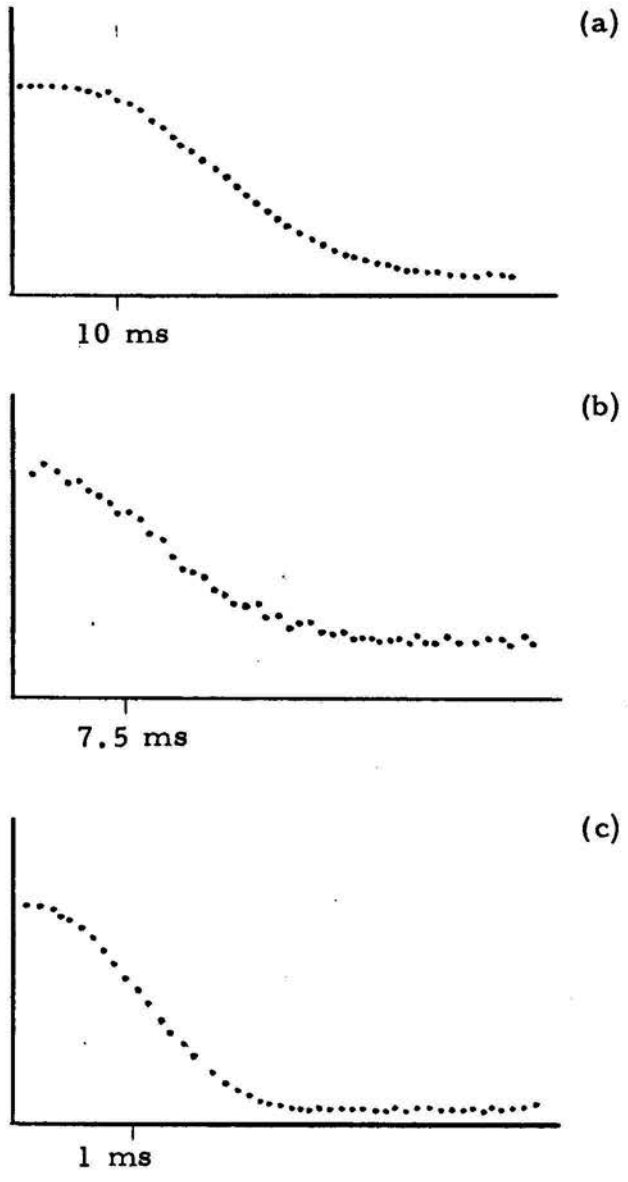

Fig. IV-2. Single-particle correlation functions obtained with one laser beam of radius w = 144 μm for (a) Δp = 1 Torr, (b) Δp = 4 Torr, and (c) Δp = 8 Torr, respectively.

correlation functions were 0.7 cm/sec, 1.4 cm/sec and 11 cm/sec for Fig. IV-2(a), (b) and (c) respectively. The error in all cases is less than 10%. In Fig. IV-3 we show three single-particle correlation functions obtained for $\Delta p \simeq 20$ Torr with two laser beams of radii 210 μm and 165 μm and separated by 670 μm. They were taken in sequence and the flow velocities were all about 80 cm/sec as determined from the separation of the two peaks. The velocities determined from $1/e^2$ of the peaks were between 75 cm/sec to 95 cm/sec. This indicates that the flow as determined by particles was actually rather uniform. Other experiments with a single laser beam also confirmed the uniformity of the flow.

The measured flow velocities, however, were not linearly proportional to Δp as predicted by Eq. (4.1a). This is because the flow slowed down considerably as it went from the polyflow tube into the much larger flow cell. Together with the actual measurements, however, Eq. (4.1a) provides a guide for rough estimate of flow velocities under different conditions.

4.2 Single-Atom Burst Correlation Functions

The significant experimental parameters of the single-atom correlation functions observed are listed in Table IV-1. These data are arranged in chronological order and should be examined together with the associated figures, Fig. IV-4 - IV-8.

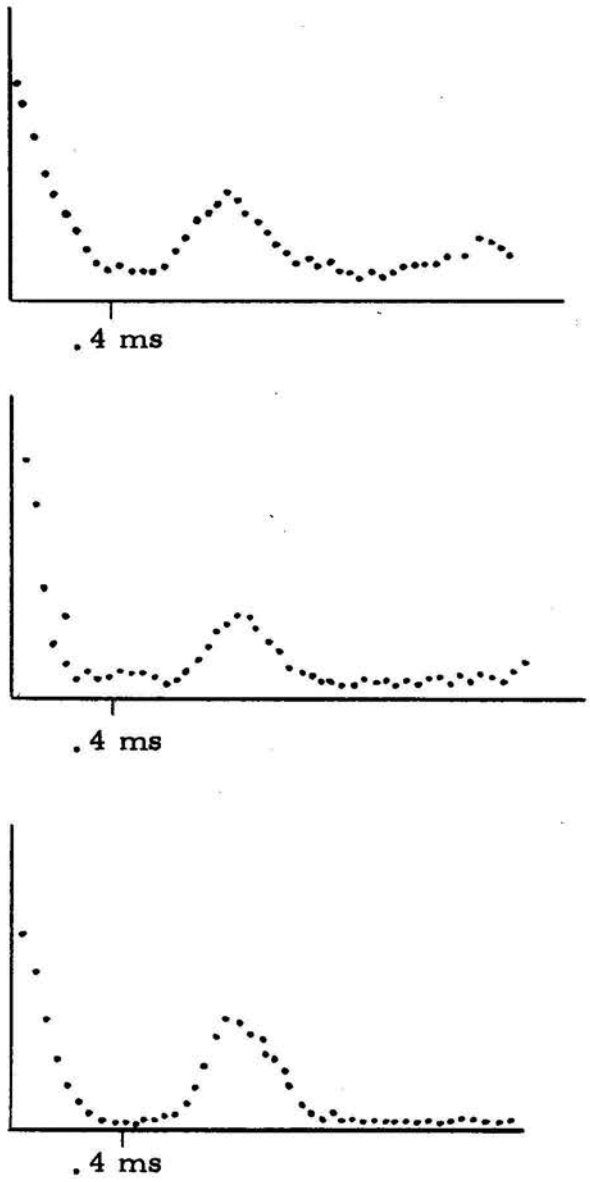

Fig. IV-3. Three consecutive single-particle correlation functions obtained with two laser beams of radii w = 210 μm and w = 165 μm and separated by 670 μm, Δp = 20 Torr.

Table IV-1. Experimental parameters for measured single-atom correlation functions.

Fig. No.	Laser power/ beam in the cell (mw)	Fluorescence count rate (counts/ sec)	Apparent velocity (cm/sec)	Estim. fluorescence counts (counts)	Observed signal counts (counts)	# of atoms in the observ. volume on the avg.	# of atoms entering laser beam during measurement time	Transit time/ atom/ beam (msec)	Comments
IV-4(a)	2	~ 1,000	38	32	32	0.05	0.6	1	2-beams
IV-5(a)	58	~22,000	41	16	18	0.16	1.2	1.7	1-beam I_2-cell used
IV-5(b)	18	~13,000	40	8	22	0.03	0.5	1	2-beams I_2-cell used
IV-6(a)	52	~39,000	50	11	40	0.3	2.5	1.4	1-beam I_2-cell used
IV-6(b)	21	~42,000	45	7	55	0.4	8.5	1.4	2-beams I_2-cell used
IV-7(a)	0.45	~13,000	97	58	42	0.2	1	.6	2-beams
IV-7(b)	0.5	~ 3,200	81	85	26	0.03	0.17	.6	2-beams

When we were first able to record single-atom correlation functions, our detection efficiency was only about 0.13%. This was primarily due to misalignment of the collection optics. The inlet of the central tube section then used (tube section no. 1 in Fig. III-2) was at a position such that it was not possible for us to move the first condenser lens to the desirable position, i.e. the laser beam being at the focus of that lens. The quantum efficiency of the photomultiplier used then, RCA 31034, was also lower, about 11%. In these earlier experiments, two laser beams of power 2 mw per beam, with radius $w = 75\ \mu m$, separated by $500\ \mu m$ were employed. One of the two-beam burst correlation function is shown in Fig. IV-3(a). Although it is rather noisy, a definite two-humped structure is seen. The velocity calculated from the separation of the two peaks is 38 cm/sec. Eq. (2.9) predicts 16 counts per transit per beam under these conditions, or 32 counts for an atom making a transit through the center of both beams, in good agreement with the observed signal. From the measured fluorescence rate, 1000 counts/sec, we estimated using Eq. (3.15) that there were 0.05 atoms on the average in the focal volume as defined earlier, and 0.6 average atoms entering the beams during the measurement time, 7×10^{-3} sec, using Eq. (3.16). Hence, it seemed likely to us then that Fig. IV-4(a) corresponded to a single sodium atom crossing both laser beams. We later realized that since diffusion was dominant, this probably

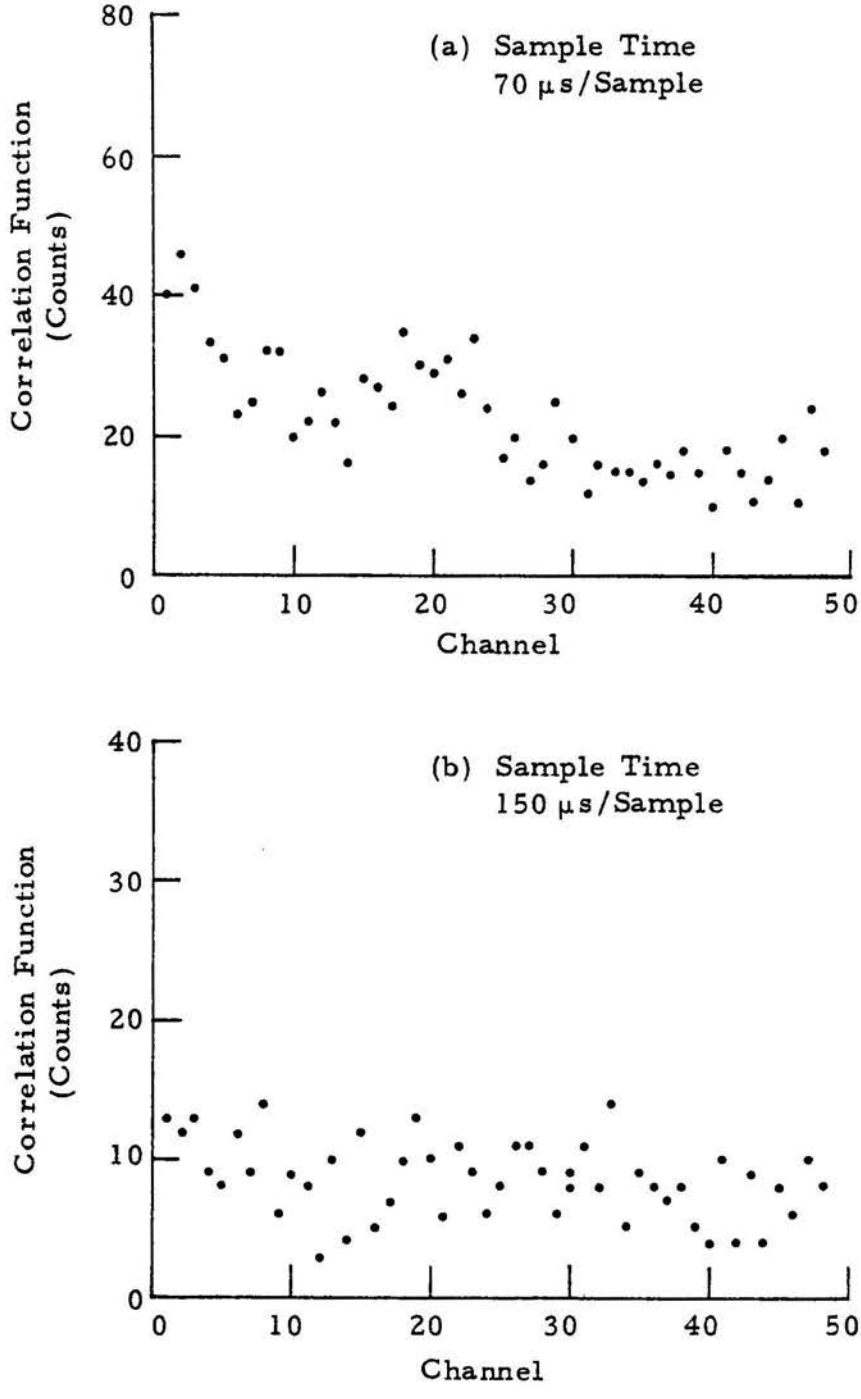

Fig. IV-4(a). Single-atom correlation function obtained with two 75 μm radii laser beams separated by 500 μm, with 2 mw per beam. (b) Correlation function due to noise counts obtained when no sodium atom was present.

represented two different atoms diffusing across the laser beams, with transit time approximately 1 ms per beam as estimated from $1/e^2$ points of each hump. Thus, the calculated velocity of 38 cm/sec is probably meaningless, but the agreement of counts with theory is not. When no atom was present or the laser was tuned off the sodium resonance line, the detected counts would not correlate. Fig. IV-4(b) shows such a correlation function.

To improve the quality of the observed correlation functions, more signal counts per atom per transit would be desirable. Using central tube section no. 2, which allows us to optimize the collection optics, and RCA 31034A high quantum efficiency photomultiplier operated at 1500 volts, the detection efficiency was increased to 0.4-0.5%. We also employed higher laser power in the cell. This requires the use of the iodine filter as described in Sec. 3.4 to prevent saturating the photomultiplier. Both single- and two-beam set-ups were used. In the former case, a laser beam of radius $w = 350\ \mu m$ was used. For the latter, the two laser beams with radii $w = 62.5\ \mu m$ separated by 725 μm were used. The I_2 cell temperature was set such that it attenuated the background scattering by a factor of 100. We later found out that at this temperature it also, unfortunately, attenuated the signal by a factor of 18 as discussed in Chapter III. As a result there is no net gain in signal-to-noise employing the I_2 filter. Fig. IV-5 illustrates single-atom burst

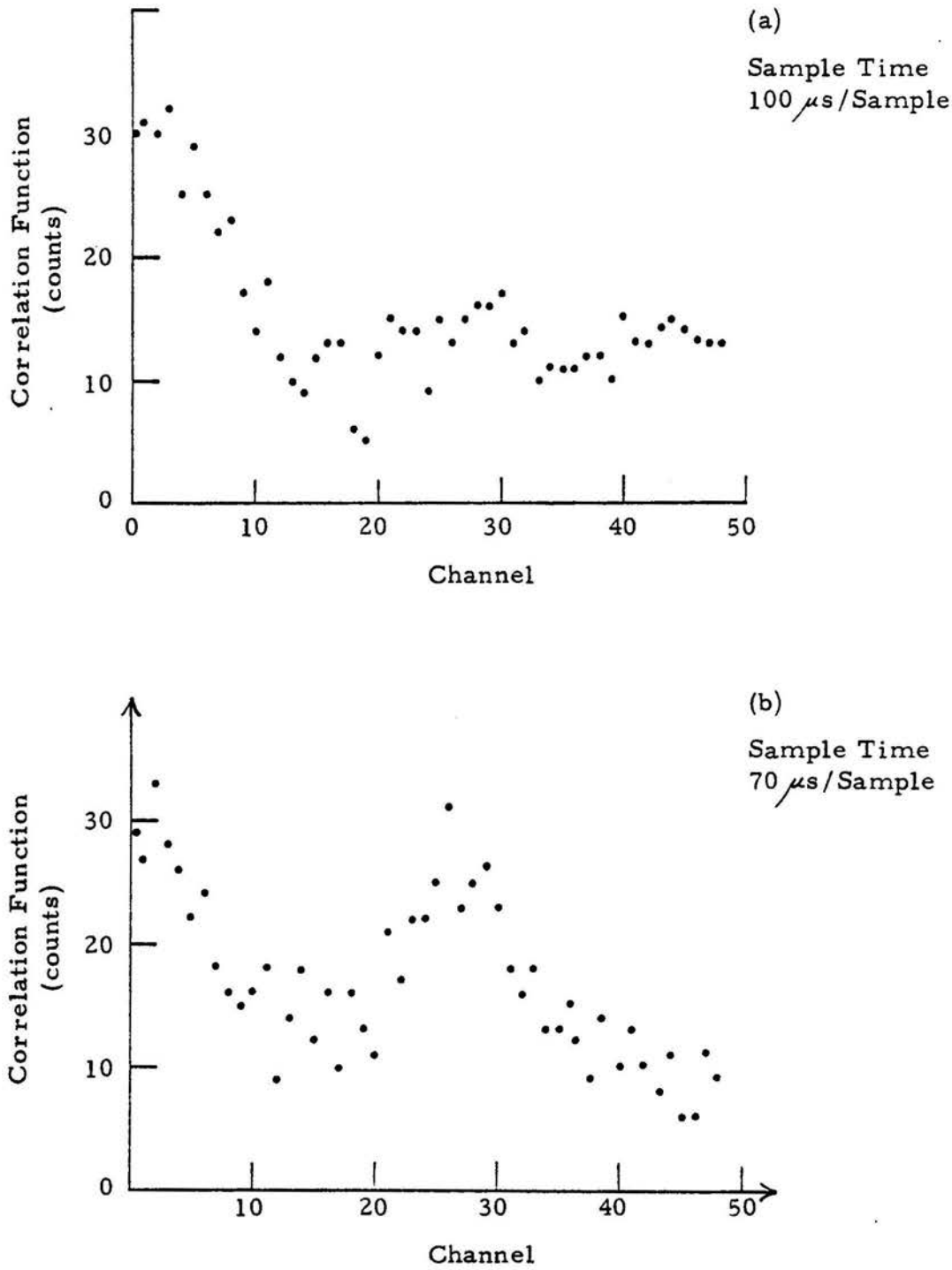

Fig. IV-5. Single-atom correlation functions obtained with (a) one laser beam of radius w = 350 μm and (b) two laser beams of radii w = 625 μm and separated by 725 μm. The iodine filter was used in these experiments.

correlation functions obtained using one- and two-beam techniques with the I_2 filter. Experimental parameters are given in Table IV-1. Note here the fluorescence rates were measured with I_2 cell removed and at reduced laser power.

Due to the statistical nature of the detection process, it is possible to detect more than the average expected counts. In fact, most of the correlation functions we observed had higher signal counts than we predicted for single atoms using Eq. (2.9), such as the one shown in Fig. IV-5(b). This, in part, may be the result of our particular experimental procedure, which requires the judgement of the experimentalist on whether a particular correlation function represented good data and was recorded or whether it was erased. This subjective criterion could mean accepting only those correlation functions which have higher signal-to-noise ratio than that for an average single-atom measurement. This can be partially remedied by monitoring the total clipped counts during the measurement time. Since the counts due to background could be clipped out to some extent, the total clipped counts is a measure of whether a burst was present or not.

The frequency of occurrence of measurable events as a function of sodium concentration was also checked and found to be in qualitative agreement with our expectation. When there was only a fraction of sodium atom on the average during the measurement time,

the occurrence of "distinctive" correlation functions was rather sporadic. The term "distinctive" means the quality of the correlation functions were at least as good as that shown in Fig. IV-4(a) and thus could be distinguished from the uncorrelated ones due to noise as that shown in Fig. IV-4(b). As the sodium concentration approached one atom per measurement time, the measurable two-humped events became appreciable, perhaps 10 in 200 tries. In addition, we also observed a comparable number of single-hump correlation functions. When the sodium density was further increased to about 5 atoms per measurement time, the number of measurable events increased to about 40 in 200 tries. These measurable events included single-hump, double hump, and even multi-hump correlation functions. The occurrence of multi-hump events became more frequent as the sodium density increased. As an example, a two-hump correlation function obtained using a single laser beam and a three-hump one obtained with two beams are shown in Fig. IV-6(a) and IV-6(b). Our calculation of the sodium level above was based on the assumption that sodium atoms traversed the laser beams at a constant velocity. In reality, diffusion was dominant. This is the primary reason for the discrepancy in frequency count and led us to suspect that diffusion was a problem.

To ascertain that these observed correlations functions are indeed due to sodium atoms, we also did a frequency count with the

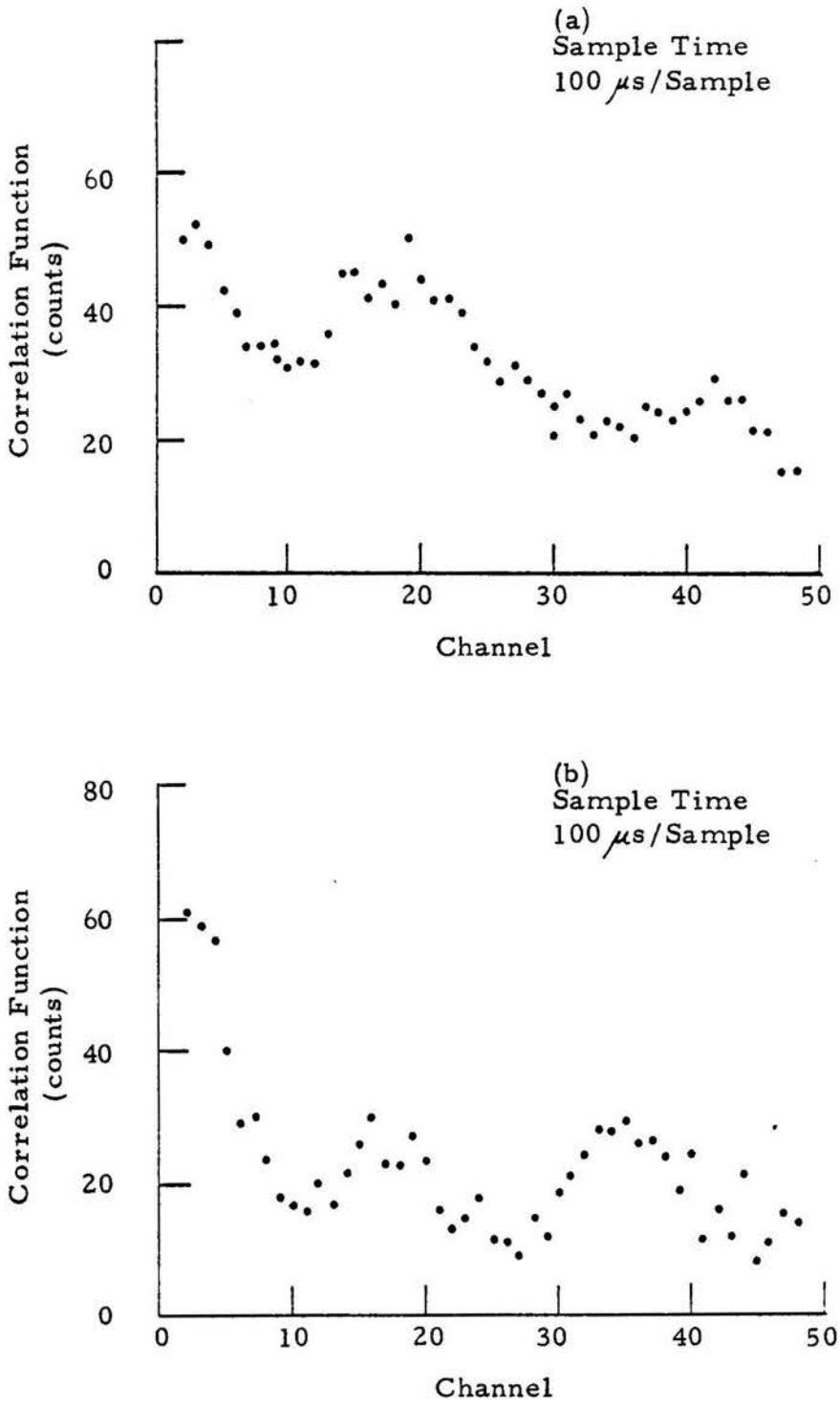

Fig. IV-6. Two multi-humped correlation functions obtained at higher sodium level with (a) one laser beam of radius w = 350 μm and (b) two laser beams of radii w = 625 μm and separation ℓ = 725 μm. The iodine filter was used in these experiments.

dye laser tuned off-resonance. The number of discernible correlation functions dropped drastically to a couple in 200 tries. These off-resonance events typically have poorer signal-to-noise than those observed on resonance. They may be the result of coincidental bunching of noise counts. Of course, it is also possible that there may still be small particulates present which could give signal off-resonance. When we further increased the sodium density to about 100 atoms during the measurement time, we observed only rare occurrence of marginal correlation functions, both on and off resonance. In this case, the focal region was flooded with sodium atoms and the bursts from different atoms were smeared together. This agreed with our discussions in Chapter II.

Assessing these earlier experiments, we concluded that the I_2 cell was not particularly helpful. The quality of the correlation functions observed did improve to some extent. This is probably due to the use of a higher quantum efficiency photomultiplier. Unfortunately, the task of checking sodium concentration after each correlation function became rather tedious. The photomultiplier had to be turned off and I_2 cell pulled out before the fluorescence count rate could be measured at a lower power level. As a result, we typically only checked sodium concentration at the beginning and end of the day. This undoubtedly introduced error in our estimation of sodium concentration. In addition, we oversaturated the transition in the

experiments using two beams, resulting in an unnecessary increase in background scattering. Here we were limited by the size of the last diaphragm. Larger beams just would not fit cleanly through the cell. We also concluded that it would be desirable to further increase the detection efficiency. Then we would attain the same level of signal counts using less laser power, and hence eliminate the need for the I_2 cell. Higher detection efficiency was achieved by operating the photomultiplier at 1800 V. This increased the photon counting efficiency by a factor of two. Background scattering also increased by a factor of two. Using a higher clipping level, however, we could clip out part of the background noise. This resulted in improvement in the quality of the correlation functions observed.

Two of the correlation functions obtained in this manner are shown in Fig. IV-7. Two laser beams of radius $w = 65\ \mu m$, separated by 875 μm were used. The detection efficiency as determined by Rayleigh scattering was 1.2%. Note that the sodium level when Fig. IV-7(b) was taken was very low (about 0.03 atoms in the observation volume). As a result, we recorded about four two-hump correlation functions during a two-hour period, in addition to several single-hump correlation functions.

Summarizing the experimental data we accumulated up to this point, we found that at 200 Torr of helium with $\Delta p \leq 1$ Torr, the

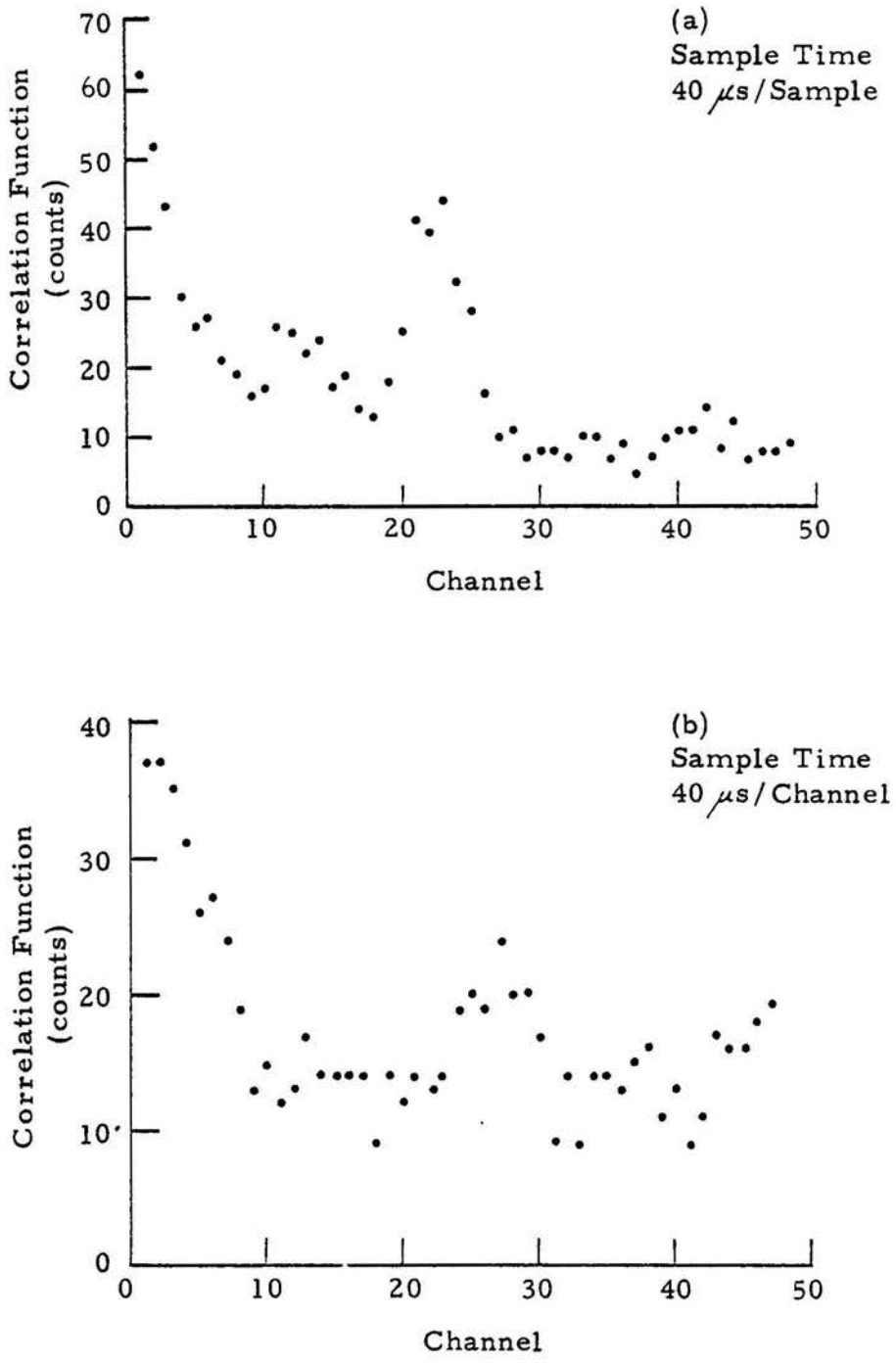

Fig. IV-7. Two single-atom correlation functions obtained with two laser beams with w = 65 μm and separation ℓ = 875 μm.

flow velocities as determined from single-atom correlation functions varied from 40 cm/sec to 130 cm/sec. We then thought perhaps turbulence was responsible for this large velocity variation. In order to see whether an average flow velocity could be determined, we integrated over many atoms with two beams. Instead of the two broad peaks as expected, a decay type of correlation function was observed. This suggested that either the degree of turbulence was huge or some additional physical processes were present. A rough calculation indicated that diffusion would be as important as flow at the pressure, flow rate and beam radius employed in these experiments. It is quite possible that an atom diffused sideways after it passed through the first beam and missed the second beam completely. For example, for the condition of Fig. IV-7(a), the sideways diffusion time is about 6.6 μs, whereas the assumed time-of-flight across the two beams was 0.9 msec. This probably explains the occurrence of single-hump correlation functions. A diffusing atom could also spend longer or shorter time in the beam that an atom traveling at constant velocity, thereby emitting more or less photons. Thus, the two-hump correlation functions we observed may represent two different atoms, one diffusing through each beam, or one atom diffusing out of one beam and back into it, etc. We can be pretty sure, however, that each burst observed was due to a single atom crossing one beam.

Examining the experimental correlation functions obtained up to this point, we concluded that we have detected individual sodium atoms in helium buffer gas by registering the atom as it diffused across the laser beam. Because of the dominance of diffusion in the flow cell, we were not able to measure flow velocities. The transit time of the atom diffusing across the beam could, however, be determined. The theory we developed in Chapter II was also shown to provide an adequate description of these single-atom measurements.

4.3 Probability Analysis

In order to compare more accurately the observed number of counts per transit with theory, we did a probability analysis on the photocounts entering the correlator. This was performed using the probability density mode of the correlator, which was described briefly in Sec. 3.5.

Briefly, the photoelectron statistics due to a constant background level are purely random and therefore should yield a Poisson distribution. The fluorescence photons emitted by an atom traversing the laser beam, on the other hand, are not random, but occur in bursts. Thus, a comparison of the probability distribution of the detected counts on and off resonance should provide information on the size of the bursts of fluorescence photons due to individual sodium atoms crossing the laser beam. Such an analysis would not

be prejudiced by operator selection of only "good" looking correlation functions.

In the following, we will study only the case of an atom in straight line motion. To take diffusion into account, a model for the trajectory of the random motion of the diffusing atom must be developed. This will not be attempted here.

Consider an atom traversing a laser beam with constant velocity v normal to a plane parallel to the long dimension of the rectangular photocathode and containing the laser beam. The sample time ΔT is chosen to be much longer than the transit time of the atom across the laser beam so that the whole burst will occur in one sample time. The probability of C_T total counts, which is a sum of a counts due to an atom entering the laser beam and $C_T - a$ counts due to background scattering, in a fixed sample time ΔT is given by the following expression:

$$\text{Prob. of } C_T \text{ total counts} = \sum_{a=0}^{C_T} \text{Poisson Prob. of } (C_T - a) \text{ noise counts}$$

$$\times \left[(\text{Prob. of } a \text{ counts due to an atom}) \times \begin{pmatrix} \text{Prob. of an atom} \\ \text{crossing the} \\ \text{planar area} \end{pmatrix} \right.$$

$$\left. + \begin{pmatrix} \text{Prob. of no atom crossing} \\ \text{planar area} \end{pmatrix} \delta_{a0} \right] . \qquad (4.2)$$

In Eq. (4,2), the Poisson prob. of $(C_T - a)$ noise counts is

$$\frac{(\bar{n}_{noise})^{C_T - a} e^{-\bar{n}_{noise}}}{(C_T - a)!} , \tag{4.3}$$

where $\bar{n}_{noise}$ is the average noise counts per sample time. The probability of detecting a counts due to a sodium atom is also a Poisson distribution,

$$\frac{[\bar{n}_f(b, z)]^a \; e^{-\bar{n}_f(b, z)}}{a!} \tag{4.4}$$

which peaks at $\bar{n}_f(b, z)$, the average fluorescence counts due to an atom traversing the planar area defined above at an impact parameter b and linear distance z from the center of the observation volume along the laser beam. From the discussion of Sec. 3.6, $\bar{n}_f(b, z)$ is given by

$$\bar{n}_f(b, z) = f_1(z/l) \; f_2(b/w) \; \epsilon\eta F , \tag{4.5}$$

where $\epsilon\eta F$ is the maximum average number of fluorescence counts expected from a sodium atom traversing the laser beam. $f_1(z)$ is the detector aperture function plotted in Fig. III-4. $f_2(b/w) = F_b/F_{max}$ has been plotted in Fig. II-2.

Eq. (3.12) gives an expression for Nv, the total number of sodium atoms per cm^2/sec. Hence, the probability of a sodium atom traversing with velocity v a unit area $\Delta b \Delta z$ at a point (b, z) on the y-z plane in sample time ΔT can be written as:

$$P_a(b,z) = \frac{(\Delta b)(\Delta z)\, R_F\, \Delta T}{(0.77)(1.12)\, \epsilon\eta F\, w(1\text{ cm})}, \qquad (4.6)$$

R_F is the fluorescence count rate defined by Eq. (3.8). The denominator factors, 0.77 and 1.12, are normalization factors for $f_1(z)$ and $f_2(b/w)$, respectively, as described in Chapter III. The probability of no atom present in $(\Delta b)(\Delta z)$ is simply $1 - P_a(b,z)$. Now we can rewrite Eq. (4.2) as:

$$\text{Prob. of } C_T \text{ total counts} = \sum_{a=0}^{C_T} \frac{(\bar{n}_{noise})^{C_T - a}\, e^{-\bar{n}_{noise}}}{(C_T - a)\,!} \Bigg\{ \sum_{b/w=0}^{2} \sum_{z=-1.2}^{1.2} \frac{(\Delta b/w)(\Delta z)\, R_F\, \Delta T}{(.77)(1.12)(1)(\epsilon\eta F)} \frac{[\bar{n}_f(b,z)]^a\, e^{-\bar{n}_f(b,z)}}{a\,!}$$

$$+ \left(1 - \sum_{b/w=0}^{2} \sum_{z=-1}^{1} \frac{(\Delta b)(\Delta z)}{(\Delta b)(\Delta z)} \left[\frac{R_F \Delta T\, (\Delta b/w)(\Delta z)}{(.77)(1.12)(1)(\epsilon\eta F)}\right] \delta_{ao}\right)\Bigg\} \quad . \qquad (4.7)$$

As we have discussed in Sec. 3.6, the upper limit for b/w is actually infinity and z varies from $-\infty$ to $+\infty$. For calculation purposes, $f_1(z/1)$ and $f_2(b/w)$ are effectively zero beyond the limits set in Eq. (4.7).

Typically, the sample time ΔT is chosen to be several times larger than τ_f, the transit time of the atom traversing the beam. Nevertheless, it is possible that in some cases, the burst of fluorescence photons could be split between two adjacent samples, which we call samples 1 and 2. Taking this into account, Eq. (4.7) should be modified as,

$$\text{Prob. of } C_T \text{ total counts} = \sum_{a=0}^{C_T} \frac{(\bar{n}_{noise})^{C_T-a} e^{-\bar{n}_{noise}}}{(C_T-a)!} \Bigg\{ \sum_{z=-1.2}^{1.2} \sum_{b/w=0}^{2} \frac{(\Delta b/w)(\Delta z) R_F \Delta T}{(.77)(1.12) \cdot (1) \epsilon \eta F}$$

$$\times \sum_{p'=0}^{2.1} \left[\frac{\bar{n}_{f,1}(b, z, p')^a e^{-\bar{n}_{f,1}(b, z, p')}}{a!} + \frac{\bar{n}_{f,2}(b, z, p')^a e^{-\bar{n}_{f,2}(b, z, p')}}{a!} \right] \frac{\Delta p'}{2.1}$$

$$+ \left[1 - (2) \sum_{z=-1.2}^{1.2} \sum_{b/w=0}^{2} \frac{(\Delta b/w)(\Delta z) R_F \Delta T}{(.71)(1.12) \epsilon \eta F} \right] \delta_{a0} \Bigg\} . \qquad (4.8)$$

The expressions

$$\bar{n}_{f,1}(b, z, p') = f_1(z)\ f_2(b/w)\ f_3(p', x)\ \epsilon\eta F \qquad (4.9)$$

$$\bar{n}_{f,2}(b, z, p') = f_1(z)\ f_2(b/w)\ (1 - f_3(p', x))\ \epsilon\eta F \qquad (4.10)$$

are the average fluorescence counts due to an atom traversing the laser beam at (b, z) recorded in sample 1 and sample 2 respectively. The function

$$f_3(p'x) = \int_{-\infty}^{p'} \frac{du}{e^{u^2} + x} \Big/ \int_{-\infty}^{\infty} \frac{du}{e^{u^2} + x} \qquad (4.11)$$

is the fraction of the fluorescence counts in sample 1 and $(1 - f_3(p', x))$ is the fraction of the counts in sample 2. The parameter $p' = \frac{\sqrt{2}vt}{w}$ is a normalized time fraction which ranges from 0 to $p'_{max} = \frac{\sqrt{2}v}{w}\frac{\Delta T}{2}$. Fig. IV-8 plots $f_3(p', x)$ vs p' from $p' = 0$ to $p'_{max} = 2.1$, a typical experimental condition and $x = 1.91$, the optimum value. The additional factor of 2 in the last term of Eq. (4.8) is needed to account for the fact that each burst of fluorescence photons is assumed to occupy two sample periods in this analysis.

Fig. IV-9 illustrates a typical probability distribution of recorded counts both on and off resonance. A laser beam of radius $w = 65\ \mu m$ at a power of 1.4 mw was used. The detection efficiency

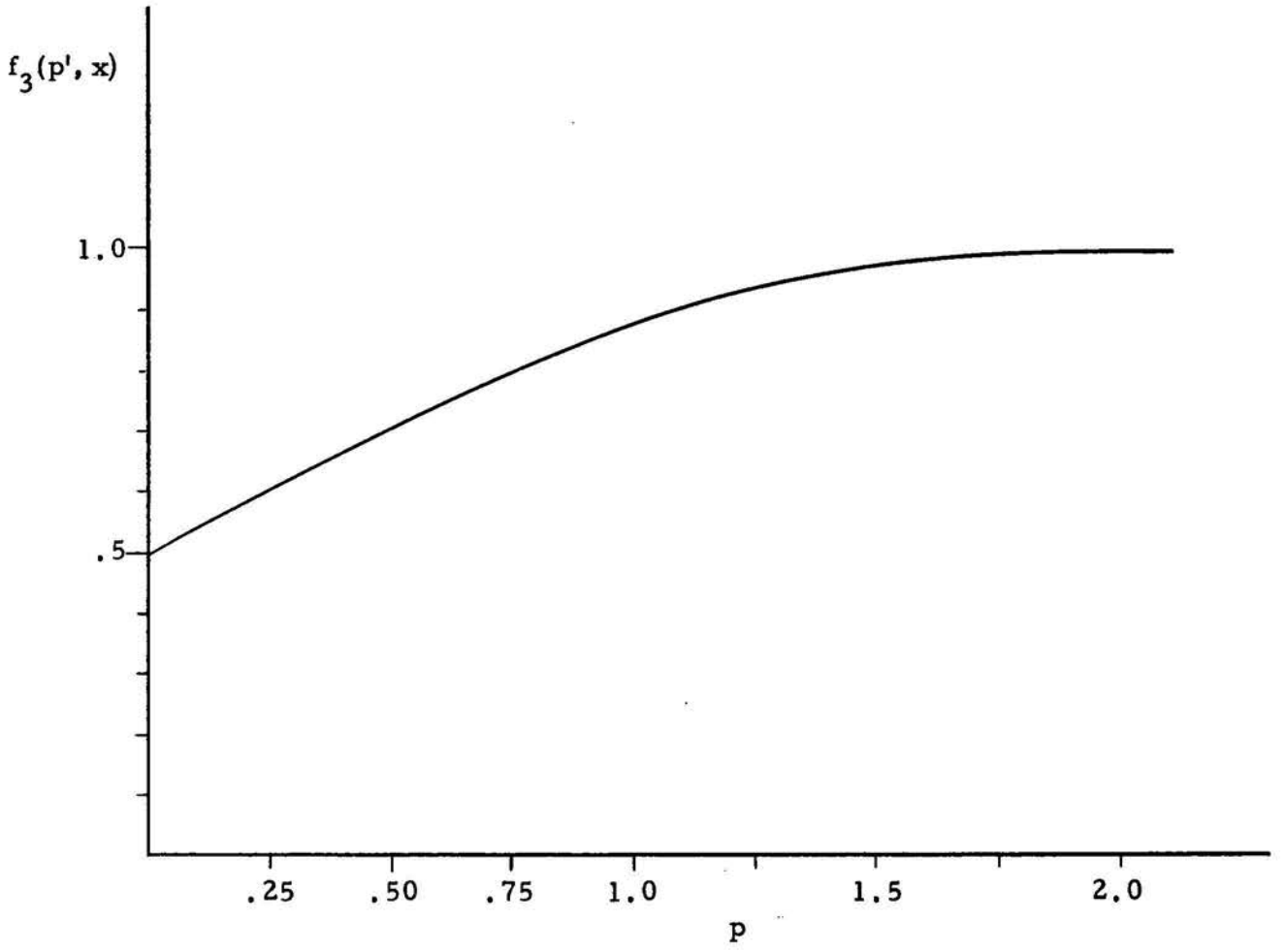

Fig. IV-8. The function $f_3(p', x) = \int_{-\infty}^{p'} \frac{du}{e^{u^2}+x} \Big/ \int_{-\infty}^{\infty} \frac{du}{e^{u^2}+x}$ versus p', where $p' = \frac{\sqrt{2}\,vt}{w}$.

was 0.5%. The sample time ΔT was set to be 250 μs in both runs. For the on resonance run, the fluorescence count rate, R_F, was 3800 counts/sec, or $\bar{n}_f = 0.95$ counts/sample. This corresponded to 0.06 atoms on the average in the observation volume. The background scattering contributed $\bar{n}_{noise} = 14.25$ counts/sample. Thus, the total counts/sample, $\bar{n}_{total} = \bar{n}_f + \bar{n}_{noise}$, was equal to 15.20. The off-resonance run was done at slightly higher laser power so that the total count rate would be approximately equal in both runs. The probability distribution for the off-resonance run (presumably all noise) can be fitted to a Poisson distribution with $\bar{n}_{noise} = 15.79$ very nicely. The on-resonance curve, even with slightly fewer average counts/sample, showed that sample periods with 26 counts or more occurred more often than the Poisson-distribution off-resonance run. These samples must then contain correlated bursts of fluorescence counts from individual sodium atoms. Using the experimental parameters in Eq. (4.8), we were able to generate theoretical probability distribution with different F's. Examining these curves, we found that if $\epsilon\eta F$ was increased by three counts, say, the corresponding probability distribution in the tail region would also be shifted over by approximately the same amount. Thus, a rough estimate of $\epsilon\eta F$ could be obtained by comparing the on- and off-resonance probability distributions in the tail region of the two curves. Examining Fig. IV-9, we could estimate $\epsilon\eta F$ to be

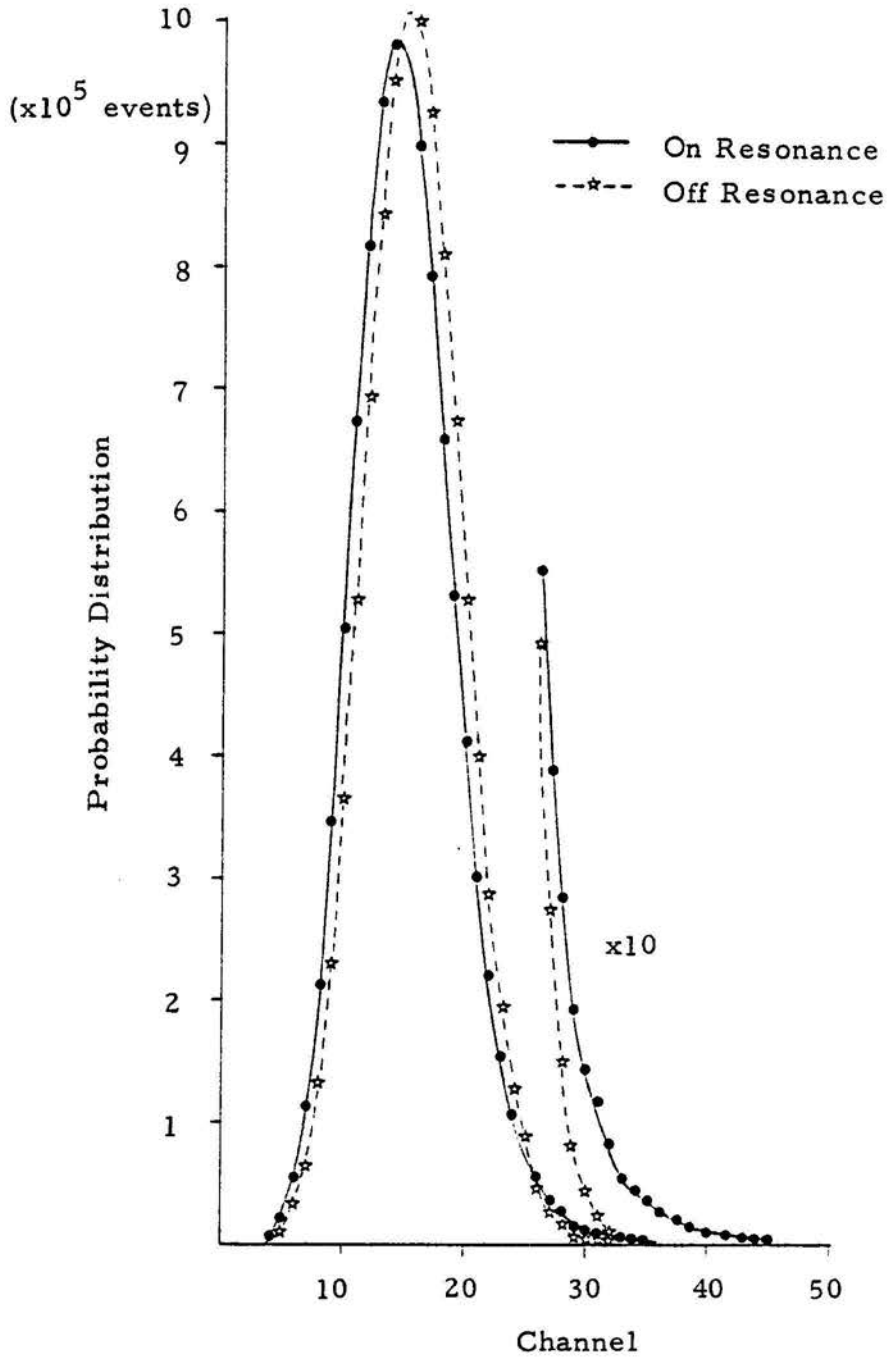

Fig. IV-9. Probability distribution of detected counts both on and off-resonance. A single laser beam of radius w = 65 μm at laser power p = 1.4 mw was used. The sample time is ΔT = 250 μs.

12 counts. Figure IV-10 gives the on-resonance probability distribution with the theoretical curve using Eq. (4.8) for $\epsilon\eta F = 15$ counts. The agreement is very good. According to Eq. (2.13), this corresponds to a diffusing time of 65 μs. Although 15 counts of signal agrees with what is observed in single-atom burst experiments. This time is longer than the diffusion time $\tau_D \simeq 7$ μs, estimated from our diffusion coefficient measurements. This suggests that a better model for Eq. (2.13) is needed to handle the case when diffusion is dominant. In addition, Eq. (4.8) does not strictly apply because diffusion was dominant in these experiments. Nevertheless, a sodium atom entering the laser beam, whether it travels with a mean flow velocity or just diffusing, would emit a burst of correlated fluorescence photons. The above described experiments and analysis clearly demonstrated this fact. This is additional proof that the correlation functions we described in Sec. 4.2 were single-atom events registering the transit of individual sodium atoms across the laser beam.

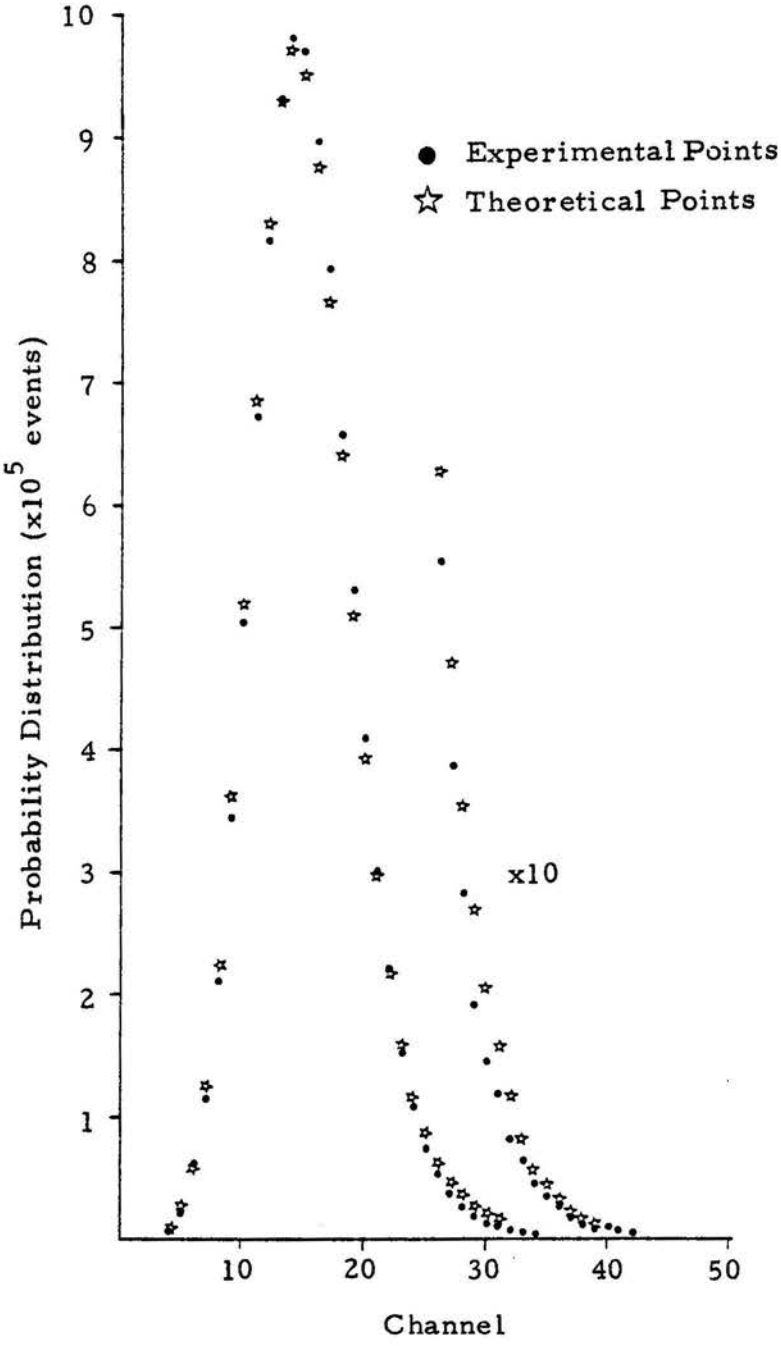

Fig. IV-10. The probability distribution of detected counts on resonance as shown in Fig. IV-9 is now shown with the theoretically predicted distribution with $\epsilon \eta F = 15$ counts.

V. DIFFUSION COEFFICIENT MEASUREMENTS

The phenomenon of diffusion is the transfer of mass from one region of space to another that occurs because of a gradient in the concentration of that material. This transfer of mass occurs through the random thermal motion of the molecules themselves. The diffusion coefficient is just the flux of molecules of species i due to a unit gradient in the number density of i. For a binary mixture of gases, in the absence of temperature and pressure gradients, external forces and chemical reactions, the flux equations are

$$\vec{J_1} = -D_{12} \vec{\nabla} n_1 \tag{5.1}$$

$$\vec{J_2} = -D_{21} \vec{\nabla} n_2 \tag{5.2}$$

The subscripts 1, 2 denote the species. n_1, n_2 are number density of the molecules, $\vec{J_1}$ and $\vec{J_2}$ are flux densities (in molecules/cm^2 sec). Under conditions of uniform total pressure and temperature, $D_{12} = D_{21}$. In this chapter, we will first present predictions for the diffusion coefficients of the Na-He and Na-Ar systems based on kinetic theory in Sec. 5.1. In Sec. 5.2, experimental data are shown and deduced experimental diffusion coefficients are compared with theory and the results of previous experiments.

5.1 Theoretical Predictions

In the following discussion, we will limit ourselves to the considerations of trace amounts of tagged molecules with mass m_1 and diameter d_1 in a stationary gas of molecules with mass m_2 and diameter d_2. Only a summary of relevant formulae will be given. Basic kinetic theory has been discussed in numerous textbooks such as ref. 24. For more details, the readers are referred to the works of Hirschfelder et al.[25] or Chapman and Cowling.[26]

Elementary considerations based on the concept of mean-free-path and the assumption that molecules are hard spheres of diameters d_1 and d_2 yield the following expressions for the diffusion coefficient D_{12},[24]

$$D_{12} = 1/3 \left[\frac{n_1 \lambda_2 \bar{v}_2 + n_2 \lambda_1 \bar{v}_1}{n_1 + n_2} \right] . \tag{5.3}$$

For $n_1 \ll n_2$, this reduces to

$$D_{12} = 1/3 \, \lambda_1 \bar{v}_1 . \tag{5.4}$$

The quantities $\bar{v}_1$ and $\bar{v}_2$ are the mean thermal speeds of species 1 and 2 respectively. They are

$$\bar{v}_i = \sqrt{\frac{8kT}{\pi m_i}} , \quad i = 1, 2 . \tag{5.5}$$

$\lambda_1 = \tau_{12}\,\bar{v}_1$, $\lambda_2 = \tau_{12}\,\bar{v}_2$ are the mean free paths with $\tau_{12} = (n\bar{v}_r \pi d_{12}^2)^{-1}$, the mean time between collisions of unlike molecules. $n = n_1 + n_2$ is the total number density, $\bar{v}_r = (\bar{v}_1^{\,2} + \bar{v}_2^{\,2})^{\frac{1}{2}}$ is the mean relative speed and $d_{12} = \frac{1}{2}(d_1 + d_2)$ is the average collision diameter. Substituting Eqs. (5.4) and (5.5) into (5.3), we get

$$D_{12} = \frac{2}{3}\sqrt{\frac{2kT}{\pi\mu}}\,\frac{1}{n\pi d_{12}^2} = \frac{2}{3}\sqrt{\frac{2k^3T^3}{\pi\mu}}\,\frac{1}{p\pi d_{12}^2}\,, \qquad (5.6)$$

which gives the correct temperature and pressure dependence as predicted by the more rigorous theory for hard spheres, i.e., $D_{12}\,p =$ constant at constant temperature and D_{12} is proportional to $T^{3/2}$ at constant pressure. Unfortunately, Eq. (5.6) also predicts

$$\frac{(D_{12})_{n_1 \ll n_2}}{(D_{12})_{n_2 \ll n_1}} = \left(\frac{\bar{v}_1}{\bar{v}_2}\right)^2 = \frac{m_2}{m_1}\,. \qquad (5.7)$$

That is, D_{12} has a concentration dependence when the mass of molecules of one type is much larger than the other. Experiments have proven to the contrary.

More precise treatments of the transport properties of gases such as diffusion coefficients require solving the Boltzman equation.

The theory of non-uniform gases first developed by Chapman and Enskog[25, 26] is accurate insofar as it obtains a solution for the Boltzman equation, based on certain molecular models. The basic assumptions of this theory are as follows: (1) Only binary collisions are considered. This is valid for gases with the ratio of mean free path to molecular diameter larger than 100, i.e. for buffer gas pressures up to 1 atmosphere at room temperature. (2) Classical mechanics are used. This assumption is valid for most cases, since above 200 K, the quantum effects are less than 1% even for the light elements. (3) The gradients of the physical quantities are small. In other words, the experimental conditions deviate only slightly from thermal equilibrium such that the transport fluxes are linear in the gradient, as in Eqs. (5.1) and (5.2). (4) Collisions are elastic. We recall that inelastic collisions of ground state molecules at thermal velocities occur only between molecules with internal degrees of freedom. (5) The characteristic dimensions, i.e. the laser beam diameters, are much larger than the molecular mean free path. Our experiments involved trace amount of sodium atoms diffusing in helium or argon buffer gas at pressures from 10 to 400 Torr. The cell temperature is always above 300 K. Hence, all the above assumptions are valid.

The general expression for the diffusion coefficient is[25]

$$D_{12} = \frac{3}{16}\left(\frac{kT}{\mu}\right)\frac{1}{n\sigma_D(T)}, \qquad (5.8)$$

where $\mu = \frac{m_1 m_2}{m_1 + m_2}$ is the reduced mass of the pair of molecules.

The quantity $\Omega_D(T)$ is the collision integral for diffusion which is in general temperature dependent through $\bar{v}_r$, the initial relative speed of the two colliding molecules. It is given by

$$\Omega_D(T) = \sqrt{\frac{kT}{2\pi\mu}} \int_0^\infty e^{-g^2} g^5 \sigma_D(v_r)\, dg \,, \tag{5.9}$$

with $g = \sqrt{\frac{\mu}{2kT}}\, v_r = \sqrt{\frac{\mu}{2kT}} \left| \vec{v}_2 - \vec{v}_1 \right|$, the reduced initial relative speed. The diffusive transport cross section, $\sigma_D(v_r)$, is

$$\sigma_D(v_r) = 2\pi \int_0^\infty (1 - \cos \chi(v_r, b))\, b\, db \,, \tag{5.10}$$

in which b is the impact parameter, and $\chi(v_r, b)$ is the deflection angle between the initial and final relative velocity vectors of the colliding molecules. For any spherically symmetric interaction potential $\phi(r)$, $\chi(v_r, b)$ can be written as

$$\chi(v_r, b) = \pi - 2b \int_{r_m}^\infty \frac{dr/r^2}{\sqrt{(1 - \phi(r)/\frac{1}{2}\mu v_r^2) - b^2/r^2}} \,, \tag{5.11}$$

where r_m is the distance of closest approach of the two molecules. It is obtained through

$$b^2/r_m^2 = 1 - \phi(r_m)/\tfrac{1}{2}\mu v_r^2 \quad . \tag{5.12}$$

Thus, given $\phi(r)$, one can in principle use Eq. (5.8) through (5.12) to calculate D_{12}. As an example, we will consider the hard sphere model, i.e.,

$$\phi(r) = \infty \qquad \text{if} \quad r \leq d_{12}$$

$$0 \qquad\qquad r > d_{12} \quad . \tag{5.13}$$

The distance of closest approach of two colliding molecules is $r_m = d_{12}$ if $b \leq d_{12}$ and $r_m = b$ for $b \geq d_{12}$. Substituting in Eq. (5.11), we get

$$\chi(v_r, b) = 2 \arccos(b/d_{12}) \quad b \leq d_{12}$$

$$0 \qquad\qquad b > d_{12} \quad . \tag{5.14}$$

Using Eq. (5.14) in Eq. (5.10), we find $\sigma_D = \pi d_{12}^2$, independent of the relative velocity. Eq. (5.9) then gives

$$\nu_D = \sqrt{\frac{kT}{2\pi\mu}}\ \pi d_{12}^2 \quad .$$

Finally, we obtain the following expression for the diffusion coefficient,

$$D_{12} = \frac{3}{16}\left(\frac{2\pi kT}{\mu}\right)^{\frac{1}{2}} \frac{1}{n\pi d_{12}^{2}} \quad . \tag{5.15}$$

In contrast with Eq. (5.6), Eq. (5.15) predicts that D_{12} is independent of the composition of the mixture of gases, a result in approximate agreement with experiments. In practical units, Eq. (5.15) can be rewritten as,

$$D_{12} = 2.628 \times 10^{-3} \frac{\sqrt{T^3(M_1+M_2)/2M_1M_2}}{pd_{12}^{2}} \tag{5.16}$$

where M_1, M_2 are molecular weights in amu/mole, p is the total pressure in atmospheres, d_{12} is in Å, and D_{12} is in cm^2/sec.

To evaluate D_{12} for the Na-He and Na-Ar systems we studied, we first calculated the atomic diameters d_{Na}, d_{He} and d_{Ar} from experimental viscosity and self-diffusion data. The formulae for self-diffusion coefficients D (cm^2/sec) and viscosity η_o (gm/cm sec) are respectively,[26]

$$D = 2.628 \times 10^{-3} \frac{\sqrt{T^3/M}}{pd^{2}} \tag{5.17}$$

and

$$\eta_o = 2.6693 \times 10^{-7} \frac{\sqrt{MT}}{d^{2}} \tag{5.18}$$

where M is the molecular weight in amu/mole, T is the temperature in K and d is the diameter in Å. The average of the diameters calculated from self-diffusion and viscosity are used. For helium and argon, the experimental values are taken from tables in reference 26. Using viscosity data, we obtained $d_{He} = 2.19\text{Å}$ and $d_{Ar} = 3.66\text{Å}$, while experimental self-diffusion coefficients of helium and argon yield $d_{He} = 2.1\text{Å}$ and $d_{Ar} = 3.46\text{Å}$. For sodium, the viscosity data of reference 27 is used. We find $d_{He} = 2.15\text{Å}$, $d_{Ar} = 3.56\text{Å}$ and $d_{Na} = 4.98\text{Å}$; hence, $d_{Na\text{-}He} = 3.57\text{Å}$ and $d_{Na\text{-}Ar} = 4.27\text{Å}$. Eq. (5.15) then predicts $D_{Na\text{-}He} = 0.5\ \text{cm}^2/\text{sec}$ and $D_{Na\text{-}Ar} = 0.17\ \text{cm}^2/\text{sec}$ at S.T.P.

More realistic models take into account the intermolecular forces more accurately by using a potential such as the Lennard-Jones potential:

$$\phi(r) = 4\epsilon_{12}\left[\left(\frac{d_{12}'}{r}\right)^{12} - \left(\frac{d_{12}'}{r}\right)^{6}\right] \tag{5.19}$$

where ϵ_{12} is the depth of the potential well and d_{12}' is the molecular diameter now defined as the distance for which $\phi(r) = 0$. Tabulated values of Ω_D as a function of temperature for a Lennard-Jones potential, useful for the evaluation of D_{12}, exist in the form of $\Omega_D^*(T)$, the reduced collision integral. This is defined as the

ratio of Ω_D to its corresponding hard-sphere value $\sqrt{\frac{kT}{2\pi\mu}}\,\pi d'^{2}_{12}$. Eq. (5.8) can now be rewritten as,

$$D_{12} = \frac{3}{16}\sqrt{\frac{2\pi kT}{\mu}}\;\frac{1}{n\pi d'^{2}_{12}\Omega_D^{*}(T)}$$

$$= 2.628 \times 10^{-3}\;\frac{\sqrt{T^3(M_1+M_2)/2M_1M_2}}{pd'^{2}_{12}\Omega_D^{*}(T)} \qquad (5.20)$$

To show the temperature dependence of Ω_D for the Lennard-Jones Potential, Fig. 8.4-5 of Hirschfeld[26] is reproduced as Fig. V-1. Here, $\Omega_D^{*}(T)$ is plotted against the dimensionless reduced temperature $T^{*} = kT/\epsilon_{12}$. The Lennard-Jones parameters for the Na-He and Na-Ar systems were taken from McCartan and Farr.[28] They are $\epsilon_{Na\text{-}He}/k = 0.72$ K and $d'_{Na\text{-}He} = 7.71$ Å, whereas $\epsilon_{Na\text{-}Ar}/k = 26$ K and $d'_{Na\text{-}Ar} = 5.3$ Å. These parameters were experimentally deduced from measurements by McCartan and Farr of the broadening and shifts of the sodium D lines by helium and argon. The reduced temperatures are $T^{*}_{Na\text{-}He} = 379$ and $T^{*}_{Na\text{-}Ar} = 10.5$ respectively at 275 K. From Fig. V-1, we get $\Omega_D^{*}(T^{*}_{Na\text{-}He}) = 0.44$ and $\Omega_D^{*}(T^{*}_{Na\text{-}Ar}) = 0.74$. Using Eq. (5.20), $D_{Na\text{-}He} = 0.17$ cm^2/sec and $D_{Na\text{-}Ar} = 0.11$ cm^2/sec are obtained at S.T.P. These correspond to $D_{Na\text{-}He}\,P = 137$ Torr-cm^2/sec and $D_{Na\text{-}Ar}\,P = 83.6$ Torr-cm^2/sec.

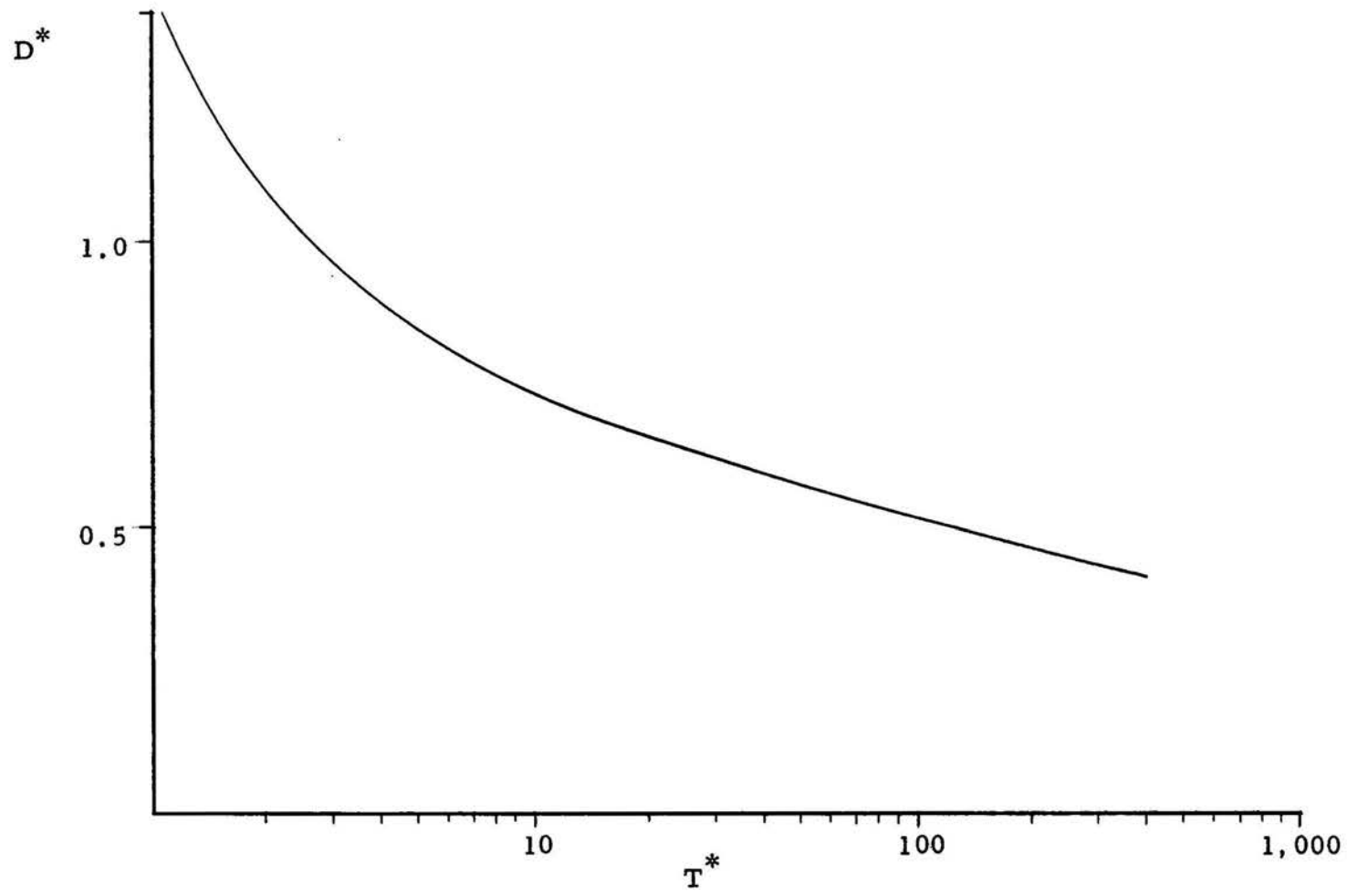

Fig. V-1. Reduced collision integral for diffusion Ω_D^* as a function of reduced temperature $T^* = kT/\epsilon_{12}$.

5.2 Experimental Results

The diffusion coefficients for the Na-He and Na-Ar systems were deduced from measurements of the diffusion time by the resonance fluorescence correlation technique described in Sec. 2.3. The experimental procedure used was discussed in Sec. 3.6. We comment here that, with this technique, we directly measure the decay of the spontaneous fluctuations in the number of sodium atoms in the observation volume. These fluctuations are due to the random thermal motion that is responsible for the diffusive motion of the atoms, while the sodium atom and buffer gas system remains essentially in equilibrium. We did use a slight pressure gradient to drive the sodium atoms into the observation volume. It will be shown that the effect of the flow was negligible under our experimental conditions.

In Fig. V-2, we show a typical time-averaged correlation function obtained for sodium atoms in 200 Torr of helium with $\Delta p \simeq$ 1 Torr, while the laser was tuned on resonance. The laser beam used had an elliptical Gaussian profile with $w_x = 109\ \mu m$ and $w_y = 91\ \mu m$, respectively. The sodium concentration maintained during this run corresponded to about 5 atoms on the average in the observation volume. The fit of the experimental points to Eq. (2.47), represented by the solid curve in Fig. V-2, with the ratio of the two diffusion times $\tau_{Dx}/\tau_{Dy} = w_x^2/w_y^2$ set at 1.47 is excellent. From

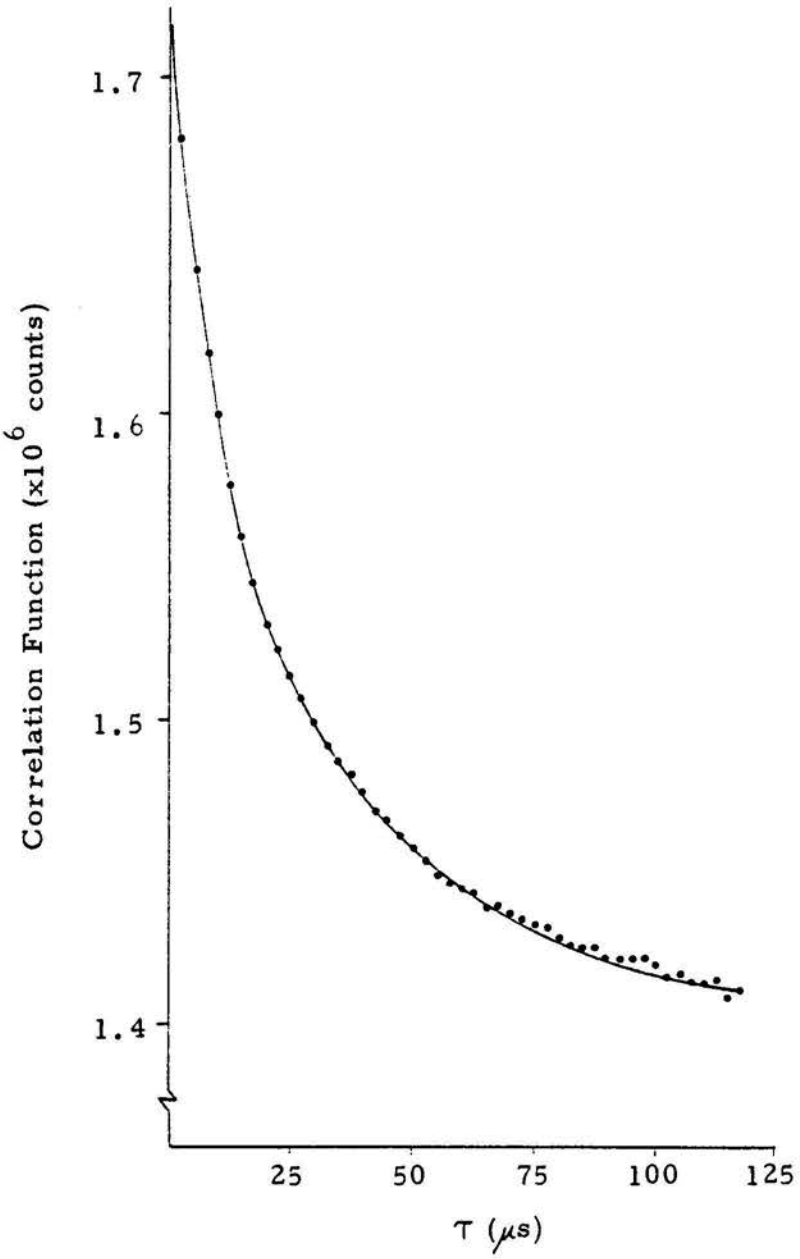

Fig. V-2. Typical time-averaged correlation function for diffusing sodium atoms in 200 Torr of helium with $\Delta p = 1$ Torr. The radii of the laser beams used were $w_x = 109\,\mu m$ and $w_y = 91\,\mu m$.

the fit, we deduced $\tau_{Dx} = w_x^2/4D = 20\ \mu s$ and $\tau_{Dy} = 13.6\ \mu s$. Hence, DP = 297 Torr-cm^2/sec at the experimental temperature estimated to be 50° C. Independent flow velocity measurements using dust particles as described in Sec. 4.1 gave $v \simeq 1$ cm/sec under the experimental conditions of this run. The corresponding time-of-flight of the sodium atom across this laser beam due to flow alone is $\tau_f = 2w/v = 20$ msec. Clearly, since $\tau_D \ll \tau_f$, the effect of flow can be ignored. We have measured the diffusion time, τ_D, at helium pressures ranging from 50 Torr to 400 Torr. Both molecular models discussed in the last section predict that the diffusion coefficient is inversely proportional to gas pressure. Or, equivalently, the corresponding diffusion time, would be directly proportional to gas pressure. In Fig. V-3, we plotted $\tau_{Dx} = w_x^2/4D$ for $w_x = 109\ \mu m$ as a function of He pressure. Each point represents one experimental run. There is a definite departure from straight line that the theory predicts. Unfortunately, the temperature in the observation volume was not monitored directly during the run. In fact, we found out later that it was significantly different for different runs, because in order to maintain desired sodium level, the sodium pocket needed to be heated to different extent at different pressures. Later, a thermocouple was inserted in the cell center to compare the temperature of the observation volume to the temperature of the sodium pocket while trying to reproduce the conditions of the different

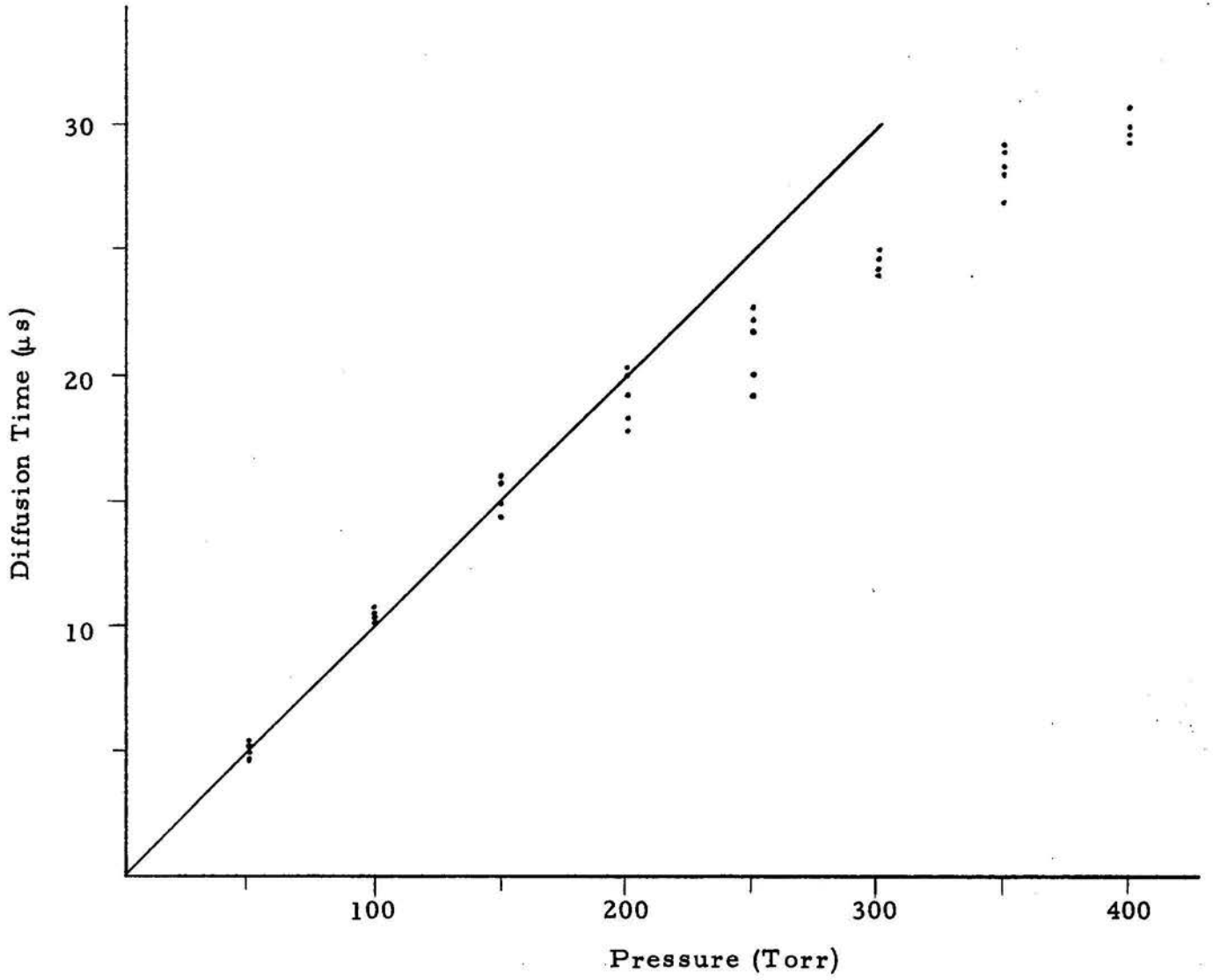

Fig. V-3. The diffusion time $\tau_{Dx} = w_x^2/4D$ $w_x = 109$ μm versus the pressure of helium buffer gas.

diffusion measurement runs. Using the predicted $T^{3/2}$ dependence, the diffusion time data shown in Fig. V-3 were normalized to 273 K and replotted in Fig. V-4. Two other sets of experiments were performed with laser beam dimension (w_y = 59 μm, w_x = 45 μm) and (w_y = 144 μm, w_x = 125 μm) respectively. As above, the diffusion time corresponding to the longer beam dimension was determined by a computer fit. These data were corrected to 273 K and plotted in Fig. V-5 and Fig. V-6. In general, these curves still bend over at helium pressures above 250 Torr, but to a lesser extent than that shown in Fig. V-3. We also note that the data taken at smaller beam diameters appear to curve over more significantly. The error in τ_D estimated from the spread for several runs taken at the same pressure was about 5%. The deviations at high pressures from the straight line appear to be bigger than that. As a further check on the pressure dependence of the diffusion coefficient, we plotted $D_{Na\text{-}He}p$ (Torr-cm^2/sec at 273 K) as a function of helium pressure in Fig. V-7. Each point represents the average of the runs taken at a particular pressure. The error bars indicate our estimate on the possible systematic errors in diffusion coefficients measurements to be discussed in more detail later. A straight line was drawn through the average of the experimental points. This average corresponds to $D_{Na\text{-}He}p$ = 240 Torr-cm^2/sec or $D_{Na\text{-}He}$ = 0.32 ± cm^2/sec at S.T.P. This compares with the

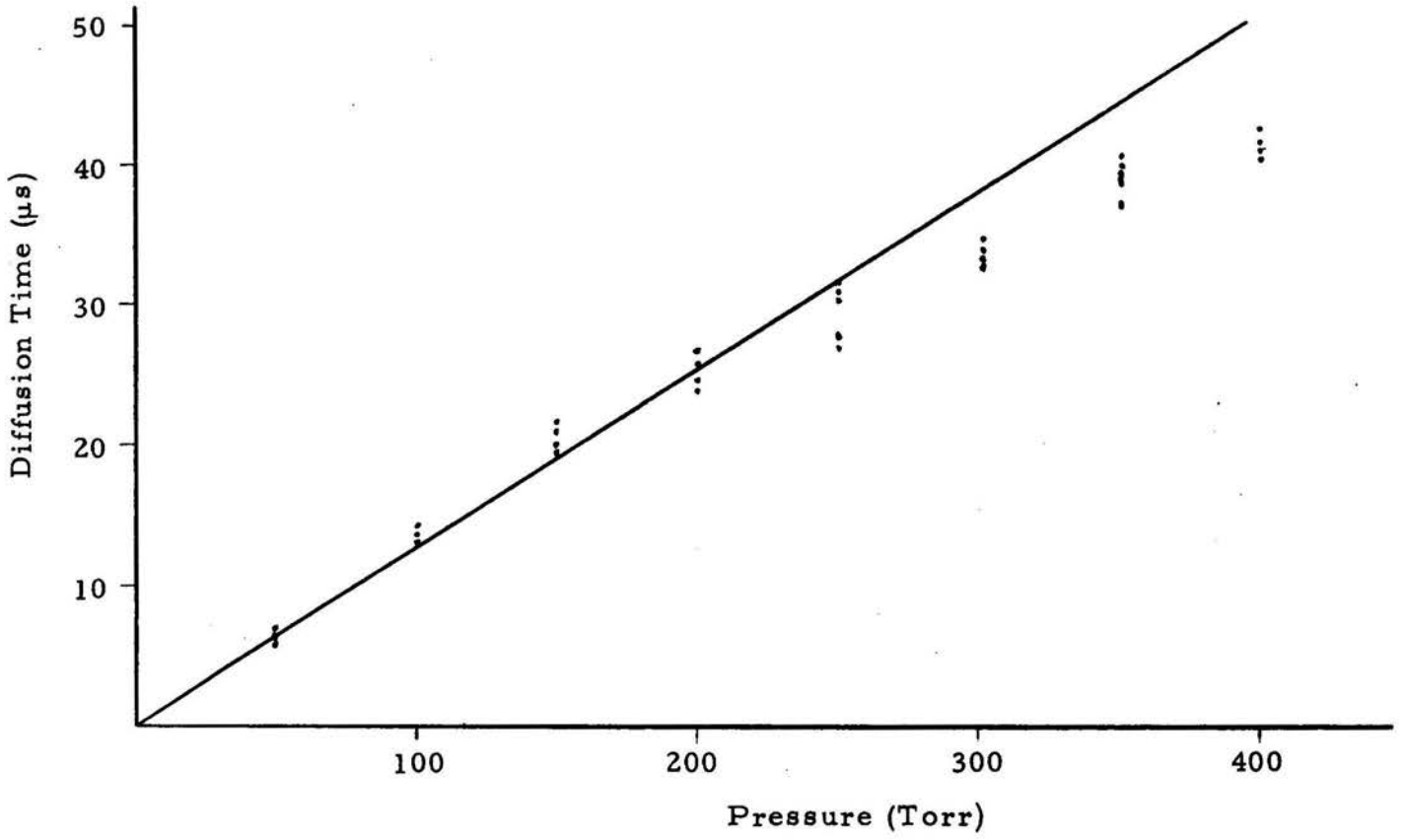

Fig. V-4. The data shown in Fig. V-3 have now been normalized using the $T^{3/2}$ dependence to 273 K and plotted as a function of the pressure of helium buffer gas.

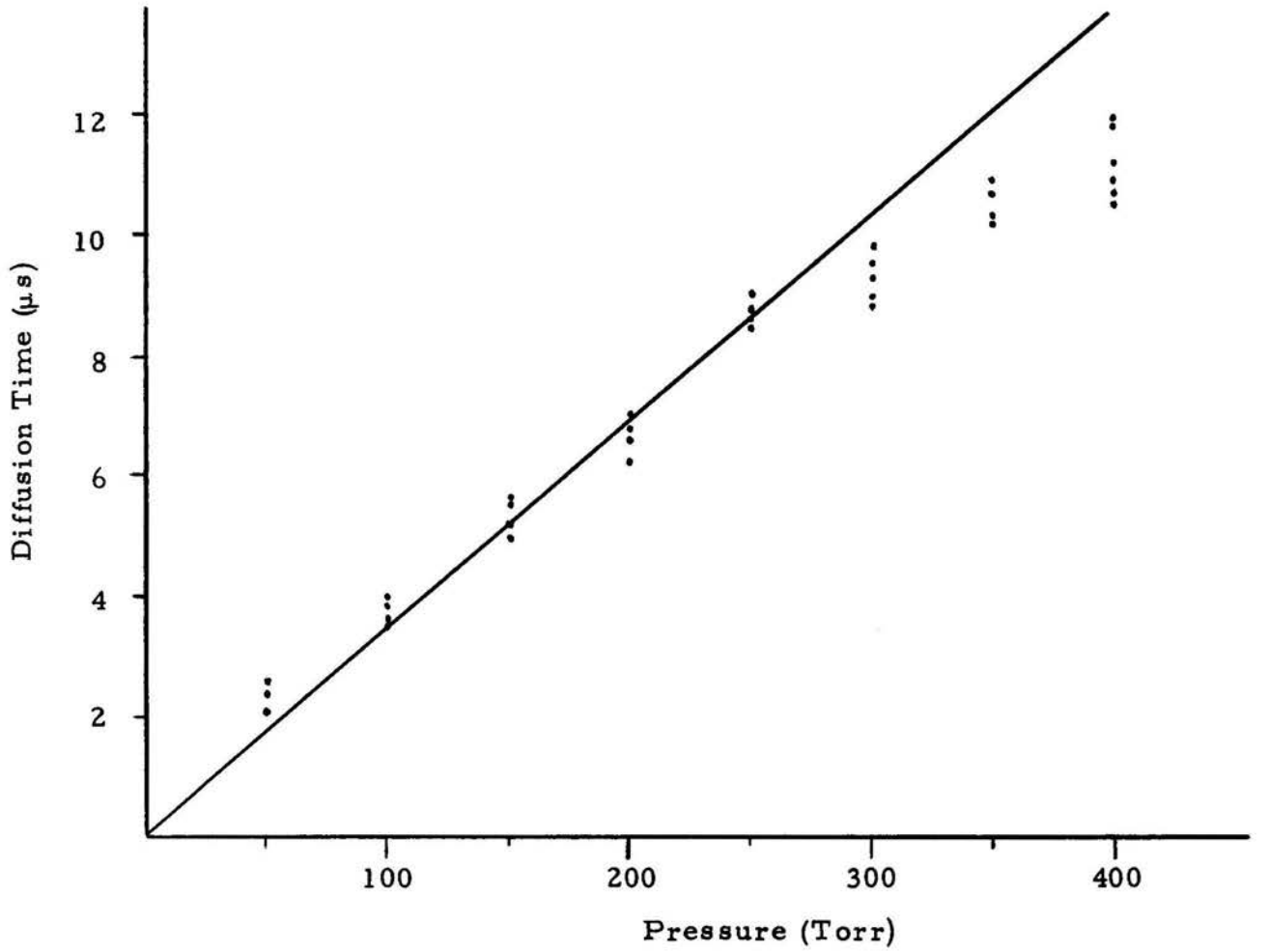

Fig. V-5. The diffusion time $\tau_{Dy} = w_y^2/4D$, $w_y = 59$ μm versus pressure of the helium buffer gas. The data have been normalized to 273 K.

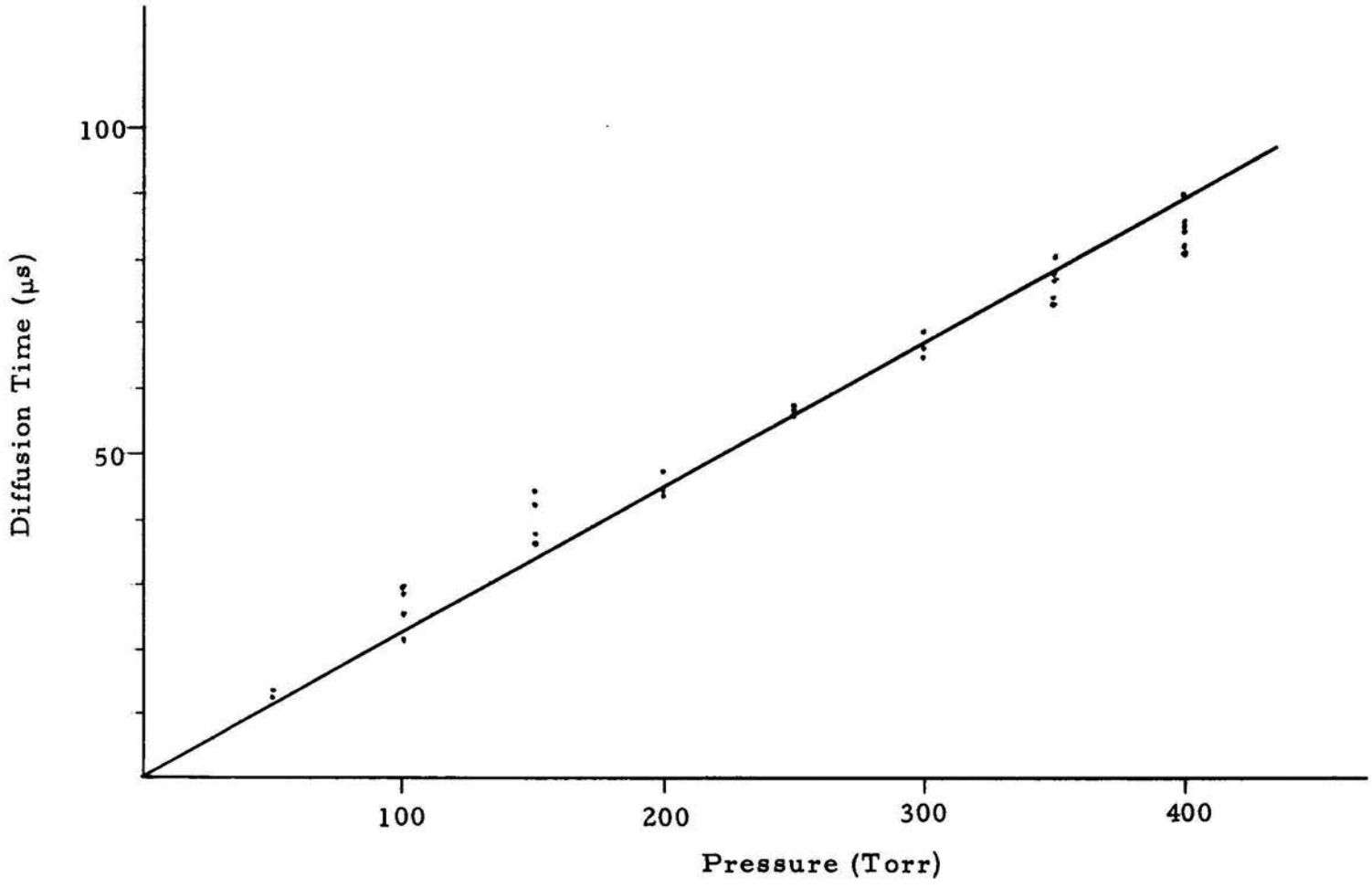

Fig. V-6. The diffusion time $\tau_{Dy} = w_y^2/4D$, $w_y = 144$ μm versus pressure of the helium buffer gas. The data have been normalized to 273 K.

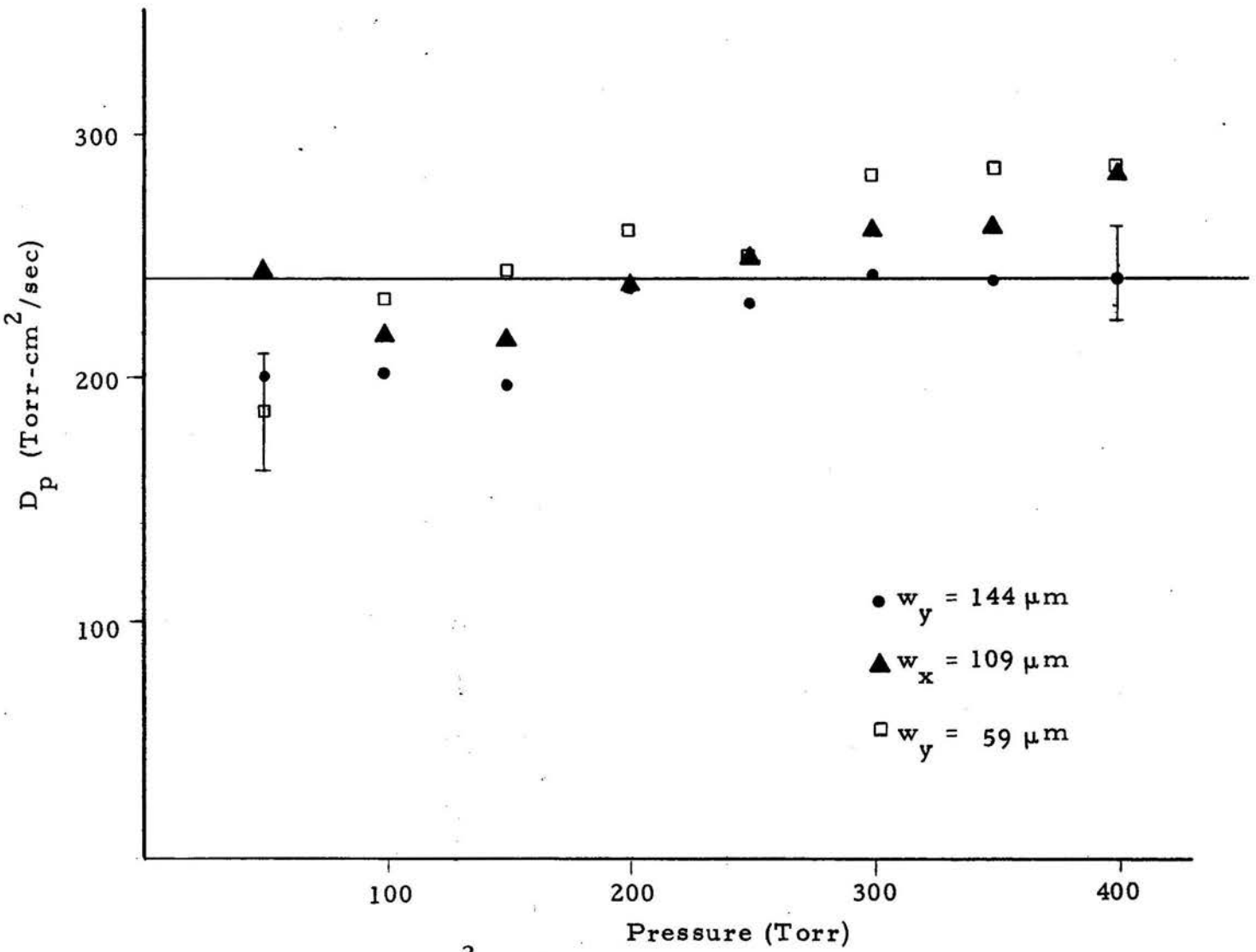

Fig. V-7. $D_{Na\text{-}He}p$ (in Torr-cm^2/sec) at 273 K is plotted as a function of helium buffer gas. The error bars indicate estimate of possible systematic error.

theoretical estimate of 0.5 and 0.17 cm^2/sec for the hard-sphere and Lennard-Jones potential models respectively. There have been few previous experiments determining D_{Na-He} and none on the pressure dependence of D_{Na-He}. Ramsey and Anderson[29,30] obtained $D_{Na-He} = 0.92 \pm 0.45$ cm^2/sec at 155°C and 1 amagat (2.69×10^{19} atoms/cm^3) and 1.0 ± 0.3 cm^2/sec at 154°C and 0.92 amagat. These corresponded to 0.74 cm^2/sec at S.T.P. A. Gozzine et al.[31] obtained 1.5 cm^2/sec at 1 amagat and 170°C, or 1.18 cm^2/sec at S.T.P. These are appreciably higher than the above theoretical estimate and our results.

Preliminary experiments were also performed to measure the diffusion coefficient of Na-Ar system. Fig. V-8 shows τ_{Dy} for Na-Ar system as a function of argon pressure from 10 to 50 Torr, normalized to 273 K. The beam radii were $w_y = 56$ μm and $w_x = 49$ μm respectively. In Fig. V-9 additional diffusion times for the same system and beam radii are shown from runs at higher pressures. Clearly, the curve for τ_D for Na-Ar also bends over at higher pressures. Using the low pressure data of Fig. V-8, we obtained a diffusion coefficient of $D = 0.11 \pm 0.03$ cm^2/sec at S.T.P. Theoretical predictions are 0.17 cm^2/sec and 0.11 cm^2/sec for hard sphere and Lennard-Jones potential models respectively. Ramsey and Anderson[31] using the spin relaxation cross-section of the Na-Ar system measured in ref. 32 estimated that $D_{Na-Ar} = 0.2$ cm^2/sec at

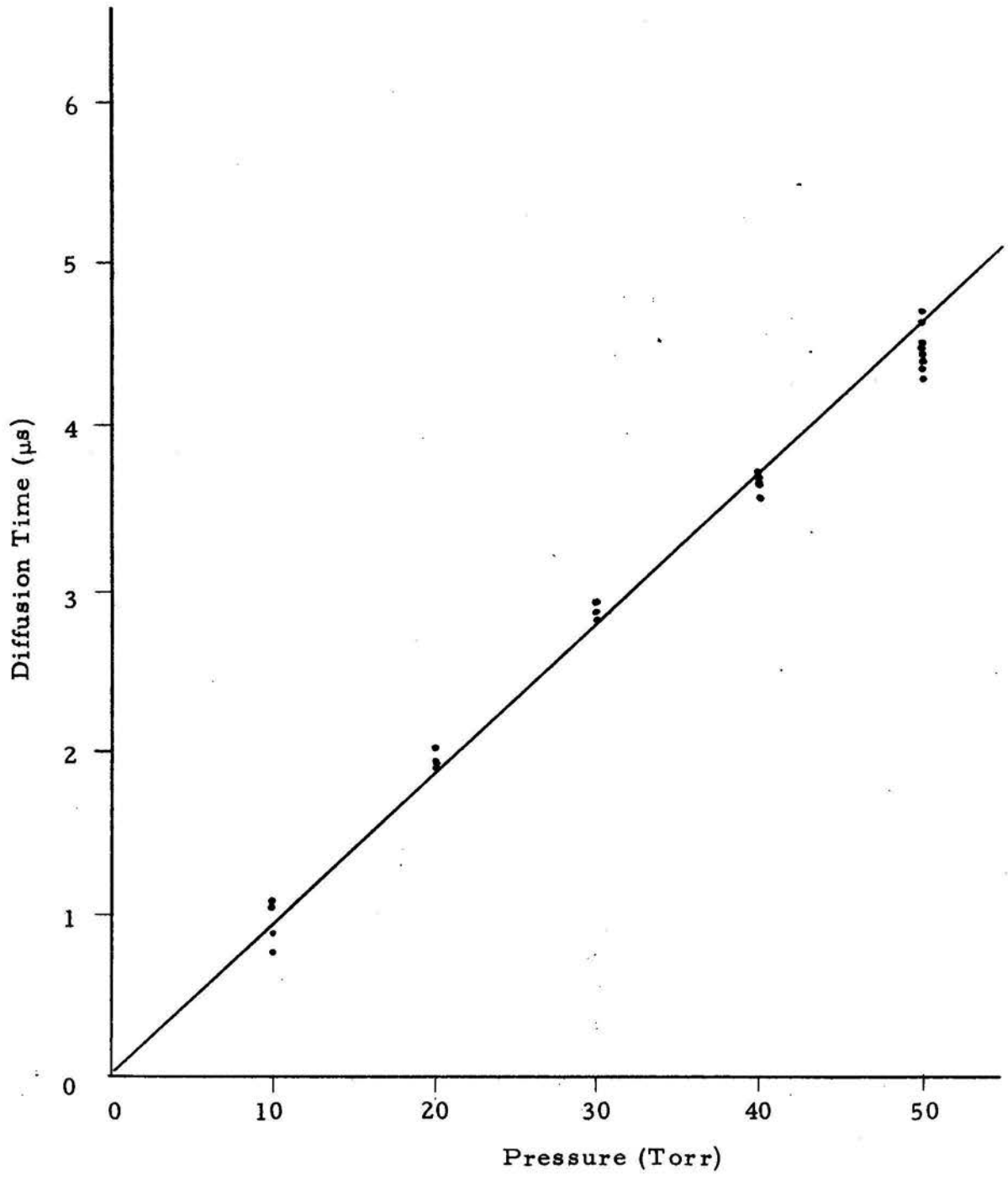

Fig. V-8. The diffusion time $\tau_{D_y} = w_y^2/4D$, $w_y = 56\,\mu m$, at 273 K versus the pressure of the argon buffer gas from 10 Torr to 50 Torr.

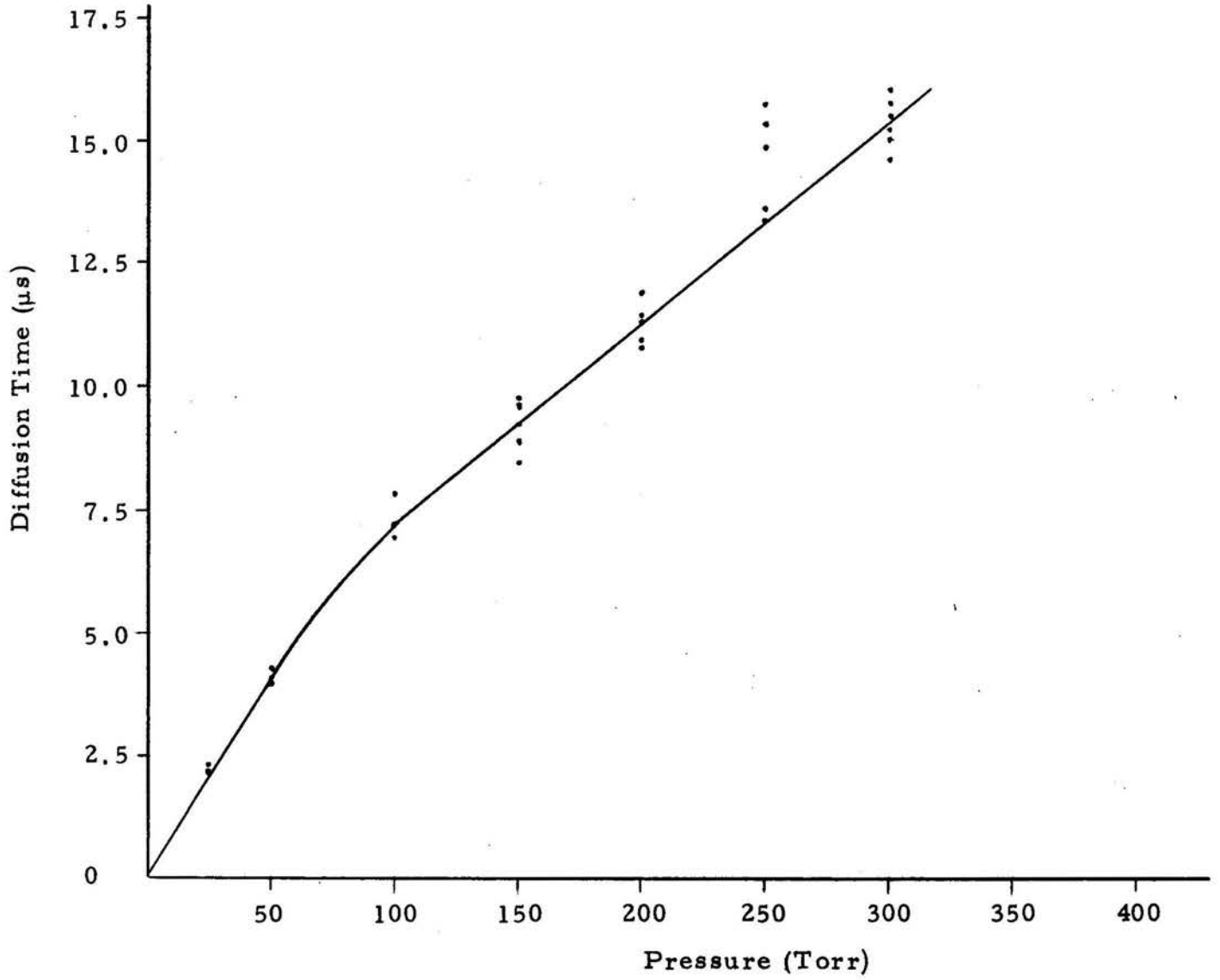

Fig. V-9. The diffusion time $\tau_{Dy} = w_y^2/4D$, $w_y = 56\ \mu m$ at 273 K versus the pressure of the argon buffer gas from 25 Torr to 300 Torr.

1 amagat and 155° C, or $D_{Na-Ar} = 0.16\ cm^2/sec$ at S.T.P. In Table V-1, our experimental results on diffusion coefficients are summarized and compared with theoretical predictions using kinetic theory and previous experiments.

Let us consider the possible systematic errors in our diffusion coefficient measurements. First of all, we are sure the correlation functions we observed were indeed due to the sodium atoms, they are not of spurious contributions such as spontaneous temperature or volume fluctuations, fluctuations in the number of dust particles present and instrument noise. This was checked by doing runs with the laser tuned off resonance. No correlation functions were observed. The effect of flow was negligible, as we have discussed earlier using arguments on the relative magnitudes of diffusion time and time-of-flight of the sodium atoms. Another source of error arises from the use of the single-clipped digital correlator instead of a "true" correlator. If the error introduced by clipping is appreciable, the observed correlation function can no longer be described by Eq. (2.44) or Eq. (2.45). Hence, the success of using these equations to fit the experimental data is an indication of the errors due to clipping and curve fitting. This is estimated to be about 5% judging from the spread of τ_D for different runs taken at the same pressure. The presence of trace amount of impurities in the buffer gas, which might chemically react with sodium atoms is not a big

Table V-1. D_{Na-He} and D_{Na-Ar} obtained in this work compared with theoretical predictions and previous experiments.

	This work	Theory		Previous experiments
		Hard Sphere Model	Lennard-Jones Model	
D_{Na-He} (cm^2/sec)	$0.32 \pm .08$	0.50	0.17	0.74 ± 0.38
D_{Na-Ar} (cm^2/sec)	$0.11 \pm .03$	0.17	0.11	0.16 ± 0.08

concern. The sodium atom spent on the average less than 50 μs in the laser beam at the highest buffer gas pressure used. Grossman et al.[33] showed the reaction rate of cesium atoms with oxygen impurities in the Cs-Ar system, an analagous system, is approximately 10 sec^{-1}. This is much too slow to show any effect in the technique we employed. Therefore, there should not be any significant systematic error in our measured diffusion times extracted from them.

The values of D_{Na-He} and D_{Na-Ar} reported above were determined from experimental measurements of the diffusion times, laser beam radii, and temperature and pressure of the Na-He and Na-Ar systems at the time of the measurement. Because of the finite size of the pinhole used (30 μm) for laser beam dimension measurement, the uncertainty in w for smaller beam radii used is about 7.5% and smaller for larger beams. This is estimated as follows. Our measurement of laser beam radius w involves the determination of the power meter position where the measured laser power $P(x, y)$ drops to $1/e^2$ of its peak value. Let us consider the case where the power meter is translated in the x-direction with $y = 0$. The error in w arises from both laser power fluctuations and error in determining $(x = x_o)$ where $P(x_o, 0)/P(0, 0) = e^{-2}$, $P(0, 0)$ being the laser power measured at beam center. For simplicity in calculation, we assume that we have a square aperture of area πx_p^2, where x_p is the radius of the pinhole used. The

integrated power measured by the power meter through the aperture at position $(x_0, 0)$ is given by

$$P(x_o, 0) = I_o \int_{x_o - \sqrt{\frac{\pi}{2}} x_p}^{x_o + \sqrt{\frac{\pi}{2}} x_p} \int_{-\sqrt{\frac{\pi}{2}} x_p}^{\sqrt{\frac{\pi}{2}} x_p} e^{-2(x^2+y^2)/w^2} dxdy \quad (5.21)$$

Let $x' = \sqrt{2}x/w$, $y' = \sqrt{2}y/w$ Eq. (5.21) becomes

$$P(x_o, 0) = \frac{w^2}{2} I_o \int_{\sqrt{2}/w\,(x_o - \sqrt{\frac{\pi}{2}} x_p)}^{\sqrt{2}/w\,(x_o + \sqrt{\frac{\pi}{2}} x_p)} e^{-x'^2} dx' \int_{-\sqrt{\frac{\pi}{2}} \frac{x_p}{w}}^{\sqrt{\frac{\pi}{2}} \frac{x_p}{w}} e^{-y'^2} dy'$$

$$= 1/4\, \pi w^2 I_o \operatorname{erf}\left(\sqrt{\frac{\pi}{2}} \frac{x_p}{w}\right) \left\{ \operatorname{erf}\left[\frac{\sqrt{2}}{w} (x_o + \sqrt{\frac{\pi}{2}} x_p)\right] - \operatorname{erf}\left[\frac{\sqrt{2}}{w} (x_o - \sqrt{\frac{\pi}{2}} x_p)\right] \right\} \quad (5.22)$$

and

$$P(0, 0) = \tfrac{1}{2} \pi w^2 I_o \left[\operatorname{erf}\left(\sqrt{\frac{\pi}{2}} \frac{x_p}{w}\right)\right]^2 \quad (5.23)$$

x_o is determined by

$$\frac{P(x_o, 0)}{P(0, 0)} = \frac{\operatorname{erf}\left[\frac{\sqrt{2}}{w}\left(x_o + \sqrt{\frac{\pi}{2}}\, x_p\right)\right] - \operatorname{erf}\left[\frac{\sqrt{2}}{w}\left(x_o - \frac{\sqrt{\pi}}{2}\, x_p\right)\right]}{2\, \operatorname{erf}\left[\sqrt{\frac{\pi}{2}}\, \frac{x_p}{w}\right]}$$

$$= e^{-2} \tag{5.24}$$

For $w = 50\ \mu m$ and $x_p = 30\ \mu m$, Eq. (5.24) gives $x_o = 52.5\ \mu m$. This is an error of 5%. Assuming the laser power fluctuates by ΔP, the apparent radius r_p is determined by using

$$e^{-2}\left(1 + \frac{\Delta P}{P}\right) = e^{-2r_p^2/w^2} \tag{5.25}$$

Typically, the fluctuation in the output power of the dye laser is less than 10%. For $\Delta P/P_o = 0.1$, $w = 50\ \mu m$, Eq. (5.25) gives $r_p = 48.8\ \mu m$, i.e. 2.5% error. Hence, the overall error in the determination of w is about 7.5%. The uncertainty in the pressure of the gases was at most $\pm$ 2 Torr, and is therefore negligible. More importantly, the temperature of the gases in the observation volume should be measured during the experiment in order to eliminate the possible errors in the temperature corrections to the data. Errors we made by measuring the temperature at a later time are hard to estimate, but they could account for the apparent, incorrect dependence of the measured diffusion time. Taking into account all these errors, we roughly estimate the precision of diffusion coefficient measurements to be about 25%.

Fairly recently, with a revised apparatus, we were able to study the diffusion coefficients of Na-He system while simultaneously monitoring the temperature. This was realized by using a retractable thermocouple in the flow cell which remained out of the way while a correlation function was being accumulated. It was inserted into the observation volume right after an experimental run. Another modification was heating only a small amount of Na by resistance wire wrapped around it rather than heating the whole inlet tube. There was less heating of the gas and hence less possible temperature error. Data obtained in the latest run is shown in Fig. V-10. The laser beam radii used were $w_x = 63\ \mu m$ and $w_y = 100\ \mu m$. As before, the diffusion times were normalized to 273 K. The signal-to-noise of some of the correlation functions observed was not very good because the sodium level was too low initially and was not accumulated for a long time. This resulted in the large spread in τ_D at lower pressures. Within experimental error, however, we did get a straight line. From the slope of the curve, we obtained $D_{Na\text{-}He}p = 270$ Torr-cm^2/sec, or $D_{Na\text{-}He} = 0.36$ cm^2/sec at S.T.P. With additional experiments, we should be able to resolve questions about the pressure dependence of these diffusion coefficients in the near future.

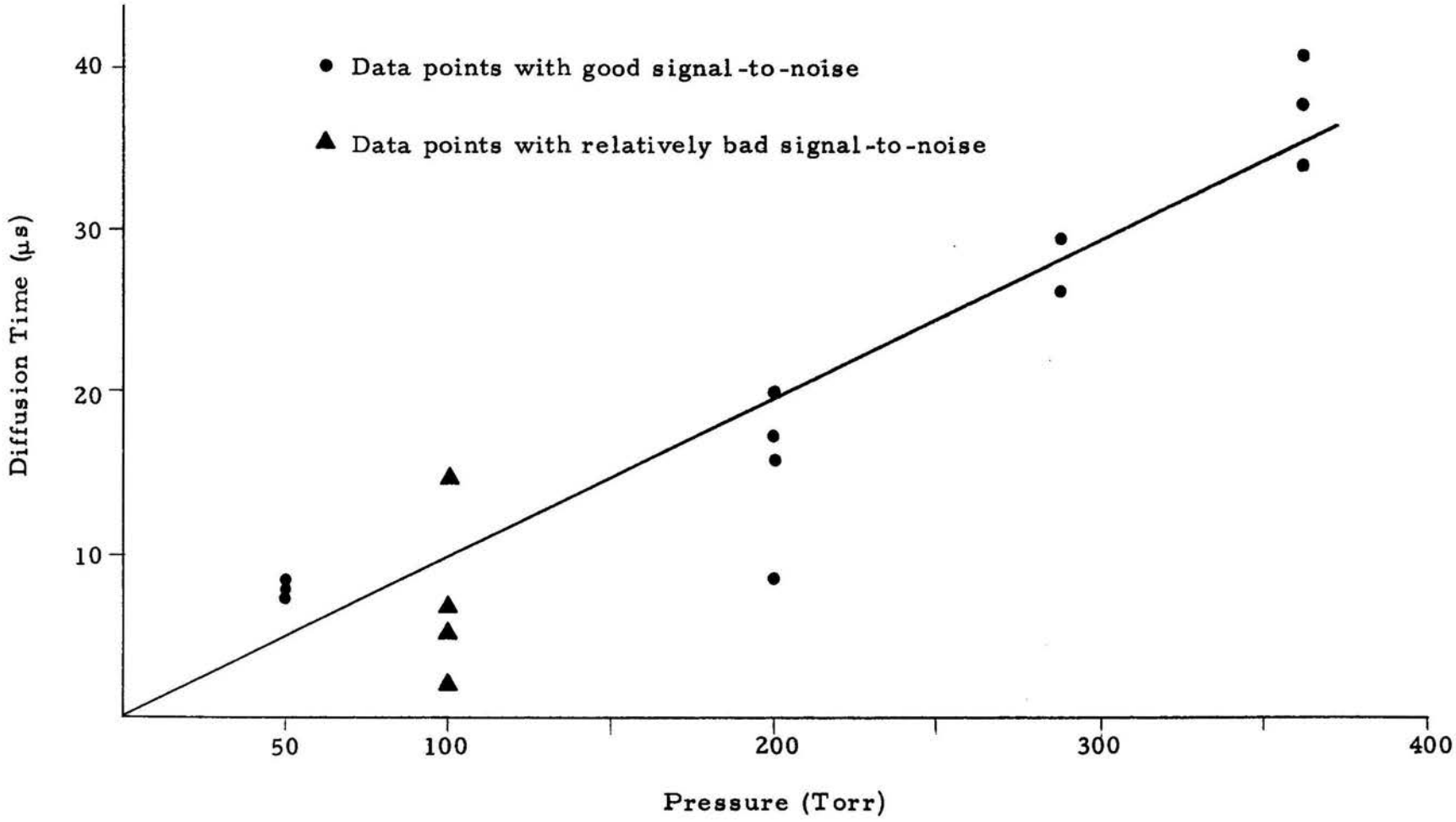

Fig. V-10. The diffusion time $\tau_{Dy} = w_y^2 / 4D$, $w_y = 100\ \mu m$ at 273 K versus the pressure of the helium buffer gas. The runs with good and bad signal-to-noise are as indicated in the figure.

VI. CONCLUSIONS AND SUGGESTIONS FOR FUTURE WORK

In this thesis, the resonance fluorescence correlation technique for single-atom velocity measurements is presented. With this technique, we have successfully detected individual sodium atoms in helium buffer gas. This is the first time that single atoms have been detected by the resonance fluorescence method in a buffer gas. We have also measured for the first time the transit-time of an atom diffusing across a laser beam. Among other things, we showed that a study of the probability distribution of resonantly scattered photons allowed the estimation of the average fluorescence photon burst size due to the individual sodium atoms traversing the laser beam. A comparison to theory was made and good agreement was found.

By averaging the diffusion times over many sodium atoms, we found that this technique also provides a convenient method for measuring the diffusion coefficients of sodium atoms in a helium or argon buffer gas. The diffusion coefficients obtained in this manner were found to be in reasonable agreement with theoretical predictions based on kinetic theory. Within experimental error, they also agree with experimental data obtained by other workers using different techniques. We believe our technique for diffusion

coefficient measurements is the most convenient and most accurate one to date. In addition, it can be applied to many other atoms as long as the appropriate laser for the resonant transition is available. In molecular gases, however, the presence of vibrational-rotational level might cause the quenching of fluorescence emission. The formulae derived in Chapter II would have to be modified for these cases.

We have also shown that the measurement of the velocity of individual sodium atoms in a flow with much higher flow velocity is within our reach. The demonstrated agreement with theory gives us confidence in predictions for future experiments at other flow conditions. For example, consider a sodium atom in a helium flow at 200 Torr and 40°C with flow velocity of $v = 2500$ cm/sec. If two laser beams of radii $w = 500\ \mu m$ and separated by 1.2 mm are used, the diffusion time is $\tau_D = 400\ \mu s$, while the time-of-flight across the two laser beams is $\tau_f = 48\ \mu s$. Under these conditions, flow would dominate diffusion, and an average flow velocity could be measured. With I_o/I_s set at 1.91, the optimum value, we need 40 mw of laser power per beam in the flow cell. Then 18 counts can be expected for a sodium atom traversing the center of both laser beams, assuming a detection efficiency of 1.0%. For our present flow cell, the background level would be of the order of 2×10^6 counts/sec. If one chooses the sample time to be $4\ \mu s$,

there would be 8 counts per sample time due to background, while the correlator in its present form can clip at most 9 counts. Unfortunately, this background level exceeds the maximum current rating of the RCA 31034A photomultiplier used in our experiments. A reduction of background would therefore be necessary if this tube is to be used. Alternately, we can use a good photon counting photomultiplier with high quantum efficiency, which can also handle the high count rate without saturation. A good candidate which is also reasonably priced is the RCA 8852 photomultiplier. Unfortunately, the quantum efficiency of this tube is only $\eta = 12\%$ at 5890Å. This efficiency is only about half as high as the RCA 31034A tube presently in use. A factor of two increases in optical collection efficiency ϵ would be desirable to compensate for this loss in quantum efficiency. For flow velocity of the order of sound velocity or higher, this increase in ϵ would be mandatory because the number of fluorescence photons emitted by an atom is inversely proportional to its velocity. An ellipsoidal collector such as the one used by Greenless et al.[2] should do the job. In principle, as much as 80% of the emitted photons can be collected. With the RCA 8852 photomultiplier, the total detection efficiency would then be 9.6%, almost a factor of 10 higher than our present efficiency. Unfortunately, this also means higher background counts as more stray light photons will be collected. The further reduction of background would be

difficult but not impossible. More and better diaphragms are needed. Another scheme which might help involves using a slit at the second focus of the ellipsoidal collector right before the photomultiplier. In this manner, one could prevent a good portion of the spurious light originating from regions outside the observation volume from reaching the photocathode.

It is also of interest to measure the velocities of the individual sodium atoms in vacuum, where thermal velocities are on the order of 5×10^4 cm/sec. At a laser power level of 50 mw, 90 counts per transit can be expected for a sodium atom going through the center of a laser beam with $w = 1.02$ cm, if a detection efficiency of 9.6% is assumed. Again, care must be taken to reduce stray light to a reasonable level. Of course, in this case, there is no Rayleigh scattering due to the buffer gas, which helps considerably. Iodine cell does not help in this case, because the Doppler-broadened sodium D_2 line is of about the same width as the I_2 absorption line. As a result, stray light and sodium resonance fluorescence are both blocked.

Once single-atom velocity measurements are achieved, practical applications such as high speed flow diagnosis, measuring the velocity distribution of atoms evaporated or sputtered from a surface and testing the fundamental results in kinetic theory could be

done. The accomplishments reported in this thesis represent an important first step in these endeavors.

REFERENCES

1. G. S. Hurst, M. H. Nayfeh, and J. P. Young, Appl. Phys. Lett. 30, 229 (1977).

2. G. W. Greenless, D. L. Clark, S. L. Kaufman, D. A. Lewis, J. F. Toun, and J. H. Broadhurst, Opt. Comm. 23, 236 (1977).

3. V. I. Balykin, V. S. Letokhov, V. I. Mishin, and V. A. Semchisen, JETP Lett. 26, 492 (1977).

4. G. I. Bekov, V. S. Letokhov, O. I. Matveen, and V. I. Mishin, Opt. Lett. 3, 159 (1978).

5. W. M. Fairbank, Jr., T. W. Hansch, and A. L. Schawlow, J. Opt. Soc. Am. 65, 199 (1975).

6. G. S. Hurst, M. G. Payne, M. H. Nayfeh, J. P. Judish, and E. B. Wagner, Phys. Rev. Lett. 35, 82 (1975).

7. See for example, A. Yariv, Quantum Electronics, 2nd Edition, New York, John Wiley and Sons, 1975.

8. N. Ioti, F. Strumia, and A. Moretti, J. Opt. Soc. Am. 61, 1251 (1971).

9. A. C. G. Mitchell and M. W. Zemansky, "Resonance Radiation and Excited Atoms," Cambridge University Press, 1971.

10. C. J. Oliver, "Correlation Techniques," in "Photon Correlation and Light Beating Spectroscopy," H. Z. Cummins and Z. R. Pike, ed., Plenum Press, New York and London, 1974, p. 151.

11. V. Degiorgio, "Photon Correlation Techniques," in "Photon Correlation Spectroscopy and Velocimetry," H. Z. Cummins and E. R. Pike, ed., Plenum Press, New York and London, 1977, p. 142 and reference therein.

12. K. G. Bartlett and C. Y. She, Opt. Lett. 1, 175 (1977).

13. C. Y. She, Optica Acta, to be published (1979).

14. D. Magde, E. Elson, and W. W. Webb, Phys. Rev. Lett. 29, 705 (1972).

15. E. Elson and D. Magde, Biopolymers 13, 1, 29 (1975).

16. P. N. Pusey, "Statistical Properties of Scattered Radiation," in "Photon Correlation Spectroscopy and Velocimetry," H. Z. Cummins and Z. R. Pike, ed., Plenum Press, New York and London, 1977, p. 45.

17. F. W. Kowalski, R. T. Hawkins, and A. L. Schawlow, J. Opt. Soc. Am. 66 (9), 965 (1976).

18. R. R. Rudder and D. R. Buch, J. Opt. Soc. Am. 58 (9), 1260 (1968).

19. S. K. Poultney, "Single Photon Detection and Timing: Experiments and Techniques," in Advances in Electronics and Electron Physics, edited by L. Marton, vol. 31, New York, Academic Press (1972).

20. G. E. Devlin, J. L. Davis, L. Chase and S. Geschwind, Appl. Phys. Lett. 19 (5), 138 (1971).

21. G. A. Kokovin, Izu. Sib. Otd. Akad. Nank, SSSR Ser. Khim. Nauk. 1, 13 (1970).

22. K. G. Bartlett, Ph.D. Thesis, Colorado State University, 1977.

23. L. D. Landau and E. M. Lifschitz, Fluid Mechanics, Pergamon Press, 1959.

24. R. D. Present, "Kinetic Theory of Gases," New York, McGraw-Hill, 1958.

25. J. O. Mirschfelder, C. F. Curtiss, and R. B. Bird, "Molecular theory of gases and liquids," New York, John Wiley and Sons, 1954.

26. S. Chapman and T. G. Cowling, "The mathematical theory of non-uniform gases," Cambridge, Cambridge University Press, 1970.

27. D. I, Lee and C. F. Bonilia, Nucl. Eng. Design 7, 455 (1968).

28. D. G. McCartan and J. M. Farr, J. Phys. B.: Atom & Mol. Phys. 9 (6), 985 (1976).

29. L. W. Anderson and A. T. Ramsey, Phys. Rev. 132, 712 (1963).

30. A. T. Ramsey and L. W. Anderson, Nuovo Cimento 32 (15), 115 (1964).

31. A. Gozzine, N. Ioli and F. Strumia, ibid. 49B, 185 (1967).

32. H. G. Dehmelt, Phys. Rev. 105, 1487 (1957).

33. L. W. Grossman, G. S. Hurst, S. D. Kramer, M. G. Payne, and J. P. Young, Chem. Phys. Lett. 50 (2), 207 (1977).